



**University of  
Nottingham**

UK | CHINA | MALAYSIA

# New Characterisation Techniques for Thin Film Antiferromagnetic Materials

**Stuart Forbes Poole**

Thesis submitted to the University of Nottingham  
for the degree of Doctor of Philosophy

**October 2023**

*“Smart enough to do a PhD;  
stupid enough to do a PhD.”*

# ***Abstract***

Antiferromagnets (AFMs), with their rise in prominence and the discovery of new effects, have led to growing interest in antiferromagnetic spintronics and their possible applications. Since AFMs have little or no stray fields and very low magnetic susceptibility, one of the biggest challenges faced by the field of AFM spintronics is the difficulty to manipulate and measure the magnetic structure of these systems. Most techniques capable of unambiguous detection of magnetic changes or domain structure require large facilities, and so the aim of the contained thesis was to support the development of new benchtop techniques capable of making such observations in AFMs.

Spin flop is a reliable and well understood method to create a repeatable reorientation of moments in an AFM. The extents to which spin flop reorients the moments in a uniaxial thin film sample of CuMnAs was determined using neutron diffraction and was found to be up to be up to 98 % at 8 T. This study also demonstrated the capability to detect AFM ordering in films as thin as 20 nm using neutron diffraction. Accompanying transport measurements, using anisotropic magnetoresistance (AMR) as the readout mechanism, were performed and show good agreement between the techniques in both the shape of the signals and the strength of the spin flop threshold field.

Asynchronous optical sampling was used to develop a rapid technique capable of characterising CuMnAs films grown on GaAs(001) and GaP(001) substrates in a matter of hours, without the need for high magnetic fields, cryogens or facilities. This utilised the changes in the Voigt effect to measure the difference in polarisation of light during and after a heating pump pulse partially demagnetises a CuMnAs film. The same polarisation changes were used to successfully detect the reorientation of moments undergoing spin flop using delay line pump probe.

While working on these optical setups, some of the elastic constants of CuMnAs were measured for use in simulation of domain formation as values to use in magnetostriction and shape anisotropy terms. The measured constants are  $c_{33} = 146 \pm 12$  GPa,  $c_{11} = 37 \pm 1$  GPa and  $c_{44} = 73 \pm 7$  GPa, where the final constant determinable in these studies was found to have two different possible values of  $c_{13} = -40 \pm 6$  GPa or  $c'_{13} = -104 \pm 7$  GPa.

A room temperature vacuum system was developed that was demonstrated to be capable of keeping a sample between  $-8$  and  $+60$  °C, with a stability below 5 mK at all temperatures in that range, where the ambient temperature was  $\approx 22$  °C. The vacuum chamber can be evacuated down to  $10^{-8}$  hPa using a readily available turbo pump.

The room temperature system was used to develop a high power probing technique for transport measurements in which the applied measurement currents are up to twenty times higher than accessible using DC probing. In the attempts to measure the deflection as a result of Néel order spin orbit torques, the combination of high currents and high fields led to the discovery of a new, large AMR signal which generates a large difference in measured AMR between antiparallel pulses in CuMnAs devices which would normally be symmetric under this change in sign of the current. This large signal is promising, but attempts to determine its origin were inconclusive.

Overall several developments were made toward the aim of accessible benchtop techniques for measuring the magnetic structure of AFM materials.

## ***Acknowledgements***

I would like to thank many people for helping with the works contained, writing and proofreading the thesis and for keeping me afloat throughout. First though, big ups to methylphenidate hydrochloride and ADHD diagnosis, without these, writing a thesis would never have been possible.

Thank you to the artists making the music that sustained me throughout my PhD and especially during the writing of this thesis.

Thank you to my colleagues and peers for allowing me to annoy you whenever I was bored and for helping make my time at UoN as delightful as it was. A special thanks to OJA and CM for helping with all my theoretical problems and for being a first port of call when I was struggling.

Thank you to my parents for hosting me during the writing process thus minimising all stresses unrelated to writing thee thesis.

Thank you to the friends I made in Nottingham. A special thanks to AW, SA and ST for being particularly understanding and for providing a safe place to rest. Thank you again to SA and ST for letting me use your houses as a home away from home. Without your welcoming generosity, I would have struggled to visit as often as I have.

Thank you to the Volume 1 café and climbing gym, as well as the staff. Without the café to work in, and the possibility to climb after, I would never have maintained motivation as long as I did. Without all the friendly faces, I would never have felt welcome enough to use this space as effectively as I did.

Thank you to all those friends I made at Volume 1. Your openness and kindness made my living at my parents, away from all my friends in Nottingham, worth it all. A special thanks to AS-C, LS-C, OC and LL for being the best friends I've ever had in that town.

Thank you to AEG for being so close to me for all these years. Without your support I would never have made it through the start of my PhD, let alone

made it this far.

Thank you to my collaborators at TU Dortmund, Germany, especially EE for being a gracious host and very helpful lab partner. You made the stays and work more comfortable than I could have ever expected.

Thank you to TK for allowing me free rein of your optics labs and for your help taming the lasers.

Thank you to the engineering workshop staff for giving me unreasonably free rein of the workshop resources, whether for work or not, you gave access to many resources I am grateful for.

Finally, I want to thank my supervisors for their patience, motivation and dedication throughout. Thank you to KWE for being the best supervisor anyone could ask for. Thank you for reading the drafts no matter how bad they were or how ill you might have been. Thank you to AA for identifying the weakest points in the thesis and helping address these rapidly, and thank you for your introduction to optical experiments. I enjoyed every minute in the optics labs that you accompanied me for. Thank you to PW, for many things: for giving me this opportunity, for being the voice of optimism, for accommodating my sporadic nature, etc. Thank you all for the experiences you made possible. Because of you, I have visited many new places and done many things I would never have been able to do without you.

# *List of Publications*

Publications to which the author of this thesis contributed as a main author:

- S. F. Poole, L. X. Barton, M. Wang, P. Manuel, D. Khalyavin, S. Langridge, K. W. Edmonds, R. P. Campion, V. Novák and P. Wadley. 2022. “*Probing the manipulation of antiferromagnetic order in CuMnAs films using neutron diffraction*“. Applied Physics Letters, 121(5), 052402. [Online]. Available: <https://doi.org/10.1063/5.0103390>
- S. F. Poole, O. J. Amin, K. W. Edmonds and P. Wadley. 2023. “*Peltier Controlled Vacuum Chamber for Transport Measurements*”, In Preparation.

Other publications to which the author of this thesis contributed directly:

- S. Reimers, D. Kriegner, O. Gomonay, D. Carbone, F. Krížek, V. Novák, R. P. Campion, F. Maccherozzi, A. Björling, O. J. Amin and L. X. Barton. 2022. “*Defect-driven antiferromagnetic domain walls in CuMnAs films*“. Nature communications, 13(1), pp.1-7. [Online]. Available: <https://arxiv.org/abs/2110.03724>
- M. Wang, C. Andrews, S. Reimers, O. J. Amin, P. Wadley, R. P. Campion, S. F. Poole, J. Felton, K. W. Edmonds, B. L. Gallagher and A. W. Rushforth. 2020. “*Spin flop and crystalline anisotropic magnetoresistance in CuMnAs*“. Physical Review B, 101(9), p.094429. [Online]. Available: <https://link.aps.org/doi/10.1103/PhysRevB.101.094429>
- O. J. Amin, S. F. Poole, S. Reimers, L. X. Barton, F. Maccherozzi, S. S. Dhesi, V. Novák, F. Krížek, J. S. Chauhan, R. P. Campion, A. W. Rushforth, T. Jungwirth, O. A. Tretiakov, K. W. Edmonds, P. Wadley. 2023. “*Antiferromagnetic half-skyrmions electrically generated and controlled at room temperature*“. Accepted by Nature Nanotechnology. [Online]. Available: <https://arxiv.org/abs/2207.00286>
- S. Reimers, O. Gomonay, O. J. Amin, F. Krížek, L. X. Barton, Y. Lytvynenko, S. F. Poole, V. Novák, R. P. Campion, F. Maccherozzi, D. Carbone, A. Björling, Y. Niu, E. Golias, D. Kriegner, J. Sinova, S. S. Dhesi,

M. Kläui, M. Jourdan, K. W. Edmonds, and P. Wadley. 2023. “*Magnetic domain engineering in antiferromagnetic CuMnAs and Mn<sub>2</sub>Au devices*“.  
In Preparation. Pre-print Available: <https://arxiv.org/abs/2302.09550>

# Contents

<b>Abstract</b>	i
<b>Acknowledgements</b>	iii
<b>List of Publications</b>	v
<b>Contents</b>	vii
<b>List of Tables</b>	xii
<b>List of Figures</b>	xii
<b>1 Introduction</b>	1
1.1 Hard Disk Drive Read Heads . . . . .	5
1.2 Switching an Antiferromagnet . . . . .	7
1.3 Thesis Outline . . . . .	9
<b>2 Spintronics in CuMnAs</b>	11
2.1 Tetragonal CuMnAs . . . . .	11
2.2 Antiferromagnetism in CuMnAs . . . . .	14
2.3 Magnetic Anisotropy in CuMnAs . . . . .	16
2.4 Defects and Domain structures in CuMnAs . . . . .	17
2.5 Anisotropic Magnetoresistance (AMR) . . . . .	21
2.6 Spin Flop . . . . .	25
2.7 Néel Order Spin Orbit Torque (NSOT) . . . . .	28
<b>3 Probing the Manipulation of Antiferromagnetic Order in CuMnAs Films Using Neutron Diffraction</b>	31
3.1 Introduction . . . . .	31
3.1.1 Neutron Diffraction . . . . .	32
3.2 Methods . . . . .	35

3.2.1	Neutron Diffraction at WISH . . . . .	35
3.2.2	Transport Measurements in a Cryostat . . . . .	40
3.3	Results . . . . .	43
3.3.1	Neutron Diffraction . . . . .	43
3.3.2	Transport Measurements . . . . .	48
3.3.3	Comparing Neutron Diffraction to Transport . . . . .	53
3.4	Discussion and Conclusions . . . . .	55
4	<b>Optical Probing of Magnetic Ordering in Thin Film CuMnAs Samples</b>	57
4.1	Introduction . . . . .	57
4.2	Relevant Magneto optics . . . . .	62
4.2.1	Polarisation of light . . . . .	62
4.2.2	The Voigt Effect . . . . .	63
4.2.3	Expected Demagnetisation Behaviour in CuMnAs Samples	66
4.3	Optical Pump Probe Techniques . . . . .	71
4.3.1	Ti:Sapphire lasers . . . . .	71
4.3.2	Asynchronous Optical Sampling (ASOPS) . . . . .	72
4.3.3	Delay-Line Pump-Probe . . . . .	73
4.3.4	Descriptions of Ancillary Equipment . . . . .	75
4.3.5	Descriptions of Optical Elements . . . . .	76
4.4	Methods . . . . .	78
4.4.1	Detecting Polarisation Angle Changes in Reflection . . .	79
4.4.2	Detecting Polarisation Angle Changes in Transmission .	82
4.4.3	Detecting Spin Flop in Transmission . . . . .	83
4.4.4	Data Handling . . . . .	86
4.5	Results . . . . .	88
4.5.1	Voigt Effect Changes Observed in Reflection Pump-Probe	88
4.5.2	Voigt Effect Changes Observed in Transmission Pump- Probe . . . . .	92

4.5.3	Spin Flop Detection Using Linear Polarisation Angle Changes in Transmission Mode . . . . .	94
4.6	Conclusions . . . . .	96
<b>5</b>	<b>Optical Determination of CuMnAs Elastic Constants using Strain Pulse Phonon Reflection</b>	<b>97</b>
5.1	Introduction . . . . .	97
5.1.1	Sample Information . . . . .	98
5.2	Methods . . . . .	100
5.3	Strain Pulses and Elastic Stiffness Coefficients . . . . .	102
5.4	Results . . . . .	111
5.5	Conclusions . . . . .	113
<b>6</b>	<b>Design, Development and Testing of a Room Temperature Vacuum System</b>	<b>115</b>
6.1	Introduction . . . . .	115
6.2	Design . . . . .	119
6.3	Manufacture . . . . .	121
6.4	Testing and Results . . . . .	123
6.5	Conclusions . . . . .	126
<b>7</b>	<b>Developing a Pulsed Magnetotransport Measurement Technique for Investigating Néel Order Spin Orbit Torques</b>	<b>129</b>
7.1	Introduction . . . . .	129
7.1.1	Quadratic Magnetic Deflection (QMD) . . . . .	130
7.1.2	The effect of NSOT on Domains and Domain Walls . . . . .	135
7.1.3	Delta-Pulsing . . . . .	138
7.2	Characterisation of Delta Pulsing Signals . . . . .	143
7.2.1	Delta-Pulsing in the RTS . . . . .	143
7.2.2	Delta-Pulsing Field Steps . . . . .	145
7.2.3	Field Sweeps with Continuous High-Current Delta-Pulses	157
7.2.4	Verifications . . . . .	160
7.3	Discussion and Conclusions . . . . .	162

<b>8 Concluding Remarks</b>	<b>164</b>
<b>Bibliography</b>	<b>169</b>
<b>Appendices</b>	<b>176</b>
<b>A List of Abbreviations</b>	<b>176</b>
<b>B Relevant Python Code</b>	<b>178</b>

# List of Tables

2.1	Table of Samples . . . . .	13
5.1	Table for Converting Between Four Dimensional Elasticity tensor and Two Dimensional Elasticity Tensor . . . . .	104
5.2	Table of Non-Vanishing Elasticity Constants for CuMnAs. . . . .	106
5.3	Table of Measured Elastic Constants for CuMnAs . . . . .	113

# List of Figures

1.1	Illustration of Types of Magnetism . . . . .	2
1.2	Illustration of a Simplified Spin Valve Stack . . . . .	6
2.1	Models of the CuMnAs Unit Cell and its Matching with the Substrate . . . . .	13
2.2	Illustration Describing the Néel Vector . . . . .	15
2.3	Ball and Stick Model Showing Symmetry Breaking in the CuMnAs Unit Cell . . . . .	15
2.4	Atomic Resolution Images of Microtwin and Slip Dislocation Defects in CuMnAs . . . . .	18
2.5	Images of the Domain Structure of Uniaxial and Biaxial CuMnAs Films . . . . .	20
2.6	Illustration of a Hall Bar and Measurement Geoemtry of AMR .	22
2.7	Illustration of a Pair of AFM Moments Before and After Spin Flop	25
2.8	Illustration Describing the Effective Fields Resulting From Néel Order Spin Orbit Torque . . . . .	30
3.1	Illustration of Geometry for Neutron Diffraction . . . . .	36
3.2	Example Raw Diffraction Peak Results for Three Different Magnetic Field Strengths from Sample C . . . . .	39
3.3	Schematic of L-bar Devices used for AMR Measurements . . . . .	42
3.4	Neutron Diffraction Raw Peak Results for Sample C . . . . .	44
3.5	Neutron Diffraction Raw Peak Results for Sample B . . . . .	45
3.6	Neutron Diffraction Peak Amplitude Results . . . . .	46

3.7	Summary of Neutron Diffraction Results as Ratios . . . . .	47
3.8	Summary of Sample C Transport Spin Flop AMR Results . . . .	49
3.9	Spin Flop Transport Measurements Showing the Uniaxial Nature of Sample C . . . . .	51
3.10	Spin Flop Transport AMR Results for Sample C with Bi-Directional High Magnetic Field . . . . .	52
3.11	Comparing Neutron Diffraction and Electronic Transport Results for Spin Flop . . . . .	54
4.1	Illustrations of the Faraday and Voigt geoemtries in Magnetoop- tical Measurements . . . . .	58
4.2	Excerpt from Saidl et al. 2017 as a Summary of Voigt Effect Demagnetisation Effects . . . . .	60
4.3	Illustration of a Polariastion Ellipse for Light . . . . .	63
4.4	Illustration of Voigt Effect Induced Changes to Polarisation Ellipticity . . . . .	64
4.5	Illustration of Voigt Effect Induced Changes to Polarisation Angle	64
4.6	Illustration of Expected Reflection Mode Polarisation Angle Changes From the Voigt Effect in Reflection . . . . .	67
4.7	Illustration of Expected Reflection Mode Polarisation Changes From the Voigt Effect in Transmission . . . . .	68
4.8	Illustration of Expected Reflection Mode Polarisation Changes From the Voigt Effect Before and After Spin Flop in Transmission	69
4.9	Schematic Representation of ASOPS Set-up to Measure Polari- astion Angle Changes in Reflection . . . . .	80
4.10	Schematic Representation of Necessary Changes to the ASOPS Set-up in Order to to Measure Polariastion Angle Changes in Transmission . . . . .	83
4.11	Schematic Representation of Delay Line Set-up to Measure Spin Flop Induced Polariastion Angle Changes in Transmission . . .	84

4.12 Polariastion Angle Change Results Measured in Reflection on Sample A . . . . .	89
4.13 Results for Polarisation Angle Change as a Function of Incident Polariastion Angle Measured in Reflection on Sample A . . . . .	91
4.14 Polariastion Angle Change Results Measured in Transmission on Sample B . . . . .	92
4.15 Polariastion Angle Change Results Measured in Reflection Before and After Spin Flop on Sample C . . . . .	95
5.1 Comparison of CuMnAs Growths on GaP(001) and High-Index GaAs Substrates . . . . .	99
5.2 Schematic Representation of ASOPS Set-Up Used to Measure Strain Pulse Echoes in Reflection Mode . . . . .	101
5.3 Illustration of Strain Pulse Propagation Through a CuMnAs Thin Film . . . . .	103
5.4 Reflectivity Change Results Cause by Reflected Strain Pulses . . . . .	112
6.1 Photograph of the RTS . . . . .	118
6.2 Exploded Views of the RTS CAD Drawings . . . . .	120
6.3 RTS Temperature Stability Results . . . . .	123
6.4 Results for Switching in the RTS With and Without Active Temperature Control . . . . .	125
7.1 Illustration of Angles Relevant to QMD . . . . .	131
7.2 Illustration of Domain Wall Motion Caused by Delta Pulsing . . . . .	137
7.3 Illustrations to Summarise the Delta-Pulsing Method . . . . .	139
7.4 Transverse Voltage Delta-Pulsing Results in the RTS on Sample C	144
7.5 Transverse QMD Delta-Pulsing Results in the RTS on Sample C	145
7.6 Transverse QMD Delta-Pulsing Results in a Cryostat with Field Applied Along the Sample C Easy Axis . . . . .	147

7.7 Separated Plots of Transverse Voltage Delta-Pulsing Results in a Cryostat with a 4.5 T Field Applied Along the Sample C Easy Axis . . . . .	149
7.8 Longitudinal QMD Delta-Pulsing Results in a Cryostat with Fields Applied Along the Sample C Easy Axis . . . . .	150
7.9 Transverse QMD Delta-Pulsing Results in a Cryostat with Fields Applied Along Various Axes of Sample C . . . . .	152
7.10 Transverse QMD Delta-Pulsing Results in a Cryostat with 12 T Field Applied Along the Sample C Hard Axis . . . . .	152
7.11 Transverse QMD Delta-Pulsing Results in a Cryostat with Fields Applied Along the Sample E Easy Axis . . . . .	153
7.12 Transverse QMD Delta-Pulsing Results in a Cryostat with Fields Applied Along the Sample E Hard Axis . . . . .	155
7.13 Longitudinal QMD Delta-Pulsing Results Comparing Two Possible Measurement Geometries in a Cryostat with 4.5 T Field Applied Along the Sample C Easy Axis . . . . .	156
7.14 Constant Amplitude Delta-Pulsing AMR Results as a Function of Applied Field Strength along the Sample C Easy Axis . . . . .	158
7.15 Constant Amplitude Delta-Pulsing Transverse AMR Results as a Function of Applied Field Strength along the Sample E Hard Axis . . . . .	159

# Chapter 1

## Introduction

The magnetic order of a material defines the ways in which it can interact with magnetic fields, with each type of magnetism being classified by the different susceptibilities of the material in question. Diamagnetism describes the opposition to an applied field which all materials will exhibit to some extent. Paramagnetic materials are those in which the opposite effect dominates and so an external field will be enhanced by the magnetic moments present in the material through the alignment of unpaired electron magnetic moments with the external field. In the absence of fields, these two types of magnetism maintain no ordering and lead to zero net magnetisation.

In ferromagnetic materials, the magnetic moments of the unpaired electrons interact with their neighbours, acting to align all the moments parallel to each other as illustrated in Fig. 1.1(a). This alignment generates a net magnetic field which can be manipulated through external fields and some magnetisation will persist in their absence [1]. This magnetisation is completely eliminated if the ferromagnet is raised above its magnetic ordering temperature, the Curie temperature  $T_C$ . The first ferromagnetic material, the lodestone (an iron oxide material that naturally forms a net magnetic field without being externally magnetised), was discovered in ancient history and was the basis for the compass as we know it now. The name ferromagnetism comes from the fact that the most common element capable of this type of magnetism is iron (Fe),

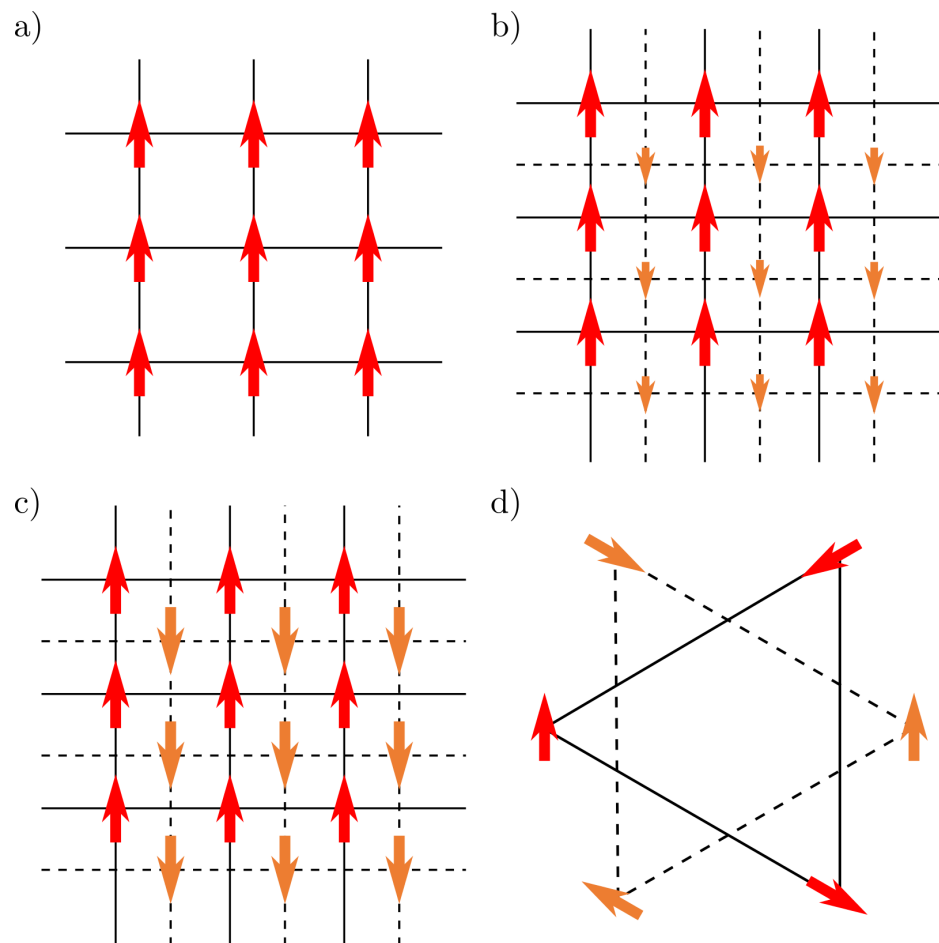


Figure 1.1: Schematic representations of the equilibrium magnetic moment alignments for (a) ferromagnetism, (b) ferrimagnetism, (c) collinear antiferromagnetism, (d) triangular noncollinear antiferromagnetism. Red arrows and solid lines represent one sublattice while orange arrows and the dotted lines represent the second sublattice, where applicable.

materials comprised of which are called ferrous. Only a few elements possess the properties required to express ferromagnetism at room temperature (i.e. having  $T_C \geq 300$  K) and they are: Fe, Ni and Co. Making alloys containing these elements can modify the magnetic susceptibility to enhance or suppress the magnetic properties as desired. There are a few more exotic forms of magnetism such as ferrimagnetism [2, 3] and spin glasses [4], which all have their own uses and interesting physics. Ferromagnetic materials, however, remain the type of magnetic materials most people refer to as magnets when not being more specific. This is most likely because of people's familiarity with the effects of ferromagnets: their attraction to other paramagnetic or ferromagnetic materials. Fridge magnets, magnetic fasteners and navigational compasses all use this property of ferromagnets in their respective applications, as well as uncountable other uses.

Since the development of the theories surrounding electromagnetism, ferromagnetic materials have found innumerable uses by combining magnetic fields generated by the flow of electricity and the passive magnetic fields generated by ferromagnets. In electric motors, magnetic materials are combined with coils of current carrying wire and are used to drive all manner of mechanisms, where in loudspeakers a similar effect is used to drive a cone to recreate sound. Ferromagnets, however, can be used for more than just their ability to convert electrical energy into locomotion e.g. in magnetic storage technologies such as tape cassettes, floppy disks and magnetic stripe storage. Hard disk drives (HDDs) are another magnetic storage in which the direction of the net magnetic field, called the magnetisation vector, is used to store and readout information by using a spinning disk, called the platter, made up of small regions of editable magnetisation. The information is stored by applying a magnetic field to these small regions to align the magnetisation either into or out of the plane of the platter. The information is then read out by using a sensitive magnetic sensor, attached to the read head, capable of exhibiting either a large or small electrical resistance depending on the magnetisation of the adjacent site on the platter,

called a spin valve. Magnetic storage device technology, such as the HDD, has seen an incredible rate of growth and development since the first magnetic core memories were used in the late 1940s, with the storage density rapidly rising from a few bits per cm<sup>3</sup> in the first magnetic core memories to a few hundred Gb/cm<sup>2</sup> in modern heat assisted magnetic recording (HAMR) HDDs [5]. Further developments have led to the invention of magnetic random access memories (MRAMs) and other magnetic memory technologies since [6]. This rise was made possible through developments made in the field of spintronics, a moniker of spin and electronics [7]. The field of spintronics comprises all manner of effects culminating from the interaction of flowing electrical currents with magnetic media, such as ferromagnets.

Antiferromagnets (AFMs), similarly to ferrimagnets and ferromagnets, have a magnetic structure in which the magnetic moments interact with their neighbours. The difference between these three, however, is that where the exchange interaction between neighbouring moments in a ferromagnet act to align the moments, in ferrimagnets and antiferromagnets, the exchange interaction instead acts to align each neighbour antiparallel. In ferrimagnets, there are two sublattices formed, one with large magnetic moments aligned in one direction, and another where the moments are smaller than the first, and are aligned antiparallel as illustrated in Fig. 1.1(b). This leads to a suppression of the net magnetic moment and some other interesting effects [3]. Antiferromagnets, however, do not have different size magnetic moments on each sublattice. The simplest form of antiferromagnetism is the collinear fully compensated antiferromagnet in which there are two perfectly antiparallel sublattices with equal magnetic moments in each as illustrated in Fig. 1.1(c). This configuration creates a material with high magnetic ordering but zero net magnetisation, no stray fields and a low magnetic susceptibility. This means that AFMs are robust to external magnetic fields, have zero crosstalk between neighbouring devices and have very fast magnetic dynamics ( $\sim$  THz) [8, 9]. The magnetic ordering temperature of an AFM is called the Néel temperature,

$T_N$ , and AFMs exist with a wide range of Néel temperatures, for example  $T_N = 4.6$  K in EuSe [10] and  $T_N = 825$  K in CuFeS<sub>2</sub> [11].

Antiferromagnetism also exists without being fully compensated (having some stray field through incomplete anti-alignment of the sublattices) and without being collinear (by having three or more directions in which the moments point) which lead to their own sets of interesting physics (e.g. Ref. 12). An example of one noncollinear, fully compensated configuration is illustrated in Fig. 1.1(d), but there are many more possible configurations of antiferromagnetism. For the sake of this thesis, the focus will be on collinear, fully compensated antiferromagnets despite the fact that the first application, the spin valve in a read head for a HDD, typically uses the non-collinear AFM, IrMn, as a pinning layer [13, 14]. Before this application, AFMs were considered to be theoretical interest but were lacking practical application [15, 16]. Since then, AFMs have risen to prominence with respect given to their numerous phenomena having implications for standalone applications (such as for MRAMs) and in structures combining FMs with AFMs, such as the aforementioned spin valves, which find use in magnetic sensors ranging from automotive, medical or computing technologies such as hard disk drives (HDDs) [14, 17].

## 1.1 Hard Disk Drive Read Heads

The active elements in the magnetic sensors used in HDD read heads previously utilised giant magnetoresistance (GMR) and now use tunneling magnetoresistance (TMR) in order to create a spin valve. These spin valves are multilayer structures in which the observed resistance experienced by a current flowing through the structure depends on the relative alignment of two FM layers. The free layer is composed of an FM layer with low coercivity such that it can easily be reoriented by the presence of an adjacent site on the HDD platter while the fixed FM layer is composed of an FM material which has its magnetisation direction pinned by an adjacent AFM material through the created exchange

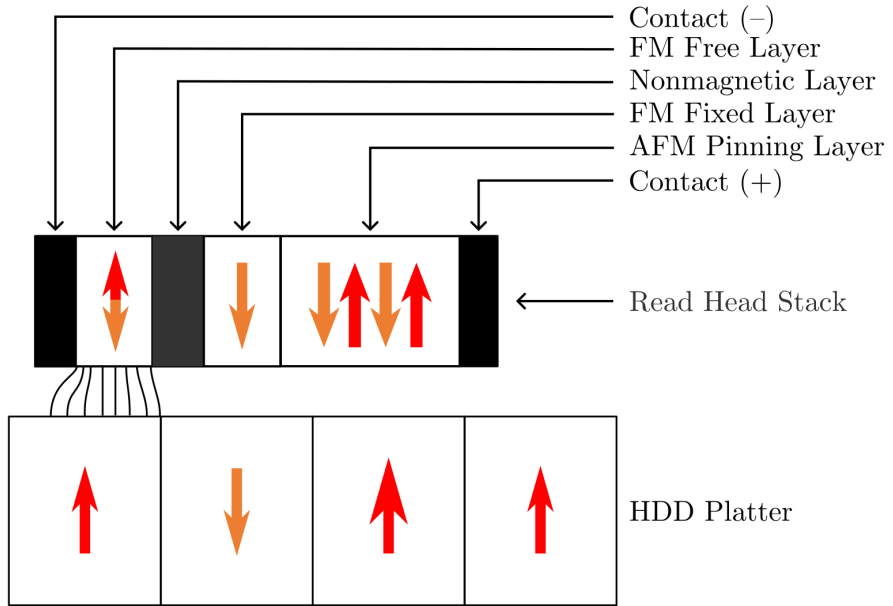


Figure 1.2: Illustration of GMR/TMR read head spin valve stack used in hard disk drive read heads. Red and orange arrows indicate magnetisation directions and the thin curved lines indicate the stray field from the measured site on the platter.

bias. The two FM layers are separated by a non-magnetic layer to eliminate the coupling between the two FM layers. Figure 1.2 illustrates the layered structure present in a GMR or TMR spin valve based read head, where the type of non-magnetic spacer layer determines the effect used. In GMR sensors, the spacer layer is electrically conductive and so a current flowing through the structure becomes spin polarised when passing through one FM layer and experiences a low resistance through the stack when the second layer's magnetisation is parallel to the first, however the resistance becomes much higher when the layers are aligned antiparallel due to increased scattering [18]. In a TMR sensor, the spacer layer is electrically insulating and so the current flow depends on quantum tunneling. The tunneling resistance is lowest when the magnetisation of the FM layers is parallel because the density of states of each material are similar, while an antiparallel configuration reduces the similarity between the density of states and leads to a larger resistance. The change in relative resistance as a result of GMR can be  $\Delta R/R_0 \approx 100\%$  [19] at room temperature while the observed change in resistance in a TMR sensor

can be much larger, reaching  $\sim 1000\%$  at 5 K and  $\approx 500\%$  at room temperature [20]. Due to the larger resistance signals possible, TMR based magnetic sensors have replaced GMR based sensors in HDD read heads [21, 22].

## 1.2 Switching an Antiferromagnet

In FMs, spin transfer torque (STT), a non-relativistic effect, has been demonstrated as capable of switching a free layer of an FM by polarising a current in a fixed layer and injecting the polarised current into an FM free layer. This allowed for the writing and reading from ferromagnetic MRAM cells [6]. This same STT was proposed as a means to efficiently reorient an AFM, however was strongly limited by defects and thermal effects in real materials and was only possible at low temperatures [23]. The spin orbit torque (SOT), which arises due to spin-orbit coupling (SOC), creates a non-equilibrium spin polarization as a result of the spin Hall effect or Rashba effect. It is also SOC which causes anisotropic magnetoresistance (AMR) through scattering of electrons. Néel order spin orbit torque (NSOT) only exists in AFMs which also exhibit the inverse spin galvanic effect (ISGE) with opposite sign in each sublattice, in which a current flowing through the material splits into staggered spin-polarised currents acting separately on each magnetic sublattice of the material. This is only possible in materials with combined broken time reversal and broken local inversion symmetry. In AFMs, opposite ISGE in each sublattice leads the same SOT acting on each sublattice so that they rotate in the same sense while remaining antiparallel to each other. If the SOT is considered to be a result of an effective field, this leads to the generation of staggered effective fields which do not act oppositely on each sublattice and leads to a net torque called Néel order spin orbit torque (NSOT), which acts to efficiently reorient the moments in compatible AFMs [24].

Studies have been reported which explore the use of NSOT to reorient two AFM thin film materials, CuMnAs and Mn<sub>2</sub>Au. Both of these materials have

the necessary symmetry breaking to exhibit NSOT (See Section 2.7 for more details) through the application of in plane electrical currents [24]. Wadley et al. [25] first demonstrated using CuMnAs as a memory cell by applying electrical currents to both write information, through NSOT, and read it back as changes in anisotropic magnetoresistance (AMR) (see Section 2.5). This spurred a wealth of surrounding research, both in experimental experiments and theoretical explorations. Since, NSOT switching in CuMnAs such as creating a multi-level memory cell [26], applying writing pulses with an alternative geometry [27], THz electrical switching [28, 29], optically induced resistivity changes [30] and using significantly higher writing current densities to induce domain shattering [31]. In these switching effects, domain wall motion is also very prevalent and may contribute to the signals. To investigate this, studies imaged the magnetic domain structure of CuMnAs before and after applying writing pulses [26, 27, 32] while theoretically works have explored expected domain wall motion and discovered that NSOT should induce high velocity domain wall motion [33, 34] with the aim of developing AFM racetrack memories. These developments highlight the possible capabilities of CuMnAs for standalone memory or storage applications, however there persists the challenge of small readout signals from AMR, since the change in resistance measured for a full reorientation of moments through spin flop gives a total signal of  $\sim 0.1\%$  while the measured signals as a result of NSOT switching can be even smaller ( $\sim 0.05\%$ ) [25, 27] and a lack of understanding of the exact responses during writing pulses. Therefore, attempts to create more accessible techniques for imaging domain structure, without the need for the large facilities necessary for X-ray linear magnetic dichroism photoemission electron microscopy (XMLD-PEEM), and ways to extract more information from the AMR signals are being investigated. The Voigt effect was shown to be capable of determining the Néel vector of an AFM [35] with the aim of using the same effect to develop an imaging technique, while progress has been made toward spin-Seebeck [36] or magneto-Seebeck [37] microscopies capable of

the same. Developments have been made toward extracting more information in electrical transport measurements by using second-order AMR effects by Olejnik et al. [28] but the presented signals are even smaller than for the first order changes. This still leaves a desire for robust and convenient tools for detecting and understanding spintronic effects in AFMs. Since the first report of growth of Mn<sub>2</sub>Au in 2013 [38], parallel progress has been made toward standalone AFM spintronic devices using Mn<sub>2</sub>Au in place of CuMnAs such as in switching [39–41], and investigating the associated mechanisms such as thermal activation [42], imaging the switching using XMCD-PEEM [43], and studying magnetoresistance [44] in Mn<sub>2</sub>Au, another collinear AFM with a high Néel temperature ( $> 1000$  K).

### 1.3 Thesis Outline

The studies contained in this thesis aim to assist in the development of accessible lab-based techniques capable of imaging the magnetic changes in CuMnAs switching devices or extracting more information from the existing transport approaches. For the studies contained, films of CuMnAs are used so, before describing any specific studies, Chapter 2 introduces the magnetic and structural properties of CuMnAs then describes the origins of the following spintronic effects: AMR, spin flop and NSOT. In the development of accessible techniques, a predictable and reliable method for manipulating the magnetic ordering of a CuMnAs is necessary. Spin flop is used to this end, in which a sudden 90° reorientation of the magnetic moments is induced by applying a large ( $\sim 1.5$  T) external magnetic field parallel to the magnetic moments in the material (see Section 2.6). Wang et al. studied spin flop in CuMnAs in detail [45], however the techniques used were incapable of determining the full extent of reorientation throughout the thickness of the film because the transport measurements only measure relative changes in AMR and the X-ray technique was surface sensitive only. This leaves the question, is spin flop a

bulk effect or is reorientation only possible at the surface while moments near the substrate interface are pinned by some growth anisotropy? Chapter 3 aims to answer this question. Chapter 4 aims to develop a rapid technique capable of determining if a CuMnAs is uniaxial or biaxial, and then aims to detect spin flop using the optical polarisation changes induced by the Voigt effect to further the understanding magneto-optical measurements in CuMnAs based on the works by Saidl et al [35]. Chapter 5 uses similar optical techniques to measure the elastic constants in CuMnAs, for possible use in future magneto-elastic simulations. Chapter 6 describes the design, manufacture and testing of a vacuum system designed to keep samples in an oxygen free environment while at a constant temperature near to ambient conditions, which proved to be directly useful in NSOT induced switching experiments. Chapter 7 investigates the use of short duration, amplitude current pulses to induce large NSOT AMR changes to further the second-harmonic investigations performed by Godinho et al. [46]. The thesis concludes by summarising the results and any other important discoveries found along the way in Chapter 8.

# Chapter 2

## Spintronics in CuMnAs

The following sections describe a simple magnetic model of CuMnAs, describe its crystal and magnetic structure and explore the origins of the observed domain structures in various samples. Following this, the origins of magnetic anisotropy, the importance of defects and descriptions of anisotropic magnetoresistance, spin flop and Néel order spin orbit torques are all discussed.

### 2.1 Tetragonal CuMnAs

The studies contained in this thesis are all conducted in the pursuit of knowledge necessary to develop, or making progress directly applicable to, techniques capable of convenient determination of magnetic states in AFMs. For all the studies, epitaxially grown films of the fully compensated, collinear, antiferromagnetic semi-metal, CuMnAs, were used. The Néel temperature of CuMnAs has been measured to be  $480 \pm 5$  K [47]. The semimetallic properties lead to sheet resistivities of  $\sim 160 \mu\Omega\text{cm}$  at room temperature [25] and the crystal symmetry (see Chapter 2) is suitable for the generation of NSOT. These properties make CuMnAs an ideal candidate for room temperature spintronic applications.

The details of all layers used are contained in Table 2.1. The CuMnAs layers used were mostly epitaxially grown on GaAs(001) or GaP(001) substrates and in both cases, the CuMnAs unit cell lattice matches with a  $45^\circ$  rotation

of the  $a = b$  principal axes compared to the substrate  $a = b$  principal axes. This means that the CuMnAs[100] is parallel to GaP/GaAs[110] while the CuMnAs[001] axis points directly perpendicular to the substrate surface. This is illustrated in Fig 2.1(b) while Fig 2.1(a) illustrates the CuMnAs unit cell. When grown on GaP(001), the CuMnAs film has < 1 % mismatch between the  $a = b$  length of CuMnAs to the half diagonal of the substrate and results in a fully strained growth up to thicknesses of  $\approx$  130 nm. In GaAs, the mismatch is close to 5 % and therefore the strain does not persist beyond a few monolayers, instead forming a relaxed layer with mosaic block structures present [47, 48]. The growths on the high index substrates (GaAs(113)/GaAs(112)) are more complicated and are explained in Chapter 5 where they are exclusively used.

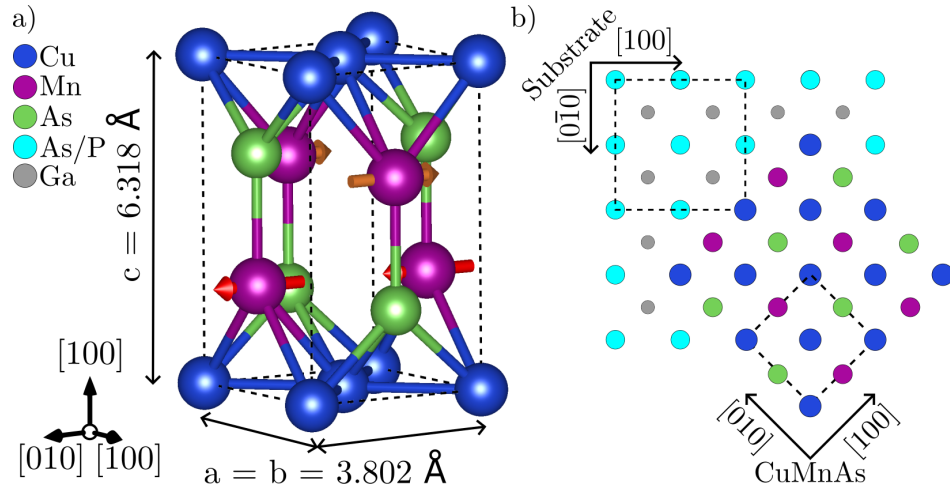


Figure 2.1: (a) Ball and stick model of the unit cell of tetragonal CuMnAs with magnetic sublattices drawn in red and orange arrows. (b) Birds eye view of the unit cell matching between a GaAs/GaP(001) substrate and CuMnAs.

Label	Name	Structure	Substrate	Other Details
A	RC171	2.5 nm Al 20 nm CuMnAs 1.08 $\mu\text{m}$ SL	GaAs	GaAs/AlGaAs Super Lattice Uniaxial
B	RC123	2.5 nm Al 20 nm CuMnAs 100 nm GaP	GaP	Uniaxial
C	RC194	2.5 nm Al 45 nm CuMnAs 200 nm GaP	GaP(S)	Uniaxial
D	RC124	2.5 nm Al 50 nm CuMnAs 100 nm GaP	GaP	Biaxial
E	C219	3 nm Al 50 nm CuMnAs 100 nm GaP	GaP	Grown in Prague Biaxial
F	RC134	5 nm Al 200 nm CuMnAs 30 nm GaP	GaP(001)	
G	RC202	2.5 nm Al 200 nm CuMnAs 200 nm GaAs	GaAs(311)	
H	RC214	2.5 nm Al 200 nm CuMnAs 200 nm GaAs	GaAs(211)	

Table 2.1: Table of materials used in the studies containing: the shorthand labels used in the text and corresponding sample name from growth records, layer structure, substrate information and other details, including magnetic structure.

## 2.2 Antiferromagnetism in CuMnAs

The magnetic structure of CuMnAs can be considered as two antiparallel magnetic sublattices composed of antiparallel magnetic moments  $\underline{m}_1$  and  $\underline{m}_2$  centered on the Mn sites with the magnetisation of each sublattice being  $\underline{M}_1$  and  $\underline{M}_2$ . The total magnetisation is then given by  $\underline{M} = \underline{M}_1 + \underline{M}_2$  which is zero in the equilibrium state since  $\underline{M}_1 = -\underline{M}_2$ . Because this is zero, the AFM magnetic direction is referred to by the Néel vector, defined as  $\underline{L} = \underline{M}_1 - \underline{M}_2$ . In the equilibrium state, the Néel vector points parallel to  $\underline{M}_1$  and has double the magnetisation of each sublattice. These vectors are illustrated in Fig. 2.2 for clarity.

The CuMnAs unit cell is bulk centrosymmetric in the P4/mnn tetragonal space group (a specific form of the P4/mmm point group) but the unit cell exhibits two broken symmetries, illustrated in Fig. 2.3. When the magnetic moment of each Mn site is considered, the unit cell has broken time reversal symmetry as illustrated by Fig. 2.3(a). Despite the bulk inversion symmetry, when the lattice is divided into two sublattices, the sublattices each, individually, have broken spatial inversion symmetry and form inversion partners as illustrated in Fig 2.3(b) [46–48]. It is this broken spatial inversion symmetry that leads to the generation of a non-homogenous spin polarisation in a current flowing in the plane. The staggered spin polarisation means that each sublattice experiences oppositely polarised current, and thus each sublattice experiences an opposite inverse spin galvanic effect (ISGE) [23, 49]. When the spatial inversion and time reversal operations are combined, a new symmetry is returned allowing for a different consideration of the symmetry not possible when considering them individually.

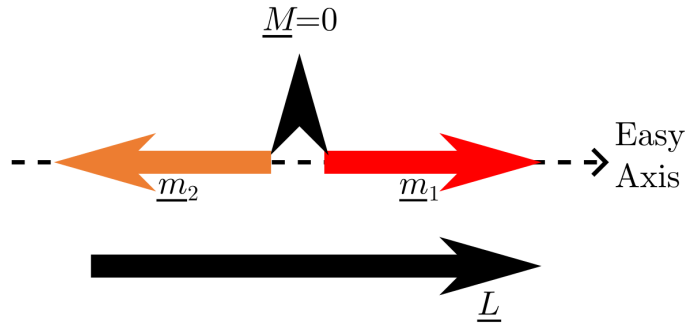


Figure 2.2: Illustration of the equilibrium state for a pair of uniaxial antiferromagnetic sublattices ( $\underline{m}_1$  and  $\underline{m}_2$ ) and corresponding magnetisation vector ( $\underline{M}$ ) and Néel vector ( $\underline{L}$ ).

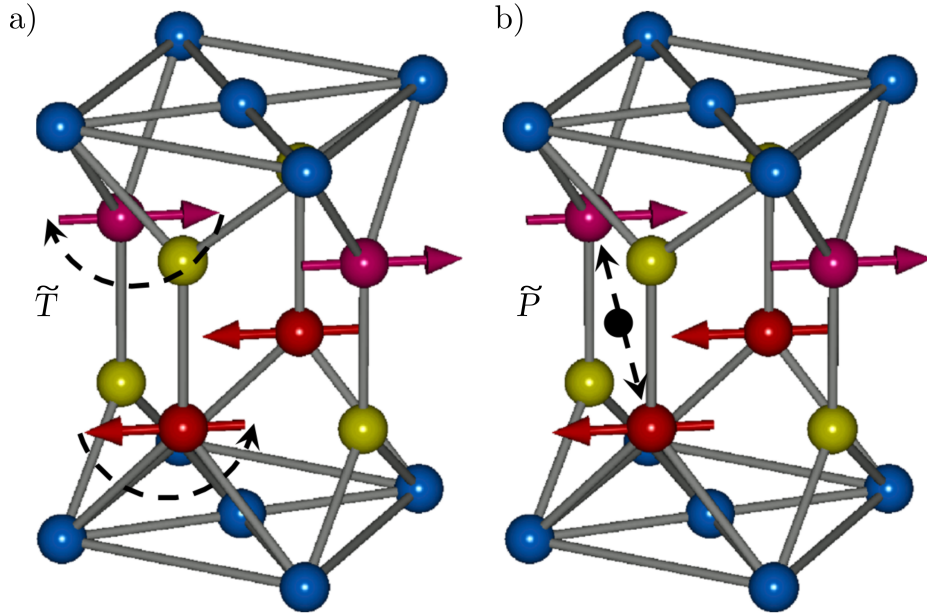


Figure 2.3: Ball and stick models illustrating time reversal and space inversion operations in the CuMnAs magnetic lattice. In (a) the time reversal operation,  $\tilde{T}$ , flips the magnetic moments thus breaking the symmetry. In (b) the black point shows the inversion center of the space inversion symmetric non-magnetic lattice. Under the space inversion operation,  $\tilde{P}$ , the exchange of magnetic atoms around the black point does not leave the antiferromagnetic lattice invariant so the space inversion symmetry is broken. When combined, the  $\tilde{P}\tilde{T}$  operation maintains symmetry even in the antiferromagnetic state. Figure adapted from Ref. 46)

## 2.3 Magnetic Anisotropy in CuMnAs

Magnetic anisotropy describes the preference for magnetic moments to lie along certain directions. Due to its tetragonal symmetry, CuMnAs exhibits strong anisotropy which prevents the magnetic moments from leaving the *ab* plane. This magnetocrystalline anisotropy arises from spin orbit coupling which connects the crystalline structure to the magnetic structure such that, in thick layers, biaxial anisotropy is exhibited with two equivalent easy axes (preferential crystal directions). These easy axes lie along the [110] and [1 $\bar{1}$ 0] crystallographic directions with the [100] and [010] directions being hard axes. In thin films ( $\leq 20$  nm), the anisotropy is uniaxial, i.e. dominated by a single axis, with the easy axis parallel to one of the equivalent [100] or [010] directions [47, 48]. For the sake of this thesis, the uniaxial easy axis is chosen to be along the [010] direction in all cases. The anisotropy energy of a uniaxial system takes the following form

$$E_{\text{uniaxial}} = -\frac{k_u}{2} \cos^2(\theta) \quad (2.1)$$

where  $k_u$  is the uniaxial anisotropy energy constant per atom and  $\theta$  is the angle of the moment relative to the [010] easy axis. For the biaxial case, the angular dependence has twice the frequency and is offset by 45° leading to

$$E_{\text{biaxial}} = -\frac{k_c}{2} \sin^2(2\theta) \quad (2.2)$$

where  $k_c$  is the biaxial anisotropy energy constant per atom and  $\theta$  is the angle between the magnetic moment and the [010] crystallographic axis which is a hard axis in biaxial CuMnAs. The factor of two in each equation is to account for the split of the anisotropy energy between each sublattice. The uniaxial anisotropy is not caused by the bulk crystal symmetry but is supposed to originate from some anisotropy at the growth interface which is not fully understood [47, 50]. Only one layer, Sample C, is thicker (45 nm) while exhibiting strong uniaxial anisotropy and this property made it uniquely

desirable for some studies contained herewithin.

## 2.4 Defects and Domain structures in CuMnAs

In CuMnAs thin films, the domain structure is known to be affected by defects though the full picture of the domain formation is not well understood [52]. Two prevalent growth defects have been identified as microtwin defects and anti-phase boundaries as a result of slip dislocations [51]. Figure 2.4 shows high-angle annular dark-field imaging scanning tunneling electron microscopy (HAADF-STEM) images of these defects. These images show contrast between atoms present in slices of crystals such that the crystal structure can be inspected. Figure 2.4(a) demonstrates microtwin defects that are growth defects presenting as stripes of rotated CuMnAs unit cells which propagate diagonally from the substrate interface through to the surface. In these cases, the defect unit cells have their c-axis rotated through  $\approx 82^\circ$  away from the substrate surface normal. These regions have been shown to force the orientation of the moments at the surface near where these defects terminate [53]. The slip dislocations illustrated in Fig. 2.4(b) are atomically sharp boundaries in which the CuMnAs unit cell is offset by  $c/2$ . This means that the bottom Mn atom on one side of the boundary is adjacent to the top Mn atom in the neighbouring unit cell, thus creating an anti-phase boundary. This is possible because the growth of CuMnAs can initiate on either of the possible As layers (labelled As<sub>1</sub> and As<sub>2</sub> in Fig. 2.4(b)). These anti-phase boundaries are implicated in the formation of holes which sometimes arise on the grown surface of CuMnAs samples [51] and have been shown to create atomically sharp domain walls [54]. These holes play a part in the observed domain structure because edge effects can introduce an additional anisotropy contribution [55] while the atomically sharp domain walls are below the detection resolution of X-ray linear magnetic dichroism photoemission electron microscopy (XMLD-PEEM) and therefore make XMLD-PEEM images more difficult to interpret..

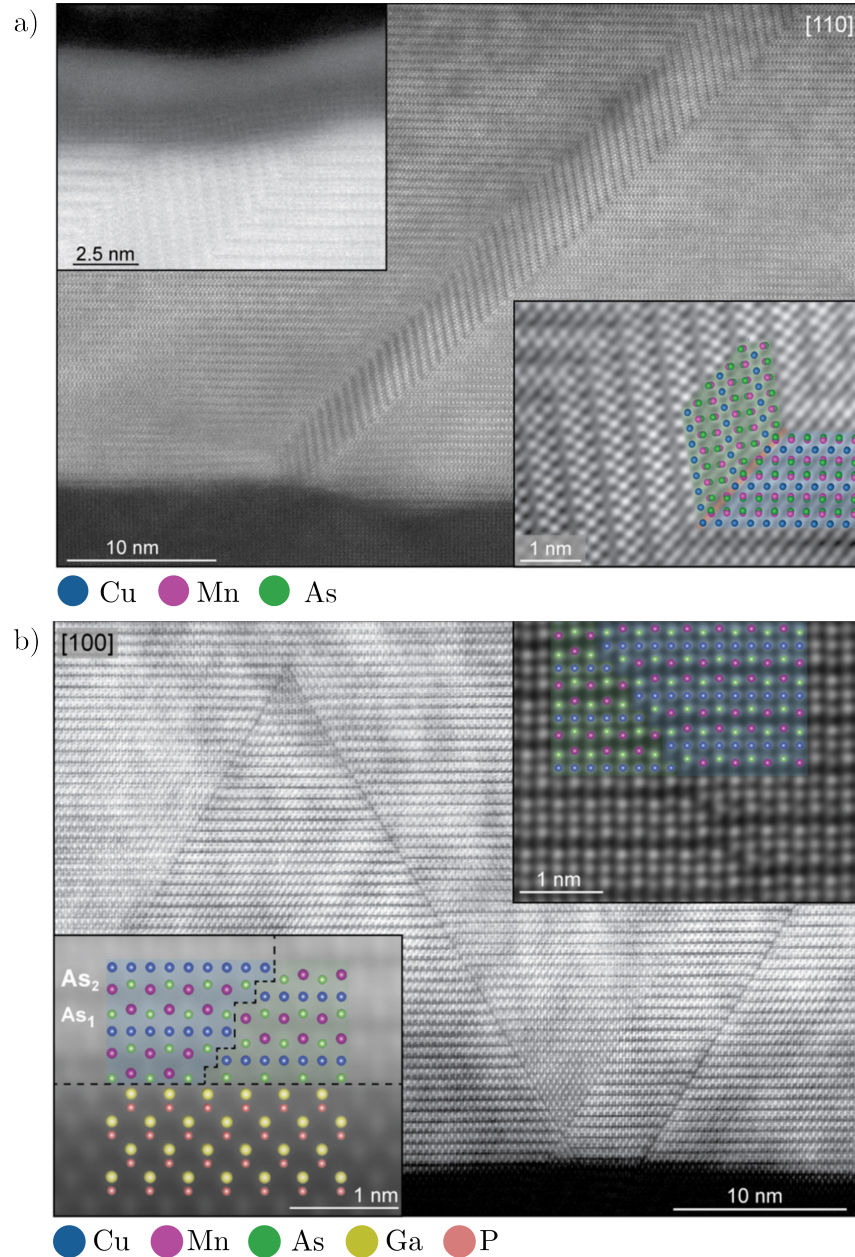


Figure 2.4: High-angle annular dark-field scanning tunneling electron microscopy (HAADF-STEM) images of a 50 nm thick layer of CuMnAs where (a) shows a twinlike structural defect propagating throughout the film, viewed from [110] CuMnAs direction and (b) shows slip dislocations in the same sample viewed from the [100] CuMnAs direction. The insets show zoomed in images to highlight features. The upper inset in (a) shows the CuMnAs-Al capping layer interface and the lower inset shows the expected crystal structure within the defect with the atoms coloured as blue for Cu, purple for Mn, and green for As. The upper inset in (b) shows the slip dislocation with the same colours overlaid while the lower inset shows the CuMnAs-GaP interface (Ga in yellow and P in orange) where the crystal is seeded starting with either the As<sub>1</sub> or As<sub>2</sub> layer of CuMnAs. Figure adapted from Ref. 51.

The domain structures presented in uniaxial and biaxial CuMnAs have been imaged using XMCD-PEEM. XMCD-PEEM makes an image of the domain structure of CuMnAs by taking PEEM images of the sample using two perpendicular X-ray polarisations. The difference in brightness between these two images is then calculated. This yields an image with contrast between different Néel vector orientations because linearly polarised X-rays, of a suitable energy, will experience dichroism. In CuMnAs, this dichroism is specifically the difference in Mn  $L_{2,3}$  absorption rates between polarisations parallel and perpendicular to the local magnetic moments. The absorption depends on the square of local magnetisation and therefore is present in AFMs and is detected in the relative angle of the Néel vector, however the technique cannot distinguish between Néel vectors separated through  $180^\circ$  [47].

Examples of XMCD-PEEM images are contained in Fig. 2.5 where (a-b) are images of the uniaxial domain structure of Sample C, and (c-d) are images of biaxial Sample E. Because the contrast in XMCD-PEEM is not capable of distinguishing between antiparallel Néel vectors, the images only show contrast between  $90^\circ$  changes in Néel vectors. By varying the incident angle of polarisation, the contrast can be chosen to create light(dark) regions for moments parallel(perpendicular) to an easy axis, or it can be chosen to be at  $45^\circ$  to the easy axis to show all domains with the same contrast while highlighting domain walls. Figures (a,c) have the incident polarisation chosen to maximise contrast in the domains while (b,d) have it chosen to detect contrast within the domain walls. The images in (a,b) shown that Sample C contains domains only along the [010] easy axis. The lines visible in these images show deviations from the easy axis for some moments, however these lines do not always form closed loops. This suggests the presence of spin textures which are not resolvable in XMCD-PEEM (resolution limited to  $\approx 10$  nm). Overall Sample C exhibits a uniaxial domain structure with large domains ( $> 100$   $\mu\text{m}$ ) and very few moments lying within domain walls. The biaxial Sample E presented in (c,d) exhibits smaller domains ( $\sim 1$   $\mu\text{m}$ ) with moments oriented along the [110] and

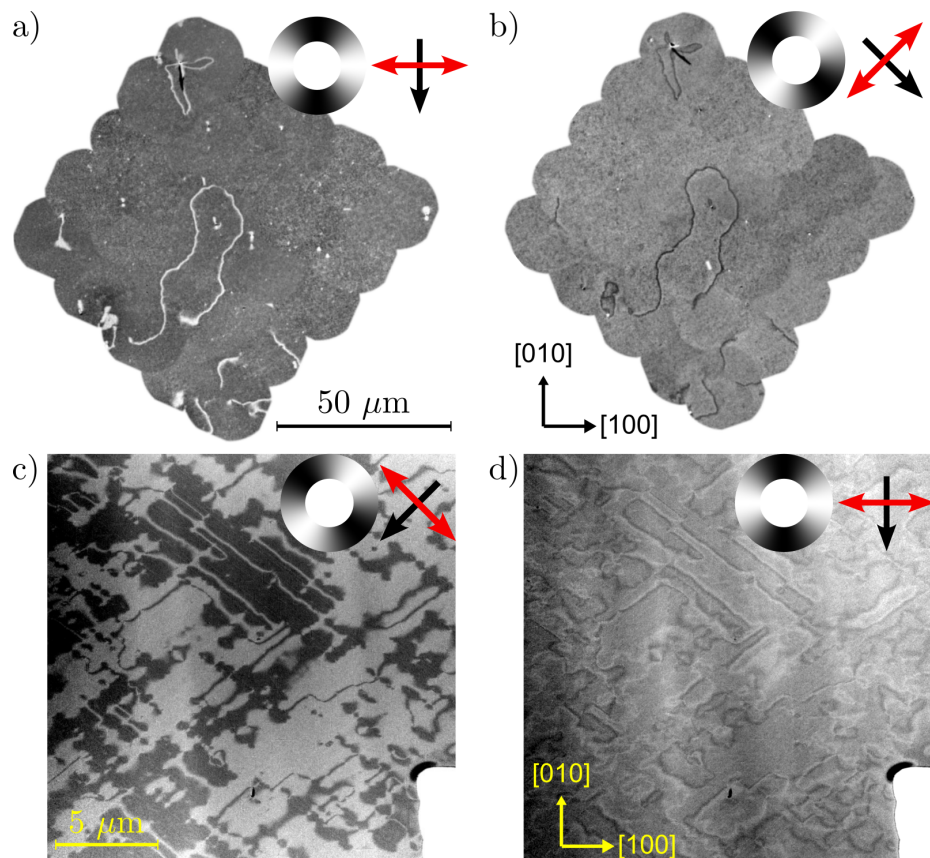


Figure 2.5: XMLD-PEEM images of (a,b) a large area map of uniaxial domains achieved by stitching smaller images taken on Sample C, indicating an easy axis along the  $[010]$  direction and (c,d) biaxial Sample E with easy axes along  $[110]$  and  $[1\bar{1}0]$ . The black arrows indicate the surface projection of the incident X-ray direction while the red arrow shows the projected incident polarisation.

[1̄10] directions with both 90° and 180° domain walls visible. The images in (b,d) highlight the different chiralities (rotation directions) of domain walls possible where some domain walls go from light to dark while others go from dark to light in the 180° domain walls, while there are four possible domain wall types present in (d).

The above images give no indication of a preference for one Néel vector direction over another in large free regions of biaxial materials. It is not possible to distinguish the L-vector in uniaxial samples and there is no evidence for an energetically preferable direction for  $\underline{L}$  in uniaxial CuMnAs. This suggests the presence of an even domain population, but recent studies have worked to progress the understanding of the domain structure in patterned samples by studying shape anisotropies in CuMnAs samples. A shape anisotropy is a localised modification to the magnetic anisotropy near the patterned edge of a device which results in a preference for the magnetic moments to align perpendicular to the patterned edge [55]. For large devices and free regions, the shape anisotropy is not relevant but in studies with large domains ( $\sim 1 \mu\text{m}$ ) and small patterned features ( $\sim 5 - 10 \mu\text{m}$ ), the shape anisotropy must be considered. In these cases, the system is likely to have an unequal population of each domain type. This must be taken into account when considering, for example, the expected outcome of the measurements conducted in Chapter 7.

## 2.5 Anisotropic Magnetoresistance (AMR)

Anisotropic magnetoresistance (AMR) is the observed difference in electrical resistivity as a function of applied current direction with respect to the crystal structure and the local magnetisation. The extent of AMR is proportional to the square of the local magnetic moment such that it is present in many AFMs [46]. The angular dependence of the electric field,  $\underline{E}$ , resulting from an applied current,  $\underline{J}$ , in an AFM with Néel vector,  $\underline{L}$ , in the absence of external

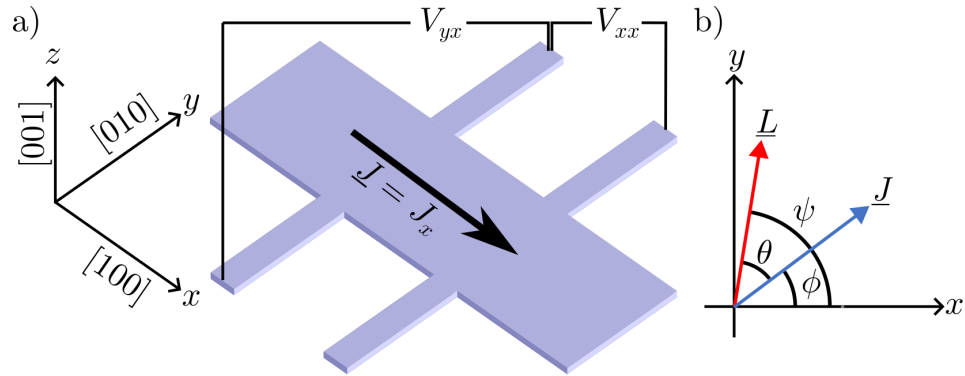


Figure 2.6: Summary of the geometry of AMR measurements in CuMnAs thin films. (a) Illustrates a Hall bar device geometry and the chosen cartesian coordinates, defined based on the crystallographic directions of the CuMnAs unit cell as drawn. (b) Illustrates the definitions of the in plane angles used to describe the direction of Néel vector,  $\underline{L}$ , and the applied current,  $\underline{J}$ , direction with respect to each other and the *x*-axis.

field (and therefore zero Hall resistivity) can be written

$$\underline{E} = \hat{l}(\underline{J} \cdot \hat{l})[\rho_{\parallel} - \rho_{\perp}] + \rho_{\perp} \underline{J} \quad (2.3)$$

from Ohm's law [56], where  $\hat{l} = \underline{L}/|\underline{L}|$ , and  $\rho_{\parallel}$  and  $\rho_{\perp}$  are the resistivities for a current flowing parallel and perpendicular to the Néel vector, respectively.

Figure 2.6 illustrates the geometry of a Hall bar that could be used to measure AMR where (a) shows a 3D representation of a Hall bar, including the definitions of the chosen cartesian system and (b) illustrates the angles  $\theta$ ,  $\psi$  and  $\phi$  which are defined as follows:  $\theta$  is the angle between  $\underline{L}$  and  $\underline{J}$ ,  $\psi$  is the angle between  $\underline{L}$  and the  $[010]$  crystallographic direction which is the *x*-axis, and  $\phi$  is the angle of the current relative to the *x*-axis. The indicated voltages  $V_{xx}$  and  $V_{yx}$  correspond to measured voltages proportional to the electric fields  $E_x$  (parallel to the current) and  $E_y$  (transverse to the current) respectively. In CuMnAs, with no external field applied and the current applied in the illustrated plane. The in-plane current is given by  $\underline{J} = (J \cos \phi, J \sin \phi, 0)$  with

$\hat{\underline{J}} = (\cos \psi, \sin \psi, 0)$ , and  $\theta = \psi - \phi$ . Substituting these terms into Eq. 2.3 yields

$$\begin{pmatrix} E_x \\ E_y \\ 0 \end{pmatrix} = \rho_{\parallel} J \begin{bmatrix} \cos(\psi) \cos(\theta) \\ \sin(\psi) \cos(\theta) \\ 0 \end{bmatrix} + \rho_{\perp} J \begin{bmatrix} \sin(\psi) \sin(\theta) \\ -\cos(\psi) \sin(\theta) \\ 0 \end{bmatrix} \quad (2.4)$$

which indicates that the electric field is parallel to the current whenever the Néel vector is parallel or perpendicular to the applied current and so  $E_y \neq 0$ , in all other cases. If the chosen current direction is fixed, such as  $\underline{J} = (J_x, 0, 0)$ , then  $\theta \rightarrow \psi$  and Eq. 2.4 can be calculated for three current directions to illustrate the expected form of  $E_x$  and  $E_y$ . Using  $\psi = 0$ ,  $\psi = \pi/4$  and  $\psi = \pi/2$  gives  $\underline{E} = J_x(\rho_{\parallel}, 0, 0)$ ,  $\underline{E} = J_x/2(\rho_{\parallel} + \rho_{\perp}, \rho_{\parallel} - \rho_{\perp}, 0)$  and  $\underline{E} = J_x(\rho_{\perp}, 0, 0)$ , respectively. With this fixed current direction, the real measured resistance can be determined by using standard conversion, which requires the length  $d$  and cross sectional area  $A$  to be known, from resistivity to resistance  $R = \rho A/d$ , from electric field to voltage  $V = -Ed$  and from current density to applied current  $I = JA$ . The measured linear resistance is then given by  $R_{xx} = V_{xx}/I$  and the transverse resistance is given by  $R_{yx} = V_{yx}/I$ . Fully written these give

$$R_{xx} = R_0 + \gamma \cos(2\psi) \quad (2.5)$$

$$R_{yx} = \gamma \sin(2\psi) \quad (2.6)$$

where

$$\gamma = \frac{1}{2}[R_{xx}(\underline{L} \parallel \underline{J}) - R_{xx}(\underline{L} \perp \underline{J})] \quad (2.7)$$

is a simplified AMR constant and  $R_0 = 1/2[R_{xx}(\underline{L} \parallel \underline{J}) + R_{xx}(\underline{L} \perp \underline{J})]$  is the base resistance for a given current direction.

This form of AMR is useful for detecting the change in AMR for a fixed geometry while manipulating the magnetic ordering, however in real crystals, the same crystalline anisotropy that causes magnetic anisotropy also leads to an relationship between the resistance and the crystallographic direction along

which the current flows. Therefore, the above definition for the resistivity difference measured in AMR does not fully describe the angular dependence. There are AMR contributions from crystallographic and non-crystallographic terms in the AMR which require four constants to fully describe in the longitudinal AMR. These can be written [45]

$$\frac{\Delta R_{xx}}{R_{av}} = C_I \cos(2\theta) + C_U \cos 2\psi + C_C \cos 4\psi + C_{I,C} \cos(4\psi - 2\theta) \quad (2.8)$$

where  $\Delta R_{xx}$  is the difference between the measured resistance and the average non-crystalline term ( $\Delta R_{xx} = R_{xx} - R_{av}$ ) and  $R_{av}$  is given by

$$R_{av} = \int_0^{2\pi} \frac{R_{xx}}{2\pi} d\phi. \quad (2.9)$$

which is the resistance averaged over all in plane angles. The four constants,  $C_I$ ,  $C_U$ ,  $C_C$  and  $C_{I,C}$  correspond to the purely non-crystalline term, the uniaxial anisotropy term, the cubic anisotropy term and the crossed crystalline/non-crystalline term respectively. The crossed term captures the different AMR experienced for current along different crystallographic directions. The  $\cos(2\theta)$  dependence is maintained with respect to the Néel vector orientation but the amplitude of this term depends on the current directions with respect to the crystal directions. The transverse AMR is given by

$$\frac{\Delta R_{yx}}{R_{av}} = C_I \sin(2\theta) + C_{I,C} \sin(4\psi - 2\theta) \quad (2.10)$$

which is independent of the purely crystalline terms. In uniaxial and biaxial CuMnAs films,  $C_U$  and  $C_C$  are relatively small while  $C_I$  and  $C_{I,C}$  are comparable to each other and make up the majority of the AMR in CuMnAs [45].

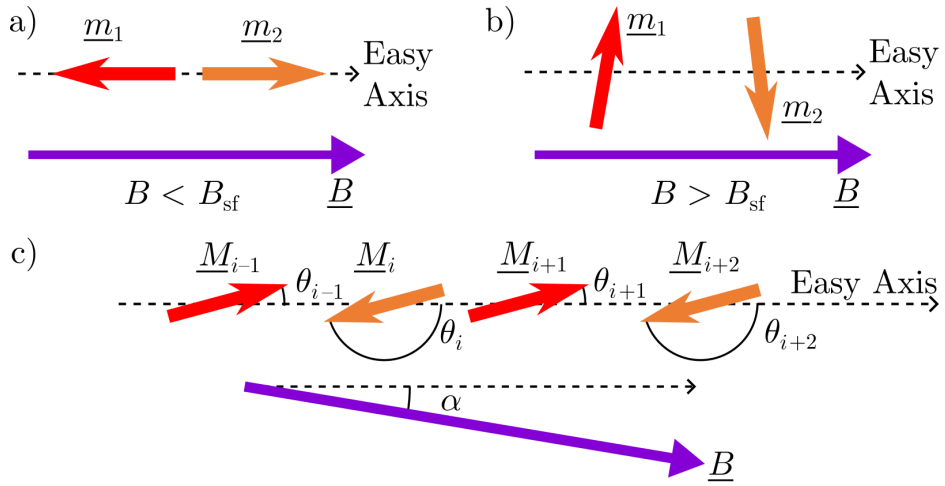


Figure 2.7: (a,b) Diagrams representing a pair of AFM moments in the (a) unflopped state and (b) flopped state. (c) Geometry of a 1D chain of AFM moments used to define the angles  $\theta$  and  $\alpha$ .

## 2.6 Spin Flop

The direct measurement of the terms from Eq. 2.8 in Ref. 45 was conducted using spin flop and field rotations. Due to the high exchange coupling field strength in CuMnAs, a realistically achievable magnetic field will never be strong enough to saturate the magnetisation, however if the field is applied along the easy axis of a uniaxial sample, a field of sufficient strength will cause spin flop to occur. Spin flop is the sudden transition from the configuration shown in Fig. 2.7(a) into the state illustrated in Fig. 2.7(b), in which the Néel vector has undergone a  $90^\circ$  reorientation away from the easy axis together with a slight canting of the magnetic moments towards the field. This occurs when the applied field strength,  $\mu_0 H$ , is larger than the spin flop threshold field strength,  $\mu_0 H_{sf}$ .

To understand why the flopped state is energetically favourable, it is necessary to express the energy of the state before and after spin flop. Figure 2.7(c) illustrates the geometry of a 1D chain sites  $i$ , occupied by magnetic moments  $\underline{m}_i$  each with angles to the easy axis of  $\theta_i$ , with a field applied at angle  $\alpha$  to the easy axis. The energy of this system is given by the following three terms

$$E_i = E_{i,\text{Zee}} + E_{i,\text{ex}} + E_{i,\text{ani}} \quad (2.11)$$

where  $E_{\text{Zee}}$  is the Zeeman term which describes the coupling of the moment to the external field,  $E_{\text{ex}}$  is the exchange term which captures the coupling of each moment to its neighbouring spins in the opposite sublattice and  $E_{\text{ani}}$  which is the anisotropy energy of each moment. For a uniaxial sample, these terms take the following forms

$$E_{i,\text{Zee}} = -m\mu_0 H \cos(\theta_i - \alpha) \quad (2.12)$$

$$E_{i,\text{ex}} = \frac{J_{\text{ex}} m^2}{2} \cos(\theta_i - \theta_j) \quad (2.13)$$

$$E_{i,\text{ani}} = -\frac{k_u}{2} \cos^2(\theta_i) \quad (2.14)$$

where the magnetic moment magnitude  $m = |\underline{m}_1| = |\underline{m}_2|$ ,  $k_u$  is the uniaxial anisotropy constant defined as the difference between the energy for a moment aligned along the easy axis and for when the moment is perpendicular to it.  $J_{\text{ex}} < 0$  is the exchange energy constant defined as the sum of the exchange energies between one moment and all of its antiparallel neighbours (taking the assumption that the sum of the exchange interactions can be considered the same for all elements). To find the spin flop transition, we must find the point at which the energy of the flopped state is equal to the unflopped state. To do this, we can first express the energy of each state as the sum of the energy in each sublattice. The total magnetisation can be used instead of considering each moment by assuming that the moments within each sublattice are all parallel such that  $\underline{M}_1 = \sum(\underline{m}_i) = -\underline{M}_2 = -\sum_j(\underline{m}_j)$  with each sublattice each making angles  $\theta_1$  and  $\theta_2$  to the easy axis, respectively. The magnitude of each magnetisation vector is then  $|\underline{M}_1| = |\underline{M}_2| = M_{1/2}$  such that the total energy of the system is given by summing the energy of each sublattice to give

$$\begin{aligned} E = & -M_{1/2}\mu_0 H [\cos(\theta_1 - \alpha) + \cos(\theta_2 - \alpha)] + \dots \\ & (M_{1/2})^2 J_{\text{ex}} \cos(\theta_1 - \theta_2) - \frac{k_u}{2} [\cos^2(\theta_1) + \cos^2(\theta_2)]. \end{aligned} \quad (2.15)$$

The energy for the unflopped state is found when  $\theta_1 = 0$  and  $\theta_2 = 180^\circ$  while in

the flopped state the energy is a function of the extent of canting and so must be determined by finding the angle which gives minimum energy for angles  $\theta = \theta_1 = -\theta_2$ . This is done by finding the solution to  $\partial E/\partial\theta = 0$  which gives the lowest energy. The energy of the unflopped state is given by

$$E_{\text{unflopped}} = -(M_{1/2})^2 J_{\text{ex}} - k_u. \quad (2.16)$$

and the energy of the flopped state can be written

$$E_{\text{flopped}} = -2M_{1/2}\mu_0 H \cos \theta - (M_{1/2})^2 J_{\text{ex}} \cos(2\theta) - k_u \cos^2(\theta) \quad (2.17)$$

$$E_{\text{flopped}} = -2M_{1/2}\mu_0 H \cos \theta - (M_{1/2})^2 J_{\text{ex}} [\cos^2(\theta) - 1] - k_u \cos^2(\theta) \quad (2.18)$$

such that  $\partial E/\partial\theta = 0$  can be written

$$\begin{aligned} \frac{\partial E_{\text{flopped}}}{\partial \theta} &= 2M_{1/2}\mu_0 H \sin(\theta) - \dots \\ (M_{1/2})^2 J_{\text{ex}} \sin(\theta) \cos(\theta) + 2k_u \sin(\theta) \cos(\theta) &= 0. \end{aligned} \quad (2.19)$$

The factor of  $\sin(\theta)$  can be separated and the corresponding solutions can be discarded as any these correspond to both moments lying parallel and along the easy axis, the energetic maximum. The other solution is given by

$$\cos \theta = \frac{M_{1/2}\mu_0 H}{2(M_{1/2})^2 [J_{\text{ex}} - k_u]} \approx \frac{\mu_0 H}{2\frac{M}{2} J_{\text{ex}}} \quad (2.20)$$

where the simplification is made by assuming that  $J_{\text{ex}} \gg k_u$  (in CuMnAs, the associated exchange coupling field is  $700 \pm 100$  T while the anisotropy fields are  $\approx 5$  mT [45]). When this is substituted back into Eq. 2.18, the energy is found to be

$$E_{\text{flopped}} = -\frac{(M_{1/2}\mu_0 H)^2}{M_{1/2} J_{\text{ex}}} + (M_{1/2})^2 2J_{\text{ex}} \left[ \left( \frac{\mu_0 H}{2M_{1/2} J_{\text{ex}}} \right)^2 - 1 \right] - k_u \left( \frac{\mu_0 H}{2M_{1/2} J_{\text{ex}}} \right)^2 \quad (2.21)$$

which expands to give

$$E_{\text{flopped}} = -\frac{(\mu_0 H)^2}{2J_{\text{ex}}} - J_{\text{ex}}(M_{1/2})^2 - \frac{k_u(\mu_0 H)^2}{4J_{\text{ex}}^2(M_{1/2})^2}. \quad (2.22)$$

By equating Eq. 2.16 and Eq. 2.22, the field strength at which both energies are equal, the spin flop field,  $\mu_0 H_{\text{sf}}$ , is found to be

$$-J_{\text{ex}}(M_{1/2})^2 - k_u = -\frac{(\mu_0 H_{\text{sf}})^2}{2J_{\text{ex}}} - J_{\text{ex}}(M_{1/2})^2 - \frac{k_u(\mu_0 H_{\text{sf}})^2}{4J_{\text{ex}}^2(M_{1/2})^2} \quad (2.23)$$

$$\Rightarrow (\mu_0 H_{\text{sf}})^2 = \frac{4J_{\text{ex}}^2 k_u (M_{1/2})^2}{2J_{\text{ex}}(M_{1/2})^2 - k_u}. \quad (2.24)$$

Since  $J_{\text{ex}} \gg k_u$ , the assumption that  $J_{\text{ex}} M_{1/2} \gg k_u / M_{1/2}$  can be made. The above expression then simplifies to

$$\mu_0 H_{\text{sf}} = \sqrt{2J_{\text{ex}} k_u}. \quad (2.25)$$

This result describes the spin flop field as a competition between the anisotropy energy and exchange energy. Above the spin flop field, the moments continue to cant into the applied field direction and the anisotropy energy and Zeeman energy terms both reduce. In CuMnAs, the spin flop field is  $\sim 2$  T, where the exchange field was measured to be  $B_{\text{ex}} = 700 \pm 200$  T suggesting an anisotropy field strength of  $B_u \sim 5$  mT [45].

## 2.7 Néel Order Spin Orbit Torque (NSOT)

The staggered current polarisation present in each sublattice of CuMnAs is a result of the ISGE and broken inversion symmetry present in CuMnAs as described in Section 2.2. To understand the principles of NSOT, consider the fact that the magnetisation in each sublattice is opposite:  $\underline{M}_1 = -\underline{M}_2$ . When the applied current,  $\underline{J}$ , becomes spin polarised, the spin transfer torque experienced by each sublattice is dependent on the inhomogeneous spin polarisation which is also opposite in each sublattice such that the resulting effective fields

are given by  $\underline{B}_1 \sim +\hat{z} \times \underline{J}$  and  $\underline{B}_2 \sim -\hat{z} \times \underline{J}$  as illustrated in Fig. 2.8(a). In this case, the resulting torques, given by  $\underline{T} \sim \underline{M} \times \underline{B}$ , are equal ( $T_1 = T_2$ ) and led to a coherent deflection in the moments through angle  $d\theta$ . This means that the maximum torque is generated when  $\underline{J} \parallel \underline{L}$  and there is no net effect on the moments when  $\underline{J} \perp \underline{L}$ . Without the necessary symmetry breaking, either no effective fields are generated (no symmetry breaking) or the effective fields on each sublattice are the same and generate no net torque.

If the deflection angle is large enough in a biaxial sample, the current induced NSOT can reorient moments to lie along the other easy axis while in both uniaxial and biaxial samples, current induced NSOT can generate, destroy or move domain walls and domain wall features [57], induce 180° reorientation of the moments or cause shattering of the domain structure [31]. The current amplitude dependence of each of these effects leads to the threshold currents observed in each of these cases, and is why currents below the threshold do not induce observable switching signals or changes persisting long enough to be detected as AMR measurements after the pulses. Therefore, measuring the NSOT induced AMR changes concurrent with the applied current is necessary to observe NSOT below the threshold as performed by Godinho et al. [46] and in the studies contained in Chapter 7.

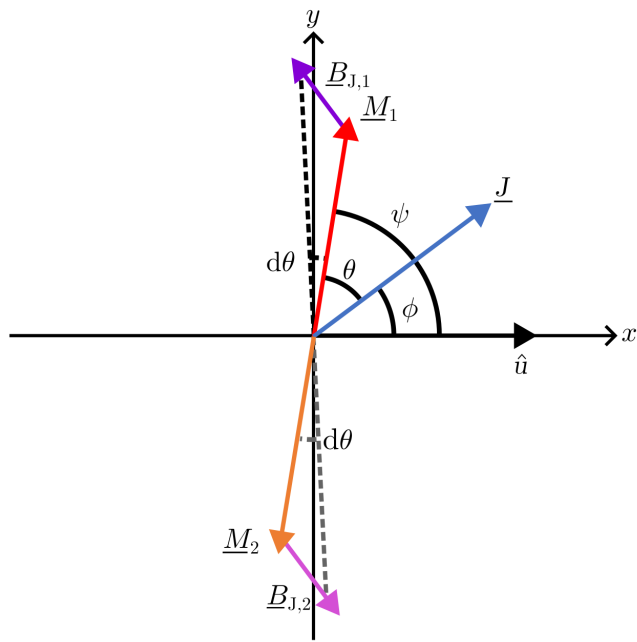


Figure 2.8: Geometry of the effective fields,  $\underline{B}_{1,2}$  on each sublattice  $\underline{M}_{1,2}$  as a result of spin orbit torque generated by an applied current  $\underline{J}$  for an AFM with necessary symmetry for the generation of staggered spin polarisation leading to NSOT.

# Chapter 3

# Probing the Manipulation of Antiferromagnetic Order in CuMnAs Films Using Neutron Diffraction

## 3.1 Introduction

Neutron diffraction is a well-established technique to directly measure the atomic arrangement of magnetic moments in a bulk AF crystal. It provides a quantitative determination of the Néel vector and, unlike electron microscopy techniques, is routinely performed in high magnetic fields. It is, therefore, well-suited to study spin-flop transitions, which typically occur in magnetic fields of several Tesla.

In this chapter, neutron diffraction is performed on CuMnAs samples to determine the full thickness extents of spin flop in an antiferromagnet, the results of which are reported in Ref. 58. Before undertaking the following studies, there was no conclusive evidence to support the idea that spin flop occurs throughout the thickness of such a film. In the study of the spin flop transition in CuMnAs by Wang et al [45], two techniques are used: electronic transport

measurements and x-ray magnetic linear dichroism (XMLD) absorption measurements. Both techniques have limitations which culminate in the desire for a more explicit measure of the magnetic ordering in an antiferromagnetic material undergoing spin flop. In the transport measurements, the AMR value (see Section 2.5) has no reference values because it is specifically the relative change in magnetoresistance, normalised by linear resistance. This measure gives little insight into the extent of spin flop, however it is a convenient technique for determining the anisotropy and spin flop field of an antiferromagnet. In the XMLD absorption measurement, the technique gives a quantitative measure of the proportion of moments parallel and perpendicular to a certain axis as a function of applied magnetic field, but the technique does not detect behaviour below the surface. In the following, neutron diffraction is demonstrated to be capable of unambiguous total volume determination of the spin-flop rotation in CuMnAs films with thickness down to 20 nm and transport measurements are also conducted to corroborate the findings. As further incentive to use neutron diffraction as part of the antiferromagnetic characterisation toolbox, a measure of uniaxiality and the extents of spin flop are also extracted from the neutron diffraction results. In order to understand the experiments, this chapter begins by introducing the basics of diffraction in general before explaining the advantages of neutron diffraction in antiferromagnetic spintronics research.

### 3.1.1 Neutron Diffraction

Diffraction crystallography utilises the constructive interference of waves scattered off of atoms which form planes in a periodic crystal structure. It relies on satisfying Bragg's law which states that constructive interference will occur for a wave with wavelength  $\lambda$  incident on the structure at angle  $\theta$  to the considered plane such that the spacing between planes,  $d$ , is equal to the path length difference introduced by the number of crystal spacings between two planes,  $n$ ,

such that

$$n\lambda = 2ds\sin(\theta). \quad (3.1)$$

The simplest form of diffraction is X-ray diffraction (XRD) crystallography, which is often monochromatic (of a single wavelength). In XRD the photons, which travel at the speed of light, naturally, are scattered by the electronic structure of atoms. When the incident light is monochromatic, only one incident angle and wavelength combination is measurable at a time, meaning that the incident angle must be changed in order to determine the lattice spacings. Often a monochromatic XRD system will have control over the relevant angles by having 2 or 3 axis control of the sample rotation and control over the incident beam and detected scattering angles.

Neutrons, by contrast, have an inherent magnetic moment while being electrically neutral. They instead interact with atomic nuclei and associated magnetic fields when scattering. Neutrons do not travel at the speed of light and instead the speed of the neutron depends on energy according to the de Broglie equation

$$\lambda = \frac{h}{mv} \quad (3.2)$$

where  $h$  is Planck's constant,  $E$ ,  $m$  and  $v$  are the energy, mass and speed of a neutron, respectively. The de Broglie equation allows the wavelength of a neutron to be determined from the speed (measured by the time-of-flight) of that neutron. This allows for the use of a broadband (consisting of a wide distribution of wavelengths) neutron beam in neutron diffraction so long as the neutrons are generated as pulses with a known reference time for the start of the trajectory. By inspecting Eqn. 3.1, it can be seen that, for one incident angle, a broadband neutron source will satisfy the condition for multiple planes because the condition is satisfied by multiple wavelengths concurrently. This

means that a broadband neutron beam incident on a sample will generate a diffraction pattern which reveals multiple diffraction peaks from one geometry simultaneously.

Neutrons have an inherent magnetic moment which means that they interact with the magnetic fields present within the unit cells of magnetic materials; this allows neutron diffraction to probe the magnetic structure of materials. In the case of CuMnAs, the (100) and (010) in-plane (IP) peaks are structurally forbidden and therefore undetectable in XRD. In neutron diffraction, however, these two peaks can be detected so long as the local magnetic moments align perpendicular to the scattering vector (such that the moments lie parallel to [010] and [100] respectively). Peaks of this nature are said to be purely magnetic diffraction peaks. There can also be combined structural-magnetic peaks in which the scattering cross-section depends on the magnetic structure but is still detectable in the absence of magnetism. In CuMnAs, the (001) is a combined structural-magnetic peak and its scattering cross-section is increased whenever moments lie in the plane perpendicular to the [001] crystallographic direction.

The neutron diffraction process used in the following study is a cold neutron, time of flight technique in which a pulse of protons from a synchrotron is fired at a tungsten target to induce spallation of neutrons. These neutrons are emitted as high energy, broadband neutron pulses. The neutrons are thermalised through a methane moderator to reduce the energy such that the wavelengths are comparable to inter-atomic distances. By including the time-of-flight information with the spatial information, the d-spacing can be extracted from the impact counts on the split detector which surrounds the sample between 10° and 170° on either side of the sample. This detector also has some small range outside the horizontal plane but most of the resolution is in the horizontal plane [59, 60].

## 3.2 Methods

The two processes used to measure spin flop in, firstly neutron diffraction, and secondly in transport measurements, are described below. The neutron diffraction measurements utilised the time-of-flight cold neutron beam line WISH at the ISIS facility and the transport measurements were conducted in cryostats with superconducting solenoid magnets at the School of Physics and Astronomy, University of Nottingham.

### 3.2.1 Neutron Diffraction at WISH

In CuMnAs, the crystal symmetries allow for interaction, and therefore scattering, of the IP, (100) or (010), planes when the magnetic moments are lying perpendicular to each of these directions. The (001) plane yields a combined structural-magnetic peak and exists regardless of magnetic structure, however its scattering cross-section does depend on the extent of magnetism in the plane perpendicular to the [001] axis, where the magnetism acts to increase the scattering cross-section through increased interaction strength. Figures 3.1(a) and 3.1(b) illustrate the geometry of the experiment for when the magnetic field is applied along the [010] easy axis. The diagram shows the directions of the incoming beam, applied field and magnetic ordering of a uniaxial sample before (a) and after (b) the spin flop transition. In this geometry, the (h0l) scattering plane is experimentally accessible and both the (100) and (001) diffraction peaks can be detected. While the applied field magnitude,  $H$ , is below the spin flop threshold,  $H_{sf}$ , the majority of magnetic moments lie perpendicular to this scattering plane and the (100) peak is accessible, and the (010) peak is correspondingly forbidden. Above this threshold, the moments rotate through  $90^\circ$  in the sample plane and lie parallel to the (h0l) scattering plane and therefore the (010) peak becomes accessible as the (100) peak becomes forbidden. In the illustrated geometry, the (100) peak can be detected but the (010) peak cannot. By rotating the sample to apply the

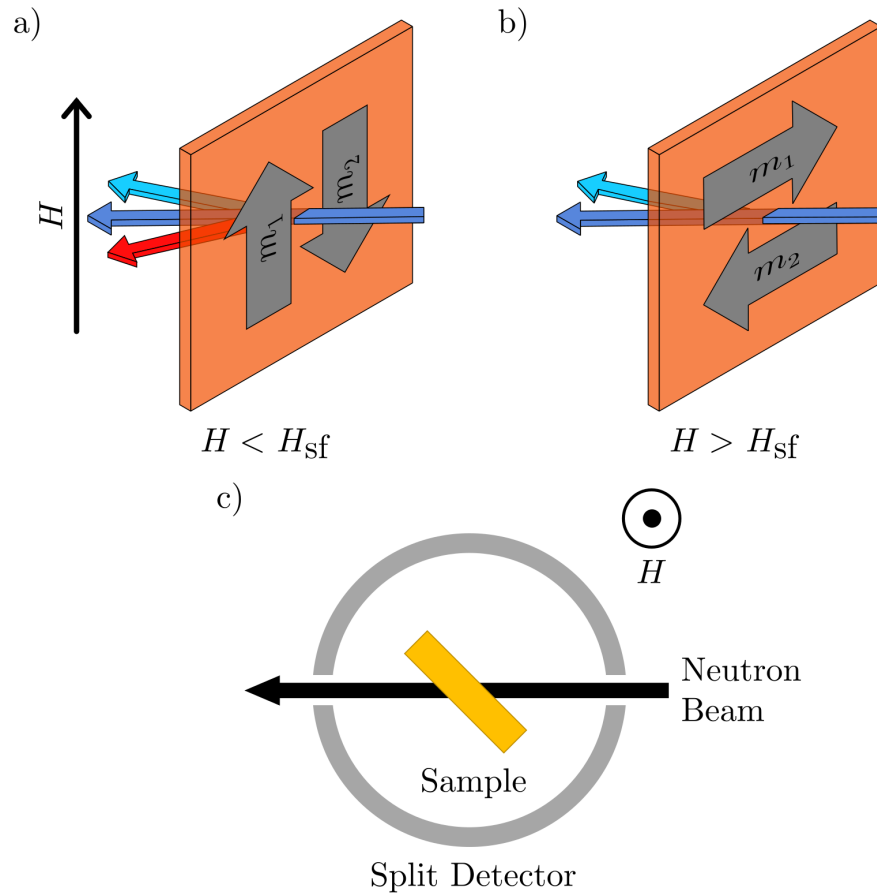


Figure 3.1: (a,b) Diagrams demonstrating the geometry for neutron diffraction for a magnetic field,  $H$ , applied along the [010] easy axis with strength below, (a), and above, (b), the spin flop field,  $H_{sf}$ . The grey arrows marked  $m_1$  and  $m_2$  represent the two sublattice magnetic alignments. The thin black arrow represents the vertical applied field direction and the blue arrows represent the incident neutron beam. The cyan arrow represents the (001) diffraction peak which is present in both states while the red arrow represents the IP peak which is forbidden in the arrangement shown in (b), above the spin flop field. (c) Schematic diagram of the neutron diffraction experiment showing the horizontal scattering plane and the vertical magnetic field. The incident beam is represented by the black arrow, and the detector arrays covering IP scattering angles from  $10^\circ$  to  $170^\circ$  are depicted as gray semicircles.

field along the [100] direction, the (010) peak can then be detected and the (100) cannot. By measuring the change in amplitude of this (100) or (010) IP peak as a function of applied field strength, the extents of spin flop can be measured as the relative change in magnitude of these peaks. For both applied field directions, the (001) peak is detectable because the moments lie in the sample plane, perpendicular to the (001) scattering plane, and so the (001) peak can be used in normalisation and to detect anomalies.

In the ideal, single domain (uniaxial) system, the IP peak would go from maximum amplitude corresponding to 100 % of the moments lying parallel to the easy axis, to zero amplitude corresponding to 100 % of the moments lying perpendicular to the easy axis. The dependence of the contribution, ( $C$ ), of a moment at angle  $\theta$  follows a dependence of  $C \propto \sin^2(\theta)$  since it corresponds to the component of the magnetic moment's vector lying parallel to the easy axis. In a real system, the domain walls and any pinned sites will exhibit some remnant signal with moments lying at some arbitrary angle, contributing to the peak's amplitude. A biaxial sample, however, will exhibit a peak of approximately half the maximum amplitude at zero-field and exhibit only a remnant signal at high field. It is therefore important to measure the sample along two perpendicular directions, allowing the total magnitude of the signal to be determined based on the magnitudes at zero field in each direction.

The neutron diffraction process relies on the scattering cross-section of the film. Because the films are very thin, maximising surface area is important to increase the volume illuminated by the neutron beam. In these studies, two large pieces ( $\approx 25$  mm squares) of both Sample B (20 nm CuMnAs on GaP(001)) and two large pieces ( $\approx 20$  mm squares) of Sample C (45 nm CuMnAs on GaP(001)) were used. Both layers exhibit uniaxial magnetic ordering along the CuMnAs[010] axis. The samples are attached to the end of a probe using aluminium foil before being inserted into the cryostat.

Figure 3.1(c) represents the geometry of the experiment with a horizontal scattering plane and a vertical magnetic field generated by a superconducting

split-pair solenoid magnet. For both films, the samples were mounted in two orientations: in one case, the uniaxial easy axis ([010]) was parallel to the applied magnetic field, and in the other, the field was parallel to the [100] axis. These geometries allowed access to the (h0l) and (0kl) scattering planes, respectively. The position of the samples in respect of the incident beam was chosen to optimize the neutron flux for the (100) and (010) magnetic reflections as well as to access the (001) reflection at the same time. This was achieved when the surface plane of the samples was at 45° to the beam direction. The measurements were conducted at a sample temperature 100 K, and care was taken to position the samples consistently.

The neutron beam consists of pulses of broadband neutron radiation, which, when incident on the sample, scatter according to Bragg's law. The position and time of incidence on the detector is recorded. In these studies, the collection period is in the order of hours, ranging from 1 hr to 8 hrs depending on the sample and orientation, being shorter for the thicker layer (Sample C) and shorter when applying the field along the easy axis because the count rate is higher at zero field in this configuration.

Three raw IP diffraction peaks are included in Fig. 3.2 as an aid for understanding the processing. These data are from the measurement of Sample C, the 45 nm film, with the field applied along the [010] easy axis while measuring the (100) IP peak. The three peaks were collected at the labelled field strength, and show that the amplitude of the peak decreases with increasing field strength, being almost entirely extinguished at 8 T (cyan crosses), but do not otherwise change in shape or position. The peak amplitudes are calculated from these peaks by integrating the peak region and subtracting the integrated background region. Similar regions are chosen for the OOP peaks and the background subtraction is also conducted on those to find their amplitudes. The IP peak amplitudes are divided by the OOP peak amplitudes as a form of normalisation, allowing for comparison between measurements with different total yields.

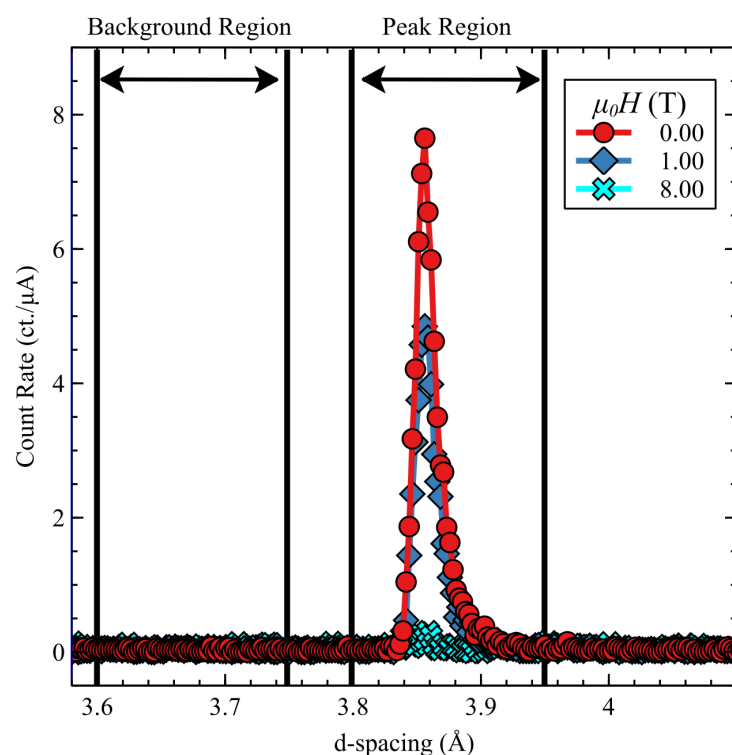


Figure 3.2: Plots of the (100) peak for Sample C (45 nm film) with three different field strengths applied along the easy axis. The integration regions used in peak amplitude calculation and background subtraction are shown.

### 3.2.2 Transport Measurements in a Cryostat

Pieces of Samples B and C were patterned into L-shaped Hall bar devices (L-bars) as illustrated in Fig. 3.3(a). Current was passed along the length of the L-bar and the two arms allow for simultaneous measurement of the transverse ( $V_{xy}$  and  $V_{yx}$ ) and linear voltages ( $V_{xx}$  and  $V_{yy}$ ) along two crystallographic directions. In the illustrated geometry, the AMR signal manifests only as changes in the transverse voltages but both AMR values were determined using the following expressions:

$$AMR_{\perp} = \frac{2(V_{yx} - V_{xy})}{V_{xx} + V_{yy}} \quad (3.3)$$

$$AMR_{\parallel} = \frac{V_{xx} - V_{yy}}{V_{xx} + V_{yy}} \quad (3.4)$$

where the factor of two in Eq. 3.3 accounts for the number of squares between the longitudinal voltage contacts. A piece of Sample C was also patterned with the L-bar rotated through  $45^{\circ}$  as illustrated in Fig.3.3(b) such that the signal should appear entirely in the  $V_{xx}$  portion of the signal.

The devices were mounted on the end of a probe and inserted into the bore of a cryostatic superconducting magnet with the field applied in the plane of the sample, along the CuMnAs[010] easy axis as illustrated. At zero field, the sample's magnetic moments predominantly lay parallel to the field and at high field they lay predominantly perpendicular to this direction. The current was applied continuously and the field was swept up to the maximum field before being swept back to zero. This sweep was repeated with the field in the antiparallel direction. The four voltage values are measured as concurrently as possible at a constant rate while the field was swept. The AMR values were plotted as a function of field. If necessary, the sweeps were smoothed to reduce the scatter from electrical noise.

For Sample C, the L-bar used had a width of 100  $\mu\text{m}$  and the field sweep was repeated with the field applied along the CuMnAs[100] hard axis direction

to demonstrate uniaxial behaviour with applied current  $I_{\text{probe}} = 2 \text{ mA}$  (current density of  $\approx 4 \times 10^4 \Omega\text{cm}^{-2}$ ). For Sample B, the L-bars were  $10 \mu\text{m}$  wide and a current of  $I_{\text{probe}} = 1 \text{ mA}$  (current density of  $5 \times 10^5 \Omega\text{cm}^{-2}$ ) was applied. The Sample B device in Orientation B was used to check for uniaxiality by applying the field along three directions: the [100], [110] and [110] directions. The device in Orientation A only had the field swept along the CuMnAs[010] easy axis but was swept in both directions to measure hysteresis.

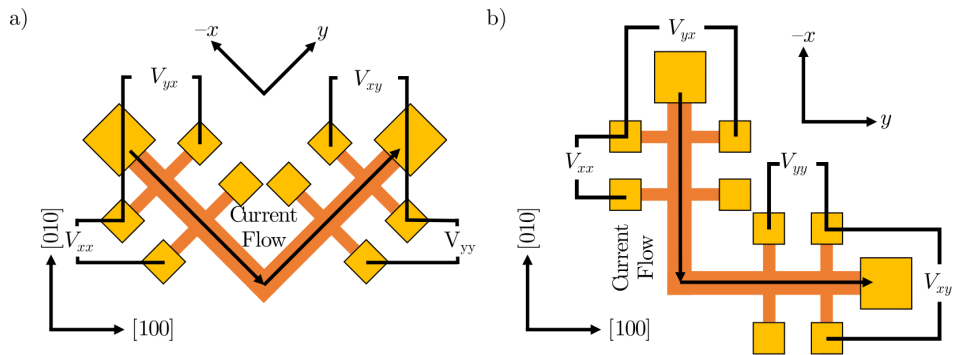


Figure 3.3: Schematic of L-bar device patterns with the arms drawn (a) in Orientation A, with the arms along the  $[110]$  and  $[1\bar{1}0]$  crystal directions and (b) in orientation B, with the arms along the  $[100]$  and  $[010]$  crystal directions. Samples in Orientation A will manifest voltage changes in the  $\text{AMR}_\perp$  value where Orientation B will manifest the signal in the  $\text{AMR}_\parallel$  direction. The orange represents the  $100 \mu\text{m}$  or  $10 \mu\text{m}$  wide CuMnAs bar for the 45 and 20 nm samples, respectively, and the gold squares represent contact pads to which wires are bonded. The arrows represent the current flow in the device, and the voltages drawn correspond to the voltages described in the text where 1 and 2 correspond to the first and second arm the current flows through, respectively.

### 3.3 Results

The following section demonstrates the results from the above described experiments. First, each step in the neutron diffraction normalisation process are shown: each of the IP and OOP peaks are displayed; their amplitudes are calculated and plotted separately; the normalised amplitude results are shown and the uniaxial nature is confirmed. Second, the plots of AMR measurements for both samples and corresponding analysis are given. Finally, the extents of spin flop is calculated from a neutron diffraction result and compared to an AMR measurement for the same sample and geometry.

#### 3.3.1 Neutron Diffraction

The detector for the neutron diffraction technique collects information for the time and position of each neutron detected (each count). The combination of time and position information allows proprietary software to determine the d-spacing associated to each count after the user selects a spatial region of interest. The resulting plots of d-spacing against counts can be inspected to find peaks at a d-spacing corresponding to the unit cell parameters for the diffraction peak, in our case, 3.82 Å for IP peaks and 6.32 Å for the OOP peaks [47]. Figures 3.4 and 3.5 contain the raw peaks measured in neutron diffraction for the two described sample orientations using the 45 nm and 20 nm samples, respectively, each showing both the IP and OOP peaks. In all cases, the IP peaks show a decreasing amplitude with increasing field while the OOP peaks remain seemingly unchanged.

The peaks were integrated to determine the peak amplitudes. These amplitudes are plotted in Fig. 3.6 with the uncertainties calculated automatically by the proprietary software. The plots further confirm that the IP peaks show a decreasing amplitude with increasing field while the OOP peaks remain mostly unchanged, only varying slightly and not systematically with increasing field.

The normalisation of the peak amplitudes is performed by dividing the IP

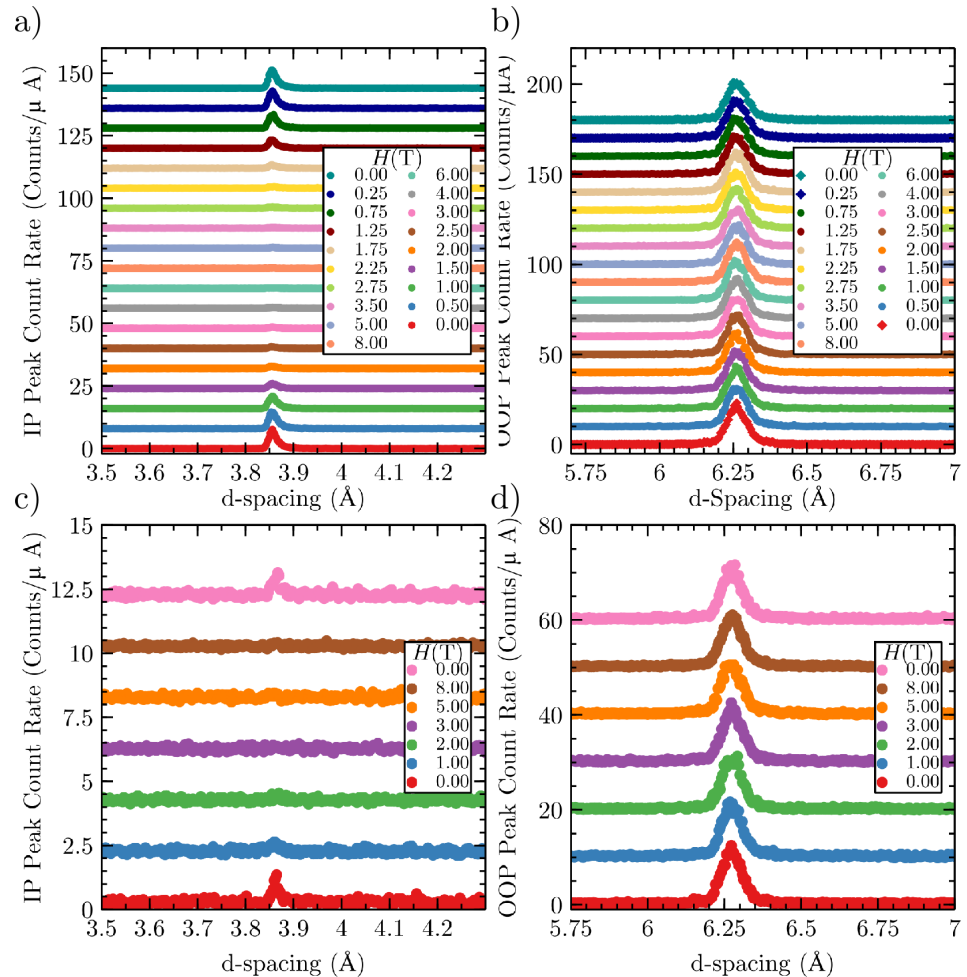


Figure 3.4: Neutron diffraction measurements for Sample C, the 45 nm CuMnAs layer on GaP, of: (a) (100) peaks and (b) (001) peaks for magnetic field along the [010] easy axis direction; (c) (010) peaks and (d) (001) peaks for magnetic field along the [100] hard axis direction.

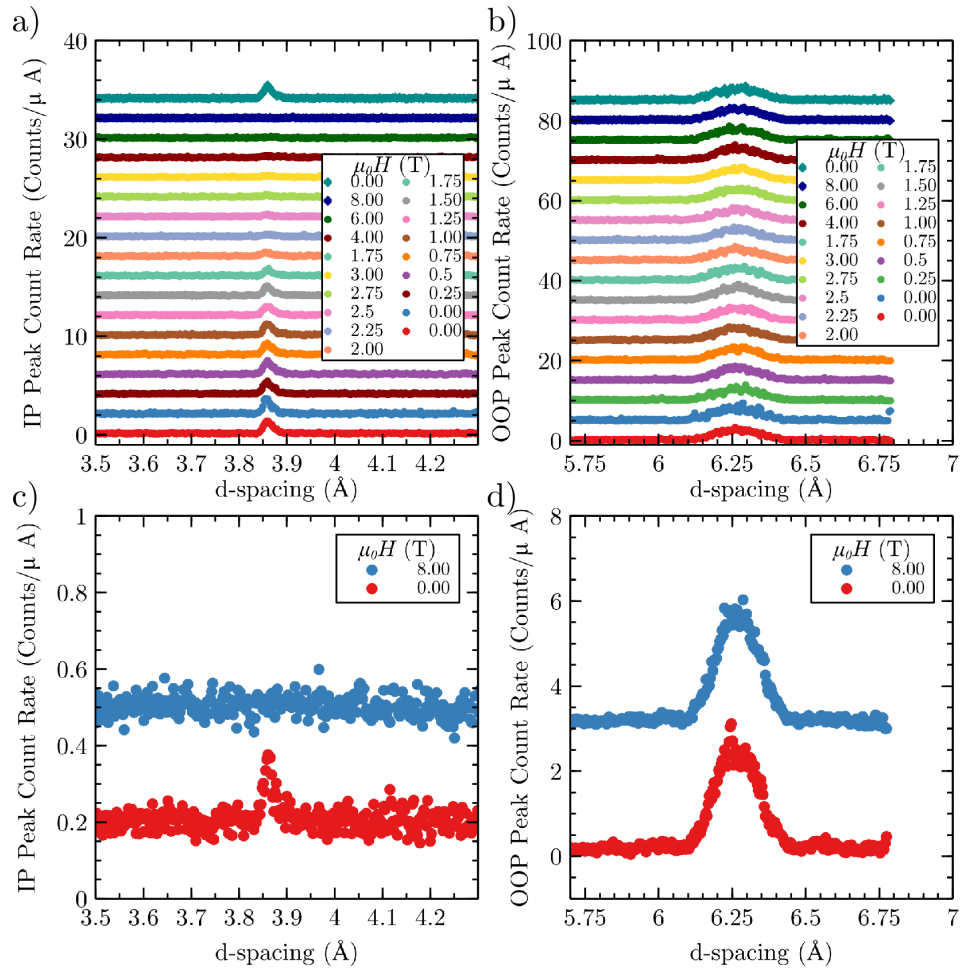


Figure 3.5: Neutron diffraction measurements for Sample B, the 20 nm CuMnAs layer on GaP, of: (a) (100) peaks and (b) (001) peaks for magnetic field along the [010] easy axis direction; (c) (010) peaks and (d) (001) peaks for magnetic field along the [100] hard axis direction.

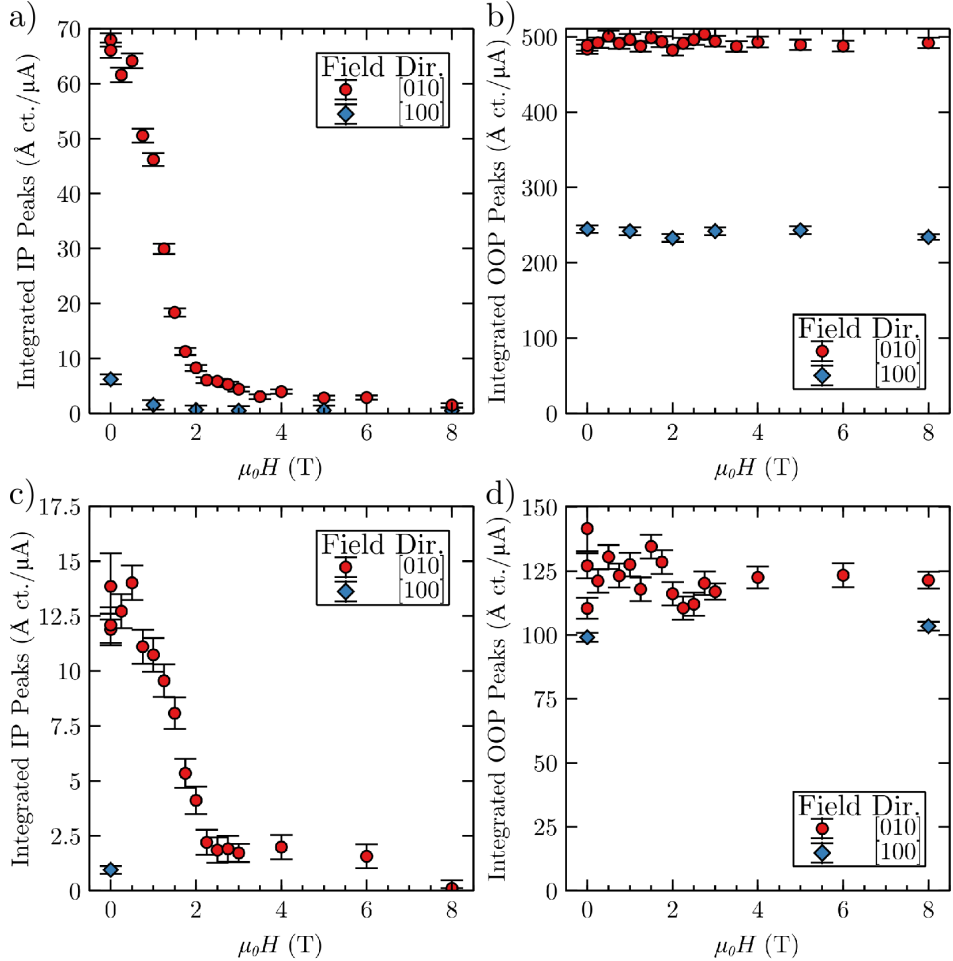


Figure 3.6: Neutron diffraction peak amplitudes for the 45nm thick film (a,b) and 20nm thick film (c,d) calculated from the data in Figs. 3.4 and 3.5. The left column (a,c) correspond to the purely magnetic IP peaks and the right column correspond to the structural-magnetic OOP peaks. The red dots correspond to measurements with the magnetic field applied along the [010] easy axis and the blue diamonds correspond to the measurements with the magnetic field applied along the [100] hard axis.

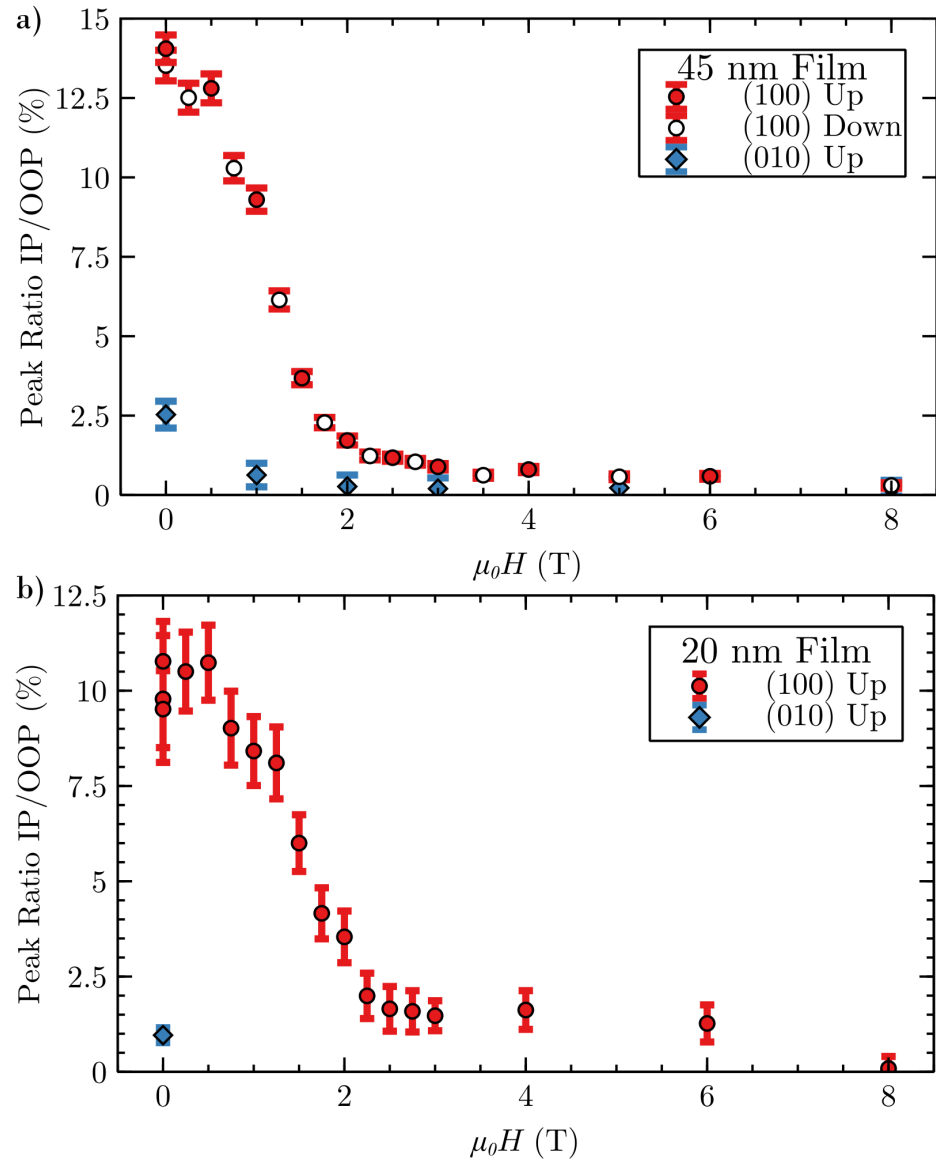


Figure 3.7: Neutron diffraction peak ratios as a function of field for (a) Sample C, 45 nm CuMnAs on GaP, and (b) Sample B, 20 nm CuMnAs of GaP calculated by dividing the IP peak amplitudes by the OOP peak amplitudes from the data shown in Fig. 3.6. The red circles/blue diamonds represent the experiments with the field applied along the [010]/[100] sample directions, measuring the (100)/(010) diffraction peaks respectively. Open and filled symbols represent the decreasing and increasing field directions respectively.

peak amplitudes by the corresponding OOP peak amplitudes to create a peak ratio. Plots of the ratios of integrated peak amplitudes vs magnetic field for Samples C and B, (45 and 20 nm thick CuMnAs layers respectively) are shown in Fig. 3.7. For the 45 nm sample [Fig. 3.7(a)], the (100) peak is larger than the (010) peak by a factor of  $5.4 \pm 0.9$ . This indicates that the magnetic moments in the sample are predominantly aligned with the [010] axis. A sharp decrease in intensity is observed between zero and 1 T for the (010) peak, and between zero and 2 T for the (100) peak, due to the spin flop rotation of the Néel vector into an axis which is perpendicular to the field. In high fields, the (100) peak is decreased to  $2.2 \% \pm 0.7 \%$  of its zero-field amplitude, showing conclusively that the vast majority of the CuMnAs layer undergoes spin flop in this field range. After the high field measurements, the sample recovers its original state.

The 20 nm CuMnAs layer [Fig. 3.7(a)] exhibited a (100) to (010) peak amplitude ratio of  $10.5 \pm 3.4$  and, therefore, demonstrates more dominant uniaxial anisotropy than the thicker layer. As with the thicker layer, the (100) peak intensity drops sharply between 1 and 2 T applied fields. However, there is significant intensity remaining between 2 and 6 T, which may be attributed to the presence of  $180^\circ$  magnetic domain walls and defect-driven domain pinning [53, 54]. The intensity then drops to zero between 6 and 8 T. Due to time constraints and the weak signal from this thin film, the (010) peak was not measured over the whole magnetic field range.

### 3.3.2 Transport Measurements

Magnetic fields sweeps were conducted on Samples B and C, 20 nm and 45 nm CuMnAs films on GaP respectively. They were conducted in different cryostats and at different temperatures, however both used the same general procedure.

Figure 3.8 contains results for the 45 nm samples with the transverse (a) and longitudinal (b) changes in AMR plotted as a function of the applied field strength. The field was applied along the [010](red) and [100](blue) directions.

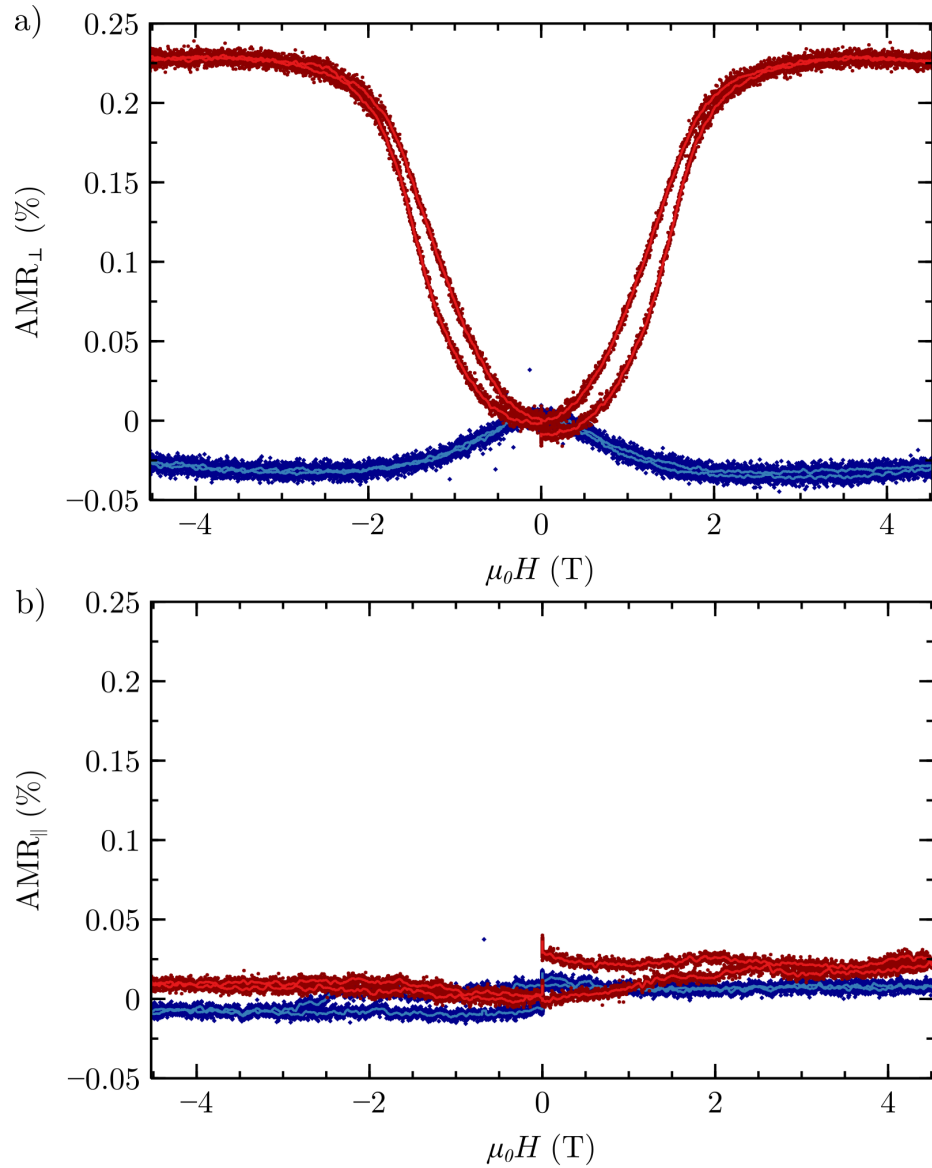


Figure 3.8: (a) Transverse AMR and (b) longitudinal AMR, as defined in Eqs. 3.3 and 3.4, respectively, vs the magnetic field for an L-bar device fabricated from Sample C (45 nm CuMnAs on GaP) in Orientation A. The red and blue lines are for fields along the [010] and [100] axes, respectively. The darker lines of each colour are smoothed versions of the lighter colours, using a 5-wide moving average filter. The plots are offset to show zero AMR at zero field for clarity.

The maximum magnetic field in each direction was 4.5 T with the sample at 4 K. As expected, the broadened spin flop curve appears exclusively in the transverse AMR measurement in this geometry. The region of maximum gradient is centered around  $\approx 1.5$  T with the majority of the transition occurring between 1 and 2 T. When the field is applied along the easy axis, the AMR signal is relatively large at a maximum 0.23 %. When the field is applied along the hard axis the maximum AMR signal is -0.03 %. The easy axis signal is approximately 7 times larger than the other, which is similar to the value in neutron diffraction ( $5.4 \pm 0.9$ ). The sweeps are very symmetric with only small hysteresis, showing a difference of  $\approx 0.2$  T between points of maximum gradient in opposing field sweep directions.

In order to corroborate the uniaxial nature of Sample B, transport measurements were conducted with the field applied along three directions using an L-bar patterned as illustrated in Fig.3.3(b). Figure 3.9 contains the results for fields applied up to 4 T along the [010] (red circles), [110] (cyan squares) and [100] (blue diamonds) directions. The sample was kept at 4 K in these measurements. Because of the change in L-bar orientation, the AMR signal manifests solely in the parallel AMR measurement. The signal-to-noise for the [100] measurement is worse because of poor optimisation in the control software. Despite this, results show that the AMR spin flop signal is maximum along the [010] direction and is minimum for the measurement applied along the [100] direction. The maximum AMR signal for the [110] direction is approximately half of the maximum for the [010] direction. These results confirm that the sample is uniaxial with the easy axis along the [010] direction, agreeing with the neutron diffraction results.

Figure 3.10 contains plots of the transverse (a) and longitudinal (b), AMR values as a function of applied field along the [010] axis of Sample B (20 nm CuMnAs on GaP) with the L-bar aligned as illustrated in Fig. 3.3(a) for decreasing/increasing magnetic field strength shown in red/blue respectively. The maximum magnetic field in each direction was 4 T except when sweeping

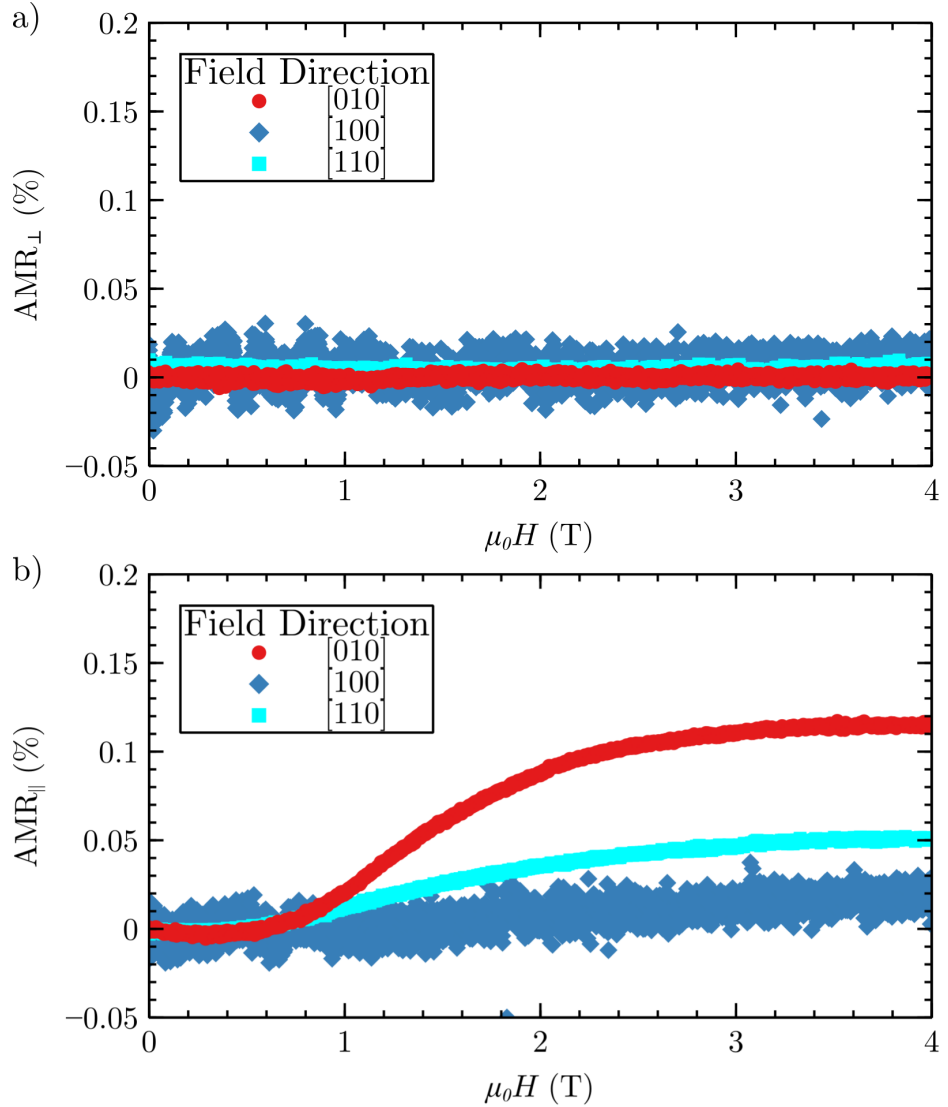


Figure 3.9: (a) Transverse AMR and (b) longitudinal AMR, as defined in Eqs. 3.3 and 3.4, respectively, vs the magnetic field for an L-bar device fabricated from Sample B (20 nm CuMnAs on GaP) in Orientation B. The data for the field applied along the [100], [110] and [010] directions are in red, cyan and blue respectively. The plots are offset to show zero AMR at zero field for clarity.

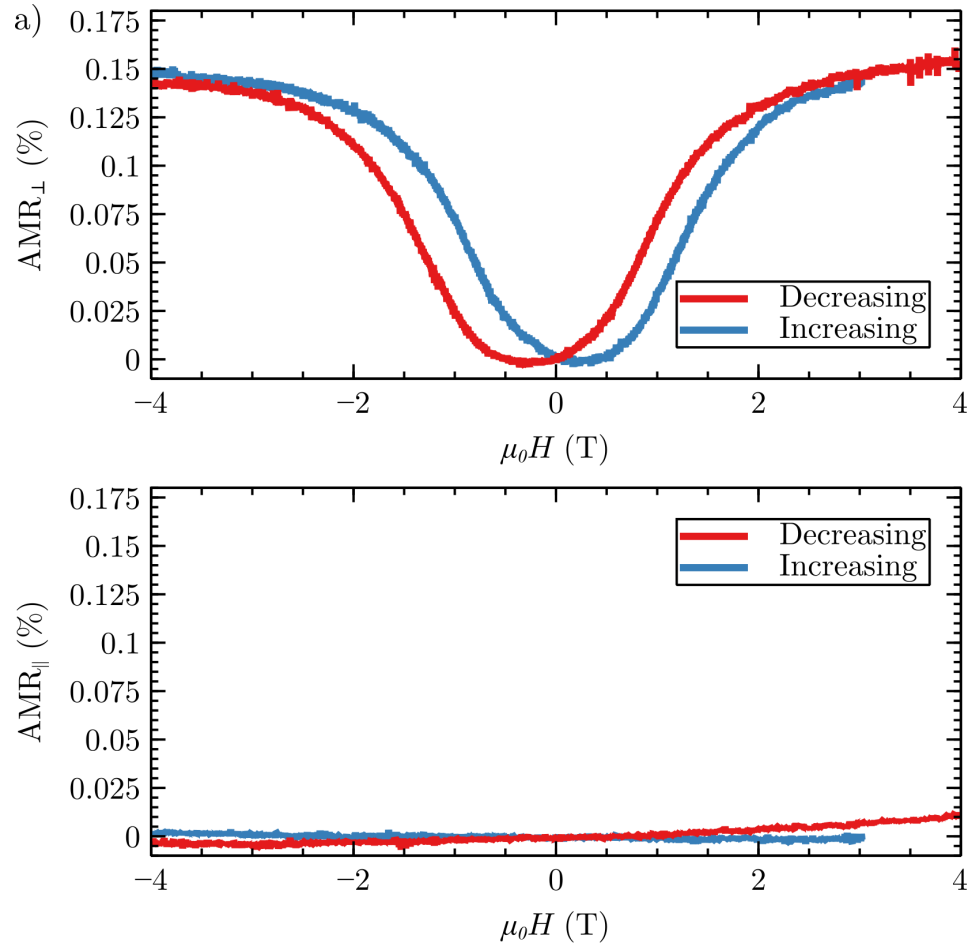


Figure 3.10: (a) Transverse AMR and (b) longitudinal AMR, as defined in Eqs. 3.3 and 3.4, respectively, vs the magnetic field for an L-bar device fabricated from Sample B (20 nm CuMnAs on GaP) in Orientation A. All lines are for fields along the [010] easy axis, with red and blue lines for decreasing and increasing field respectively. The plots are offset to show zero AMR at zero field for clarity.

back up (blue line) where the measurement was aborted early at 3 T. In these measurements the sample was kept at 2.5 K. The spin flop signal appears exclusively in the transverse AMR measurement with only a linear temperature drift appearing in the longitudinal AMR measurements. The majority of the spin flop transition occurs between 1 and 2 T as with the thicker sample. These data show significantly more hysteresis than in the thicker layer, with a gap of  $\approx 0.5$  T between points of maximum amplitude in opposing directions and the signal is smaller, at 0.15 % AMR. There was a long pause at each end of the sweep, leading to some drift in the measurements, so the increasing and decreasing sweeps are plotted separately for this sample.

### 3.3.3 Comparing Neutron Diffraction to Transport

Figure 3.11 compares the neutron diffraction and  $\text{AMR}_\perp$  measurements over the same magnetic field range using the data in red from Figs.3.7(a) and 3.8(a), respectively. The spin flop extent is calculated from the neutron diffraction results and is defined as  $1 - P(H)/P(0)$ , where  $P(H)$  is the integrated peak amplitude at field  $H$  and  $P(0)$  is the initial value at zero field. It can be seen that the electrical transport measurement gives a qualitatively accurate measure of the spin flop extent with the shape, hysteresis, and spin flop field all matching well. Note that the neutron diffraction measurements were performed at 100 K while the AMR was measured at 4 K. Previous studies have shown that this difference in temperature creates a small change in amplitude of the AMR signal due to changes in the base resistance but does not qualitatively change the signal [45, 61].

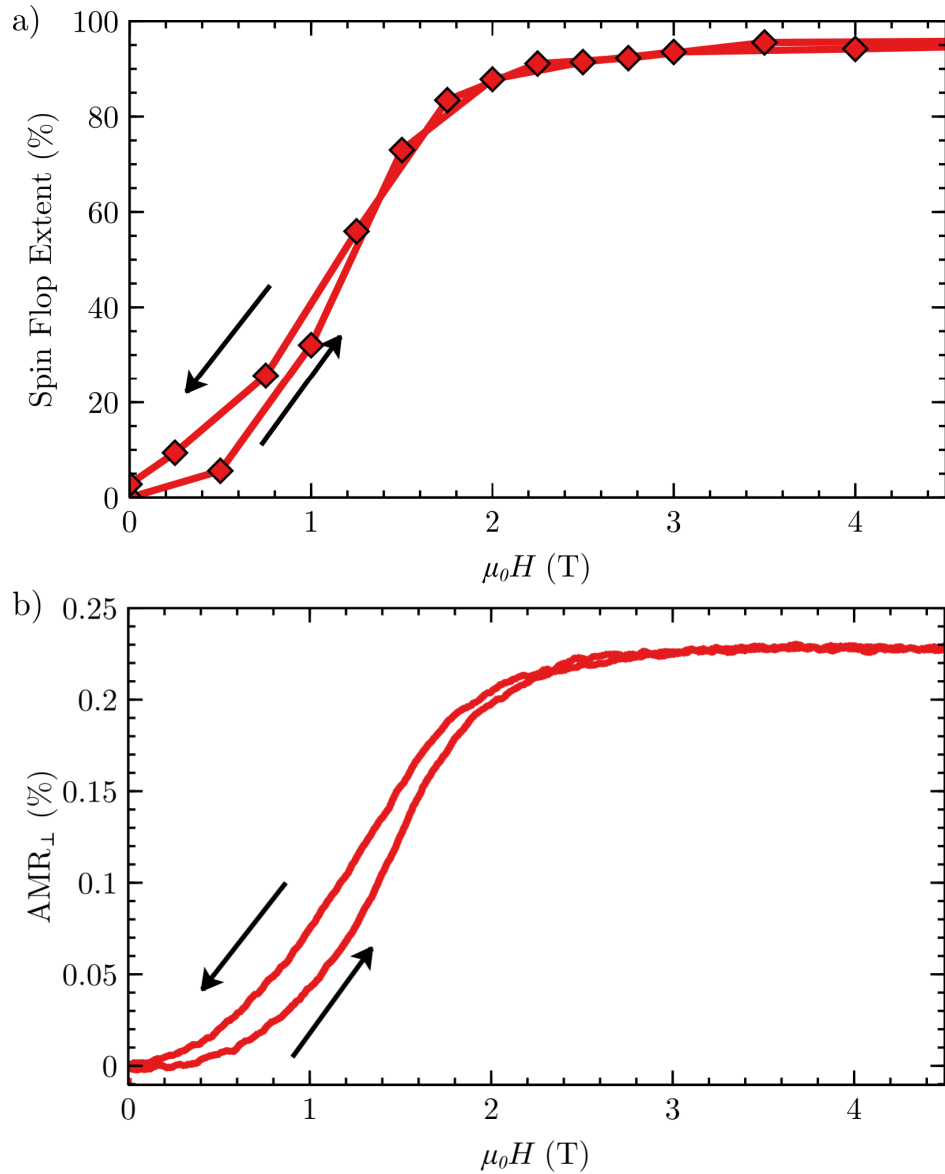


Figure 3.11: Comparison of spin flop behaviour for (a) spin flop extents calculated from neutron diffraction measurements and (b) transverse AMR measurements for Sample B with the magnetic field applied along the [010] easy axis. The neutron data is truncated to 4.5 T for ease of comparison. Arrows indicate the the direction of field sweep.

### 3.4 Discussion and Conclusions

Given that only 2.2 % of the moments remain for one measurement, the spin flop extent can be said to have reached 98 % reorientation in moments at 8 T, for the first time clearly showing that spin flop must occur throughout the material's thickness, not just at the free surface. In all the 8 T measurements there is some small remnant signal. The canting angle for a CuMnAs film was observed to be 0.2° at 2T from superconducting quantum interference device (SQUID) measurements in Ref. 45. This canting angle is small and depends sinusoidally on the applied field ( $\mu_0 H \propto \sin \theta$ , if  $\theta$  is the canting angle), so it can be assumed to be linear, leading to an estimated canting angle of < 1° at 8 T. At 1° canting, the total contribution of canted moments to the remnant signal is approximately 1 % of the fully aligned signal and so the remaining remnant signal can be attributed to 180° domain walls and topologically protected features and pinned domains such as those induced by structural defects [53, 54, 57].

The ability for magnetic neutron diffraction to measure the spin flop transition in uniaxial CuMnAs films as thin as 20 nm was demonstrated. The uniaxiality of the samples was shown to be high, at ≈80 % and ≈90 % uniaxial for the 45 nm and 20 nm samples, respectively. The neutron diffraction results agree strongly with the transport measurements, which show a maximum AMR signal of 0.25 % and 0.15 % for the 45 nm and 20 nm films, respectively.

Due to the duration of scans, instantaneous manipulation of the Néel vector from effects such as electrical switching [25] would not be detectable in neutron diffraction. For any effects which create stable reorientation or which can somehow be maintained, this technique could provide insight into the extents of the manipulation, previously inaccessible through other techniques such as microscopy of transport measurements. The technique is limited by its duration and the symmetry of the materials, where CuMnAs is a good candidate for using neutron diffraction to probe other manipulations of the magnetic order

using neutron diffraction.

Magnetic neutron diffraction has been demonstrated to be a robust, quantitative measure of the magnetic ordering in CuMnAs films as thin as 20 nm. The technique is capable of determining the unambiguous, total volume extents of spin flop even for films with such small volumes. There is good agreement between the results found in neutron diffraction and in transport measurements indicating that both methods measure the magnetic order. Overall, this result indicates that the technique should be applicable for measuring the magnetic Néel vector magnitude and direction of any such compatible magnetic crystals.

# Chapter 4

## Optical Probing of Magnetic Ordering in Thin Film CuMnAs Samples

### 4.1 Introduction

Polarised light incident on a magnetic material will experience different local refractive indices based on the relative geometry of the polarisation and wavevector with respect to the magnetisation direction. When measuring a transparent ferromagnet, the Faraday and Voigt effects describe the changes in polarisation observed when light is transmitted through the material with a wavevector,  $\underline{k}$ , parallel and perpendicular to the magnetisation, respectively. These two geometries are illustrated in Fig. 4.1 where (a) describes the Faraday geometry and (b) describes the Voigt geometry. These two geometries result in different effects. In the Faraday geometry, the Faraday effect is observed when light is transmitted along the magnetisation axis through a material that has a different refractive index for light with opposite circular polarisation directions, which is magnetic circular birefringence. This means that linearly polarised light, which is an equal superposition of polarisations with opposite rotation directions, will have its plane of polarisation rotated proportionally to

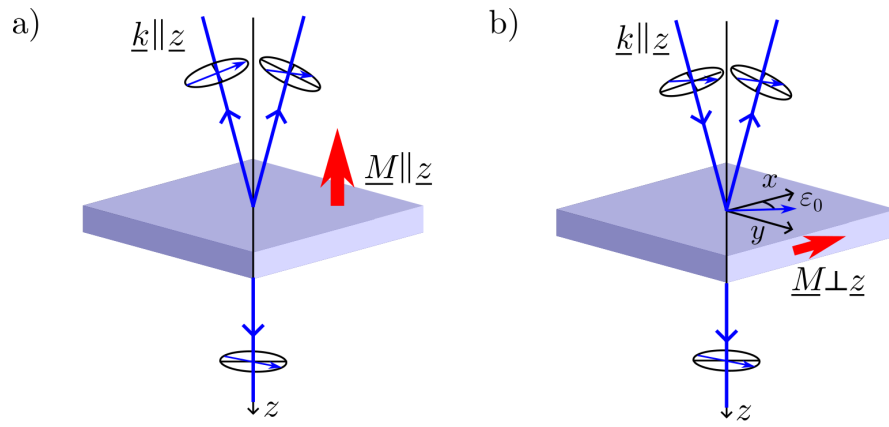


Figure 4.1: Illustrations of (a) Faraday Geometry (b) Voigt Geometry.

the difference in these refractive indices and as a function of the path length through the material. In a material exhibiting absorption, the difference in refractive indices also creates a difference in absorption coefficients, which is called magnetic circular dichroism, and therefore there will be a change in magnitudes of each component and so the polarisation will become elliptical (creating a deviation from linear polarisation). The polar Kerr effect describes these polarisation changes when the light is instead reflected off the sample.

In the Voigt geometry, the Voigt effect (also known as the Cotton-Mouton effect) is the combination of magnetic linear birefringence (MLB) and magnetic linear dichroism (MLD) and these replace the circular cases. The Voigt effect results from a difference in refractive indices for linear polarisations parallel and perpendicular to the magnetic field in the material when the light is propagating perpendicular to the magnetic field. When the incident polarisation is parallel or perpendicular to the magnetic field there is no change to polarisation because only one refractive index is involved, but at any other angle of incident polarisation, the Voigt effect causes changes to the outgoing polarisations.

In the transparent case, MLB causes linearly polarised light to become elliptical with the resulting extent of ellipticity being a function of the difference in the real parts of the refractive indices and the path length in the material. When the material also exhibits absorption, i.e. having a difference in the imaginary parts of the refractive indices, MLD causes the plane of polarisation

to be rotated as well. When reflected, MLB and MLD are similar to their transmission counterparts but are no longer a function of the path length in the material.

The Faraday and Kerr effects are linearly proportional to the magnetisation of the sample,  $M$ , and so are not expressed in fully compensated AFMs such as CuMnAs. The Voigt effect and MLD, however, are proportional to  $M^2$  and so the sublattice magnetisation should cause these effects in CuMnAs. For the first time, the Voigt effect was used to determine the orientation of the Néel vector of uniaxial CuMnAs samples by Saidl et al [35]. In that study, a pump-probe optical technique was employed to detect the change in polarisation which occurs as a result of pump-induced heating in the sample which leads to some demagnetisation. Because the magnetisation is reduced, the optical anisotropy of the probing light is reduced. A probe beam with chosen incident polarisation was used to measure this pump-induced demagnetization-related change in the polarisation angle, called there the magnetooptical (MO) signal, as a function of time after the pump pulse. This measurement was repeated with many incident polarisations,  $\varepsilon$ , measured relative to the Néel vector, in order to detect the angular dependence of the signal. Figure 4.2 contains a summary of the main results obtained in Ref. 35, where (a) demonstrates the decaying changes in demagnetisation signal, corresponding to the change in polarisation angle as a function of time for three incident polarisation angles, measured relative to the anticipated magnetic easy axis i.e. the Néel vector. It shows that the signal is almost zero when the polarisation is parallel to the easy axis, and the sign of the signal changes between  $+45^\circ$  and  $-45^\circ$ . Figure 4.2(b) demonstrates the transmissivity changes induced by the change in temperature. This result shows a very minor angular dependence on this signal but no change in sign of the signal. Both (a) and (b) show that the signal is almost entirely extinguished within 1 ns at 15 K. Figures 4.2(c-d) show the angular dependence of the maximum MO signal at many incident angles to demonstrate the  $\sin(2\varepsilon)$  dependence where (c) is measured in transmission and (d) is measured in

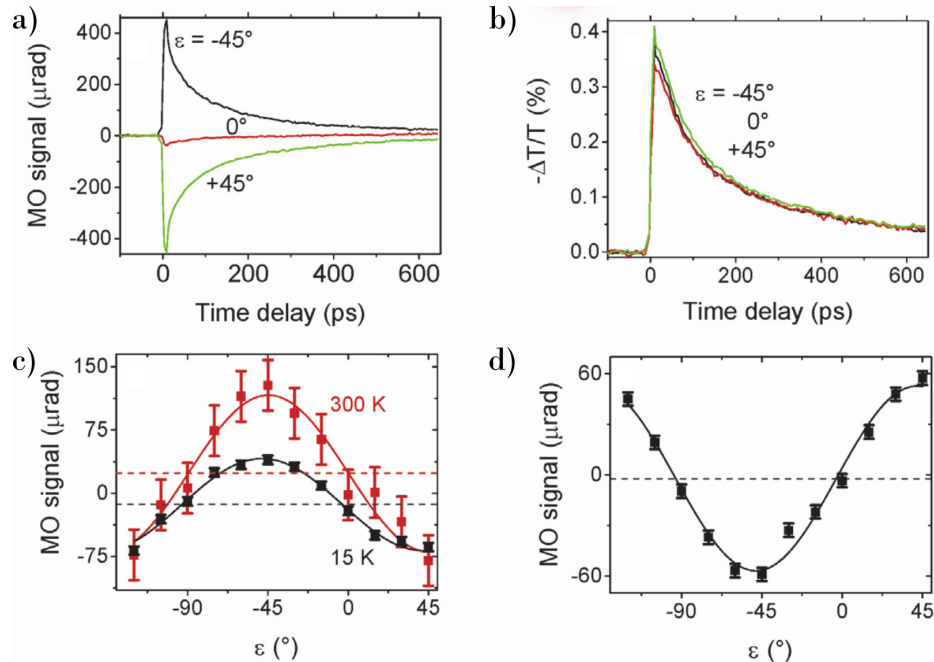


Figure 4.2: A summary of findings by Saidl et al in which the authors experimentally observed the uniaxial magnetic anisotropy of a 10 nm CuMnAs film grown on GaP(001). (a) Time-resolved pump-induced changes to polarisation angle measured by probe pulses with different incident polarisations measured relative to the  $[1\bar{1}0]$ CuMnAs direction ( $\varepsilon$ ) in transmission geometry at a sample temperature of 15 K. (b) Time-resolved transmissivity changes measured simultaneously with the MO signal shown in (a). (c) Probe-polarization dependence of pump-induced change polarisation at 15 K (black points) and 300 K (red points) where  $\varepsilon = 0^\circ$  corresponds to polarization plane along the  $[010]$  direction in CuMnAs. Solid lines are fits following a  $\sin 2\varepsilon$  dependence plus polarization-independent backgrounds, which are shown by dashed horizontal lines. (d) is the same as (c) only in reflection geometry at 15 K. Figure adapted from Ref. 35.

reflection. (c) Also shows a comparison between the signal amplitude at low temperature (15 K) in black and room temperature (300 K) in red. This study successfully determined the Néel vector of uniaxial CuMnAs samples grown on GaP(001) substrates in both a reflection mode and transmission mode optical pump probe measurements using delay lines. The use of delay lines means that the experiments can take many hours to perform, due to difficulties in finding the overlap of the two beams and the time taken to measure the signals.

The use of magneto optical approaches to image the domain structure of AFMs is attractive due to accessibility (compared to facility based XMCD-PEEM, for example) and so the studies contained in this chapter aim to progress the understanding of these processes in order to aid development of such a technique. To this end, this chapter describes the use of asynchronous optical sampling (ASOPS) as a replacement for delay-line pump probe as a tool to rapidly characterise the anisotropy of CuMnAs films. In order to do so, ASOPS setups are designed to allow for the measurement of pump-induced polarisation angle changes in both transmission and reflection modes. Only CuMnAs samples grown on GaP(001) were measured previously so a sample grown on GaAs(001) is studied in reflection mode to demonstrate that the Voigt effect is reproducible and can be used for characterization of CuMnAs layers. Finally, the reorientation of moments induced by spin flop is detected by applying a magnetic field of 4.5 T while using a delay line pump probe technique. This aimed to detect the difference in polarisation change signals before and after spin flop.

In order to describe the experiments, a description of polarised light is given before the MLB and MLD are described in more detail, including a description of the expected results from the studies. Two distinct optical pump probe techniques are used (ASOPS and delay line) so the experimental schemes of these are given, including a summary of associated optical components and ancillary equipment. The methods for the studies are provided before the results are discussed and the final conclusions are made.

## 4.2 Relevant Magneto optics

In this section, a description of polarised light is given before how the Voigt effect changes the polarisation of light is described. The expected behaviours of pump-induced demagnetisation is summarised with reference to domain structure and spin flop.

### 4.2.1 Polarisation of light

For an electromagnetic wave in a vacuum with a direction of propagation given by the wave vector  $\underline{k} = (\omega/c)\underline{n}$ , the wave at position  $\underline{r}$ , at time  $t$ , can be described by the propagation of electric field  $\underline{E}$  and magnetic field  $\underline{B}$  in the form

$$\underline{E}(\underline{r}, t) = \underline{E}_0 e^{-i(\omega t - \underline{k} \cdot \underline{r})} \quad (4.1)$$

$$\underline{B}(\underline{r}, t) = \underline{B}_0 e^{-i(\omega t - \underline{k} \cdot \underline{r})} \quad (4.2)$$

where  $\omega$  is the angular frequency, and  $\underline{E}_0$  and  $\underline{B}_0$  are the amplitudes of the waves. As  $\underline{E}$  and  $\underline{B}$  are orthogonal in a vacuum, only one of the above is necessary to describe the wave fully.

The above described wave can have polarisation, in which the  $\underline{E}$ -vector of the wave describes an ellipse that is perpendicular to the direction of propagation. If the direction of propagation is chosen  $\underline{k} \parallel \underline{z}$  then a wave propagating in a vacuum is described by

$$E_x = a \operatorname{Re} [e^{-i(\omega t - kz)}] \quad (4.3)$$

$$E_y = b \operatorname{Re} [e^{-i(\omega t - kz - \delta)}] \quad (4.4)$$

where  $a$  and  $b$  are the real amplitudes of the  $x$  and  $y$  components of the wave, respectively, and  $-\pi \leq \delta \leq \pi$  is the phase difference between these two components. The resulting elliptisation is drawn in Fig. 4.3 where (a) illustrates

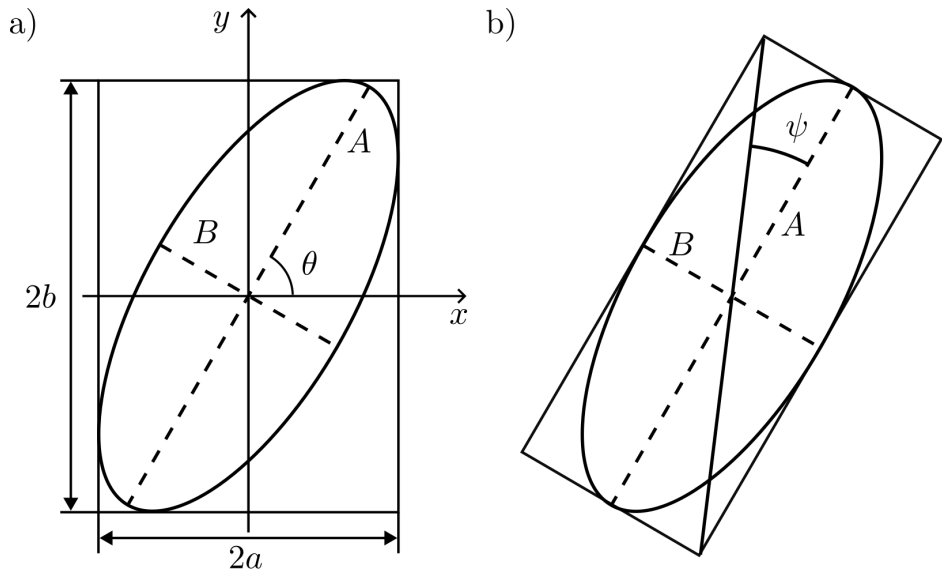


Figure 4.3: The polarisation ellipse of light describing the angle of polarisation (a) relative to the  $x$ -axis and (b) between the major axis of the ellipse and the diagonal of the inscribing rectangle.

the polarisation angle  $\theta$ , defined relative to the  $x$  direction and (b) describes the ellipticity angle  $\psi$ , defined as the angle between the major axis  $A$  and the diagonal of the inscribing circle. If  $\psi = \pm\pi/4$  then  $\delta = \pi/2$ ,  $a = b$  and the light is circularly polarised while light with  $\delta = 0$ , then  $\psi = 0$  is linearly polarised.

#### 4.2.2 The Voigt Effect

In magnetic materials, the interaction of the light with the local magnetisation causes a difference in refractive indices for different polarisations. In the Voigt geometry, shown in Fig. 4.1(b), the Voigt effect is caused by a difference in the refractive index for light with polarisation parallel to the local magnetisation ( $n_{\parallel}$ ) and perpendicular to it ( $n_{\perp}$ ). Both of these refractive indices are complex numbers, therefore having real and imaginary parts. When considering an AFM such as CuMnAs, light with incident polarisation at  $45^\circ$  to the Néel vector can be decomposed into equal components parallel and perpendicular to the Néel vector. In this case, the light experiences the maximum difference in refractive index between each component. The real part of the difference, described by MLD, leads to a difference in the wavelength in the material and

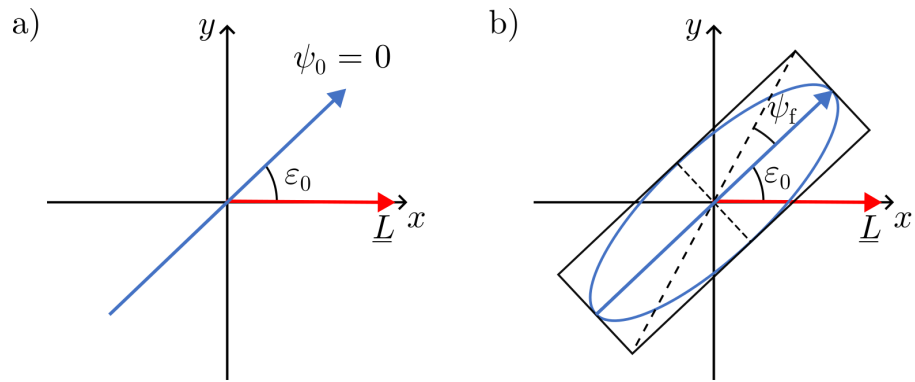


Figure 4.4: Illustration of the  $x$ - $y$  projection of polarisations to indicate the change in ellipticity of (a) incident linear polarisation and (b) reflected or transmitted elliptical polarisation, when the incident polarisation is linear and at  $45^\circ$  to the Néel vector,  $\underline{L}$ .

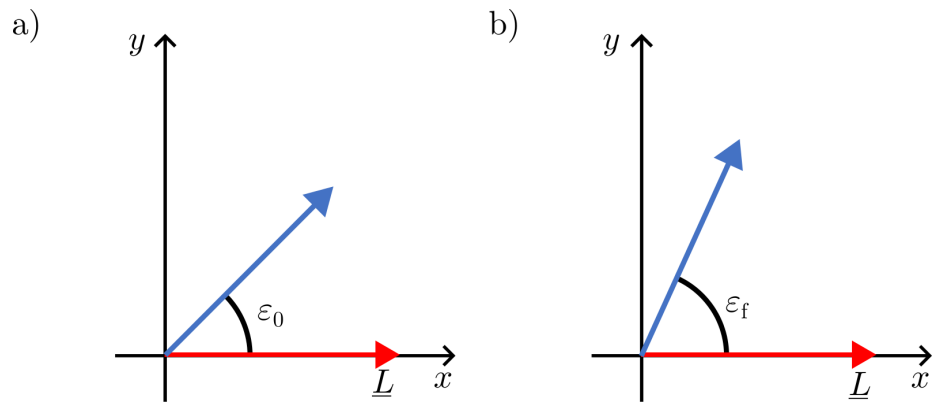


Figure 4.5: Illustration of the  $x$ - $y$  projection of polarisations to indicate the change in linear polarisation angle of (a) incident linear polarisation and (b) reflected or transmitted linear polarisation after undergoing the rotation, when the incident polarisation is linear and at  $45^\circ$  to the Néel vector,  $\underline{L}$ .

thus a phase difference is introduced as the light is transmitted through the material. This change in phase causes the polarisation to become elliptical. This phase difference is given by

$$\delta = \frac{\omega}{c} \operatorname{Re}(n_{\parallel} - n_{\perp})d \quad (4.5)$$

where  $d$  is the path length of the light within the material, i.e. the thickness of the film. This change is illustrated in Fig. 4.4 where (a) shows the incident polarisation with  $\varepsilon_0 = 45^\circ$  and  $\psi = 0$  while (b) shows the resulting polarisation of light after undergoing an ellipticity change of  $\Delta\psi = \psi_f - \psi_0$ .

The imaginary part of the difference in refractive indices, described by MLD, causes a difference in the absorption coefficients for the components parallel ( $\alpha_{\parallel}$ ) and perpendicular ( $\alpha_{\perp}$ ) to the Néel vector. The absorption coefficients are related to the refractive indices by

$$\alpha_{\parallel} - \alpha_{\perp} = \frac{4\pi}{\lambda} \operatorname{Im}(n_{\parallel} - n_{\perp}) \quad (4.6)$$

where  $\lambda$  is the wavelength of the incident light in a vacuum. MLD causes one component to attenuate more strongly than the other and leads to a change in the ratio  $a/b$ , and thus the polarisation rotates. The resulting rotation angle change is illustrated in Fig. 4.5 where (a) shows the incident polarisation with the Néel vector parallel to the  $x$ -axis such that  $\theta = \varepsilon = 45^\circ$  and (b) shows the resulting polarisation of light after undergoing a rotation of  $\Delta\varepsilon = \varepsilon_f - \varepsilon_0$ .

The total change in polarisation is the combination of these two effects and this is the Voigt effect. If the incident polarisation is chosen to be at  $\pm 45^\circ$  to the Néel vector, and if the film is thin or the difference in refractive indices is small, i.e.  $\omega/c(n_{\parallel} - n_{\perp})d \ll 1$ , then the changes to polarisation in transmission are captured by

$$\Delta\varepsilon - i\Delta\psi \approx -\frac{i\omega}{2c}[n_{\parallel} - n_{\perp}]d. \quad (4.7)$$

In reflection mode measurements, the same effects persist but are a result of

surface interactions only. The resulting changes to polarisation are described independently of the thickness of the film, and instead are related to the difference in reflectivities for the two components of polarisation. In this case, the resulting polarisation changes remain proportional to the difference in refractive indices [62], but the exact extents of rotation and change in ellipticity are more complicated. MLB will induce some change in ellipticity because of the phase difference between the reflected components and will induce some rotation as well. MLD will also change the phase and cause ellipticity changes, but whether it rotates the polarisation is not guaranteed without knowing the values of the imaginary parts of the refractive indices.

In the general case of incident linear polarisation with arbitrary angle, the magnitude of the change in linear polarisation angle,  $\Delta\varepsilon = \varepsilon_f - \varepsilon_0$  is related to the relative orientation of the polarisation angle with respect to the Néel vector,  $\varepsilon$ , following a

$$\Delta\varepsilon \propto \sin(2\varepsilon) \quad (4.8)$$

dependence [35]. This describes the behaviour in which there is change to the polarisation as a result of the Voigt effect when the polarisation is parallel or perpendicular to the Néel vector, and the changes should be maximum for polarisations incident at  $\pm 45^\circ$  to the Néel vector for both reflected and transmitted light.

#### 4.2.3 Expected Demagnetisation Behaviour in CuMnAs Samples

The magnitude of the difference in refractive indices is proportional to the square of the sublattice magnetisation,  $M^2$ , and so as the heat raises the sample closer to the Néel temperature and partially demagnetises the sample, the magnitude of  $M$  is reduced. This reduction leads to a reduction in the change in polarisation resulting from the Voigt effect. This can be detected as a change from the static polarisation. If the sample is fully demagnetised, the

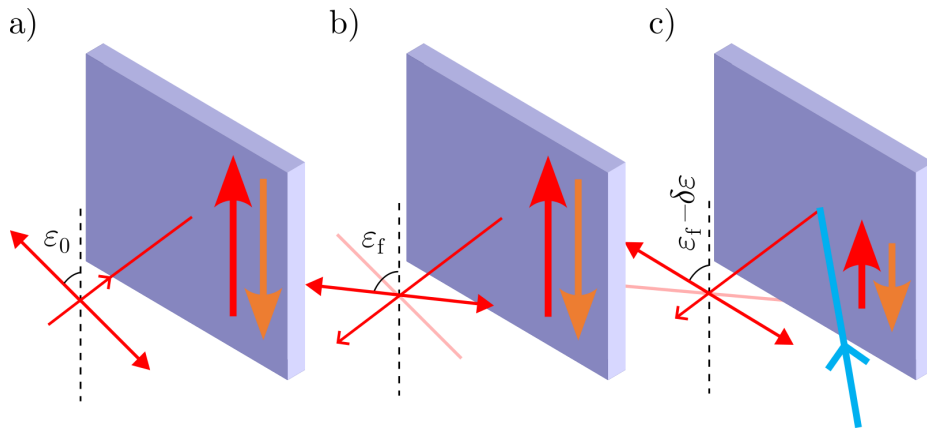


Figure 4.6: Schemes showing the expected rotation of polarisations as a result of the Voigt effect and MLD in reflection mode where (a) shows the incident polarisation (b) shows the reflected polarisation angle in the steady state and (c) shows the reflected polarisation directly after the demagnetisation effects of a pump pulse. The red and orange arrows represent the sublattice magnetisations  $M_1$  and  $M_2$ , respectively and the blue arrow represents the blue pump pulse incident at  $\approx 45^\circ$  to the sample surface. The translucent line in (b) shows the incident polarisation and the translucent line in (c) shows the reflected polarisation at angle  $\varepsilon_f$  from (b).

resulting polarisation returns to the incident case ( $\varepsilon_f \rightarrow \varepsilon_0$ ) and the resulting demagnetisation signal corresponds to the total resulting change in polarisation from the Voigt effect. In the case that the sample is not fully degmagnetised then the resulting signal is proportional to square of the extent of demagnetisation. Non-magnetic contributions to the outgoing polarisations are removed by only measuring the pump-induced changes to magnetisation, as was shown in Ref. 63.

Figure 4.6 illustrates the expected behaviour in reflection mode where the expected polarisation angles are drawn for (a) the incident polarisation (b) the steady state reflected polarisation and (c) shows the reflected polarisation directly after the demagnetisation by the pump pulse. The extent of polarisation due to the Voigt effect is largest in the steady state and is reduced by  $\delta\varepsilon$  due to the demagnetising effect of the pump pulse.

Similarly, Fig. 4.7 illustrates expected behaviour in transmission mode where the expected polarisation changes for (a) the incident and transmitted polarisations in the steady state and (b) the incident and transmitted polarisations directly after the demagnetisation due to the pump pulse.

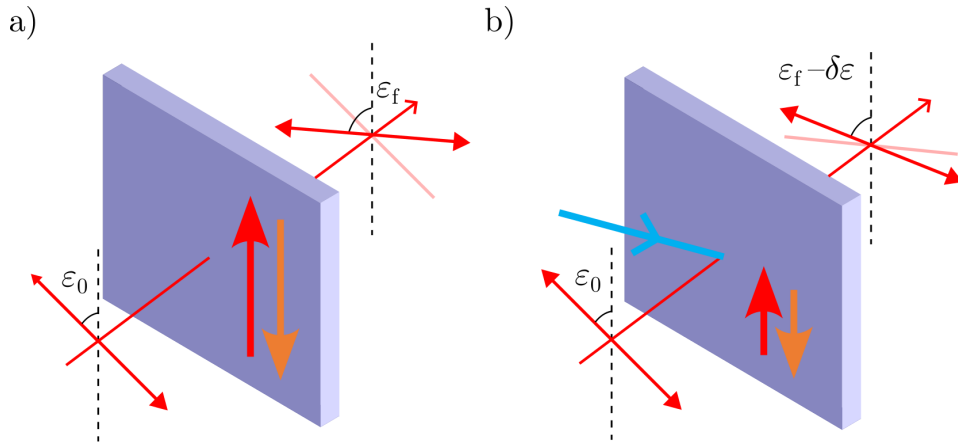


Figure 4.7: Schemes showing the expected rotation of polarisations as a result of the Voigt effect and MLD in transmission mode where (a) shows the incident polarisation and transmitted polarisations in the steady state and (b) shows the incident and transmitted polarisations directly after the demagnetisation effects of a pump pulse. The red and orange arrows represent the sublattice magnetisations  $M_1$  and  $M_2$ , respectively and the blue arrow represents the blue pump pulse incident at  $\approx 45^\circ$  to the sample surface. The translucent line in (a) shows the incident polarisation and the translucent line in (b) shows the steady state transmitted polarisation at angle  $\varepsilon_f$ .

Figure 4.8 illustrates the expected polarisations without (a,b) and with (c,d) the magnetic field applied along the easy axis, i.e. before and after spin flop, respectively. (a,c) show the incident and transmitted polarisations in the steady state while (b,d) show the polarisations directly after the demagnetisation due to the pump pulse. With the field applied along the hard axis of a uniaxial sample, the moments should not undergo reorientation and so the system should resemble (a,b) with and without the applied field.

In most uniaxial CuMnAs samples, the domain structure consists of domains with their Néel vectors predominantly aligned along the easy axis, with only the moments within  $180^\circ$  domain walls and those pinned by defects being aligned differently. Because the domains are oriented  $180^\circ$  apart, the contribution to the Voigt effect from each domain is the same, and so these systems can be considered the same as a single domain system containing only one Néel vector. Once undergoing spin flop, most of the moments should rotate through  $90^\circ$  and therefore the sign of the steady state polarisation change is opposite for

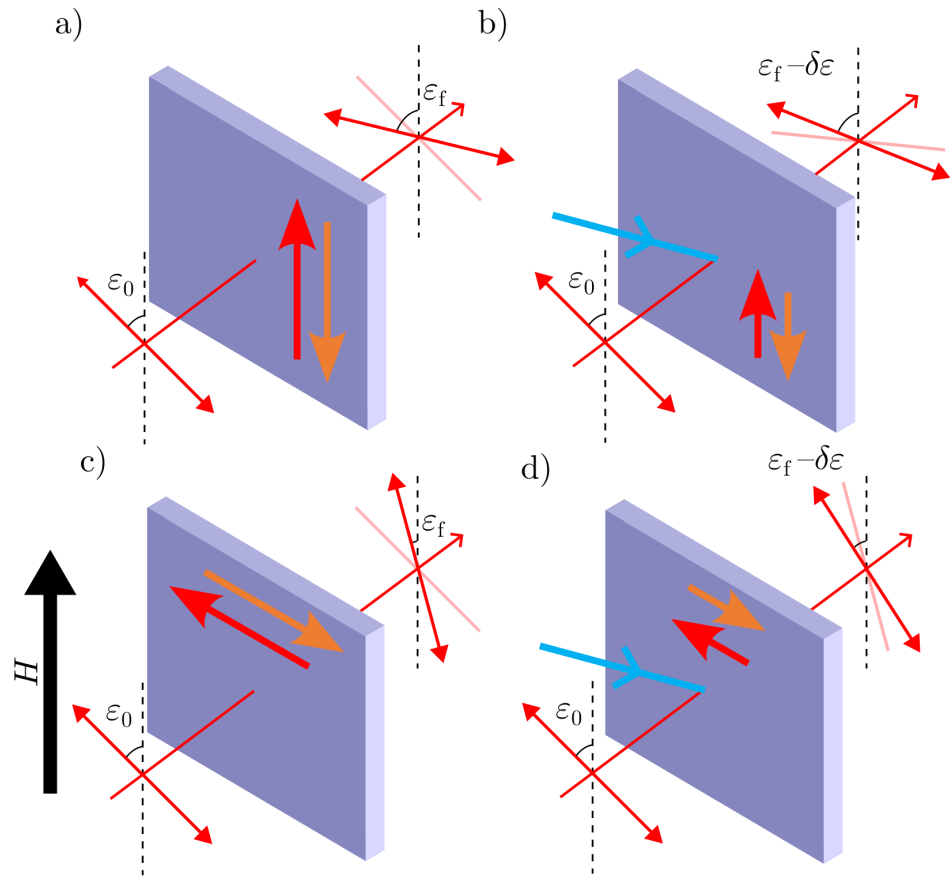


Figure 4.8: Schemes showing the expected rotation of polarisations as a result of the Voigt effect and MLD in transmission mode before and after spin flop where (a,c) show the incident polarisation and transmitted polarisations in the steady state and (b,d) show the incident and transmitted polarisations directly after the demagnetisation effects of a pump pulse. (a,b) correspond to the zero field state and (c,d) correspond to the case after spin flop with the magnetic field,  $H$ , applied along the easy axis as indicated by the black arrow. The red and orange arrows represent the sublattice magnetisations  $M_1$  and  $M_2$ , respectively and the blue arrow represents the blue pump pulse incident at  $\approx 45^\circ$  to the sample surface. The translucent lines in (a,c) show the incident polarisations while the translucent lines in (b) and (d) show the steady state transmitted polarisations at angle  $\varepsilon_f$ , drawn in (a) and (c) respectively.

the same incident polarisation, and the expected demagnetisation signal should then have the opposite sign.

For a biaxial sample, domains separated by  $90^\circ$  will contribute oppositely to both the steady state Voigt effect and the demagnetisation changes. If the probe spot size is much larger than the domain sizes, then, without external field, all angles of incident polarisation should give no demagnetisation-related signal. After spin flop, the proportion of domains perpendicular to the applied field will increase and so the magnitude of the signal should increase and start to behave the same as a uniaxial sample, with the magnitude being proportional to the extent of reorientation of moments in the sample. Due to the inhomogeneity of the domain structure, the magnitudes of the observed signals in biaxial samples will vary across the sample and so sometimes a signal may be observed without external field since the proportion of observed domains in each orientation may be uneven. If the measured spot is largely uneven, it is also possible that the reorientation of moments could cause the signal to be reduced by changing the proportion of domains to be closer to even. This makes the measurement of biaxial samples much more complex than for uniaxial samples.

For CuMnAs films grown on GaP(001), both transmission and reflection mode measurements can be conducted because GaP is transparent for the used probe wavelengths ( $\approx 800$  nm). Because of this, the transmission mode measurements will give larger signals simply because GaP has a higher transmittivity than reflectivity in this wavelength range. On CuMnAs films grown on GaAs(001), transmission measurements are not possible because GaAs is opaque to the probe wavelengths used. This means that the reflection mode measurements must be used, and should give larger reflected intensity than the GaP(001) grown films.

## 4.3 Optical Pump Probe Techniques

Optical pump probe techniques use two lasers, one to induce some change in the material using pump pulses, and another to detect the resulting changes in optical properties using a probe pulse. The time difference between these two pulses is adjusted in order to measure the decay of the changes as a function of time, called a trace. In this chapter, two distinct techniques are used to vary the time between the pulses: asynchronous optical sampling (ASOPS) and the use of delay-lines. ASOPS uses the stroboscopic effect to continuously vary the time difference between a pump pulse and probe pulse by having two different repetition rates of the pulses from two lasers. In the contained delay line technique, one laser is split into two beams and the path length of one of the beams is varied to change the relative time of arrival of the pulses. The following section describes these two techniques in more detail before giving a description of the optical components and ancillary equipment required to understand the experiments conducted in this chapter.

### 4.3.1 Ti:Sapphire lasers

A Ti:Sapphire (specifically Ti:Al<sub>2</sub>O<sub>3</sub>) crystal, when pumped with green light, will emit a broadband light covering much of the red/near-IR spectrum. The output can be tuned, both in resonant frequency and in wavelength. The Ti:Sapphire lasers used in these studies convert continuous wave 532 nm beams into high power ps or fs pulsed beams with the capability to select from 700–1080 nm with a repetition rate of 80 MHz (12.5 ns period). The selection mechanism uses prisms to distribute the light and a slit is used to select the wavelength of choice. The cavity also includes an acousto-optic modulator and oscillating mirror which, together, allow the cavity to resonate at the necessary period to isolate the desired laser mode and create  $\approx$ 100 fs pulses. This process is called mode-locking. The resonant frequency of the cavity is determined by the round-trip path length of the cavity, typically around 4 m. These lasers

allow for very high power, ultrashort pulses to be produced in a narrow, tunable wavelength distribution. This is useful because the temporal resolution of optical spectroscopy measurements is limited by the pulse width and non-linear optical effects, such as second-harmonic generation (SHG), require very high power densities to exhibit the desired effects.

#### 4.3.2 Asynchronous Optical Sampling (ASOPS)

ASOPS is a pump-probe optical technique in which two pulsed lasers are tuned such that their pulse rates are slightly different. The technique cannot achieve temporal precision to the same degrees as a delay-line pump-probe technique (described below) but allows for much faster measurements and easier alignment. Therefore, this technique is excellent for prototyping and characterisation. The speed is such that the results can be seen in real time using an oscilloscope and there is no need to mechanically move optics on stages and wait for the consequent vibrations to subside, yielding measurement rates in the order of 1000 traces per second.

In order to achieve this measurement rate, ASOPS utilises the strobe effect generated by offsetting the repetitions rates of one of the lasers relative to the other. If the pump pulse is set to be faster, this results in each consecutive probe pulse arriving with a larger delay between pump and probe pulse than the previous probe pulse. The temporal precision of such a set-up is determined as the difference in time periods between the two pulse trains. In the experiments described here, the pulse rate of the lasers,  $f_{\text{Pu/Pr}}$  is of the order 80 MHz with a difference in pulse rate,  $\Delta f$ , in the order  $< 1$  kHz. For  $\Delta f = 800$  Hz the resulting temporal resolution is  $\approx 0.125$  ps and a full trace of signal versus time is at the rate of  $\Delta f$  meaning that averaging is rapid and achieves good signal-to-noise. A typical point in a trace is the result of 100,000 or 1,000,000 averages taken in less than an hour. In the following ASOPS studies, each point in time is the average of 8 points, binned to the centre of the group; this

is simply to improve data density and rate of measurement. There is no need for a lock-in amplifier in ASOPS, instead, the measured signals are fed to an oscilloscope for real time monitoring and to an analogue-to-digital converter (ADC) for measurements with more averaging.

A Red Pitaya multifunctional measurement system was used as the ADC in the ASOPS experiments because it has a field-programmable gate array (FPGA), which is a programmable circuit board that allows for rapid parallelisation of data processing, and 10-bit 125 MHz ADC built in. The FPGA was programmed to measure 10000 traces in a batch and then handle the averaging of those traces and the transfer of data to the control computer concurrently with measuring the next batch of traces.

For each Ti:Sapphire laser in the ASOPS experiments, there are several ways in which the repetition rate can be changed. In all cases it is the optical path length of the beam inside the laser that is adjusted since the laser is a resonant cavity. The position of the back mirror, the location of the wavelength selection slit and amount of accompanying compensation prisms in the beam are the most common adjustments. In our case, the probe laser was set to a fixed frequency and the pump laser was fitted with a computer controlled slip-stick piezoelectric motor for back mirror adjustment. Because two lasers are used in ASOPS, the stability of both lasers must be good or the difference in repetition rate must be continuously monitored. By mixing the repetition rates of each laser (read from an internal photodiode) the difference and sum of the repetition rates can be measured. By using the difference as an input into a PID control, the back mirror of the pump laser was adjusted by this PID .

### 4.3.3 Delay-Line Pump-Probe

Delay-line pump probe can achieve temporal resolutions suitable for THz spectroscopy, limited by the duration of the pulses of the laser used, which can be  $\leq 100$  fs. This is achieved by changing the path length between two

laser beams to affect the relative arrival time of the probe pulse after the pump pulse. By splitting the output of one pulsed laser into a pump beam and a probe beam and controlling the path length difference between the two beams, the relative arrival time of a probe pulse after a pump pulse can be controlled using a retro-reflector on a sliding stage. This combination of a retro-reflector and a linear stage is called a delay-line and is the technique's namesake. The resolution of the time of arrival is determined by how precisely the path length can be controlled, which can typically be in the  $1 \mu\text{m}$  range, so results in 3 fs time of flight precision. Since the shortest pulse width from the Ti:Sapphire lasers used is  $\approx 100$  fs, the limiting factor in the temporal resolution is the pulse width.

The signal measured in a delay-line pump probe experiment is noisy and the effects that are being measured are typically much smaller in amplitude than this noise, therefore some technique must be employed to extract the signals. In these delay-line experiments, a lock-in amplifier was used. A lock-in amplifier is an analogue voltmeter which can extract small signals in noisy environments where the signal is of a known frequency. They are typically used in situations where a DC amplifier would fail to measure the desired signals. The lock in amplifier is passed a reference signal  $s_1$  of frequency  $f_1$  which is mixed with the input signal  $s_2$  which also contains a component with an oscillation of frequency  $f_2$ . Due to the orthogonality of sine waves, the mixing of  $s_1$  and  $s_2$  will yield zero for any signal where the frequencies are different ( $f_1 \neq f_2$ ) when integrated over a sufficient number of cycles. In order to extract a useful signal, the mixed signal must be integrated over some time, typically several orders of magnitude larger than the period of the reference signal. The resulting value can then be sampled periodically, and a mean can be calculated from these samples. In order to feed an oscillating signal into the lock-in amplifier, some property of the pump or probe beam must be affected in a sinusoidal manner, such as oscillating the intensity of the pump beam or polarisation of the probe beam.

In these delay-line experiments, the pump beam intensity is varied sinusoidally by using the photo-elastic modulator (PEM) to oscillate the polarisation, incident on a polarisation filter to create an oscillation in intensity instead. In this case, the desired signal is zero for any time the pump beam is off and is expected to be non-zero whenever the pump beam is incident. By using the driving frequency of the PEM as a reference signal into the lock-in amplifier, all signals that do not oscillate at the same frequency as the PEM are removed by the lock-in amplifier, leaving only the changes in signal caused by the pump beam, thus eliminating much of the noise.

#### 4.3.4 Descriptions of Ancillary Equipment

In both ASOPS and delay-line techniques, the polarisation change is ultimately measured by the amount of light on each half of a split detector. A split detector consists of two photodiodes with opposing polarity as inputs to an amplifier circuit such that light on one photodiode cancels out the voltage generated by the light on the other. This allows for balancing of the signal to zero in the steady state and amplifying the small changes. Without this, the signals would saturate the amplifier circuitry, and the changes would be undetectable above the noise of such an effect. Often these detectors have frequency filters to eliminate the oscillations from the pulse. By blocking one input, the transmissivity or reflectivity change caused by a pump pulse can be detected since the other diode no longer cancels out the change in intensity. To measure the voltage for balancing both inputs are exposed to the light and the polarisation is adjusted until the measured signal is zero when readout on a normal voltmeter.

The split detector is AC coupled which means it does not measure the DC amplitude with steady state illumination. Therefore, to measure the DC magnitude of the incident light, an optical chopper can be used. A chopper is simply a wheel with alternating open and closed sections which spins to

block and expose a beam. Attached to the chopper's housing is a light gate which detects the frequency of oscillation for use with a lock-in amplifier. In the following studies, the frequency is not important and by oscillating the light, the stepwise change in intensity can be measured on an oscilloscope to determine the DC magnitude of light incident on each diode of the detector.

A spectrum analyser simply shows a plot of the wavelength distribution of an input light. They are essential with Ti:Sapphire lasers for tuning and choosing the output wavelength distribution. When Ti:Sapphire lasers are not tuned and mode-locked properly, the resulting behaviour can still output high power laser light, however when not mode-locked, the laser either operates in continuous wave (CW) mode or emits low power pulses off resonance. The spectrum analyser is also used to monitor the lasers and ensure that they are mode-locked.

In ASOPS experiments, it is important to have a reference time for when the beams emit pulses simultaneously. In order to find this time, a trigger detector is used which consists of a photodiode and a thresholding circuit. The photodiode is illuminated by both beams but cannot generate a voltage above a certain level unless two pulses arrive concurrently. In the concurrent case, the photodiode will emit a drastically larger voltage during the concurrent pulses, which is fed into the thresholding circuit. The circuit can be tuned to emit a trigger signal (short 5 V pulse) whenever the voltage from the photodiode is above a certain level, and the level can easily be adjusted. The trigger signal is then used to start a trace at a consistent point in measurement time and allows averaging.

#### 4.3.5 Descriptions of Optical Elements

The studies described in this chapter measure polarisation and so it is key to be introduced to some of the optical elements used. Firstly the polarisation optics are described and then the process of generating blue light from a red

light beam is described.

A half-wave ( $\lambda/2$ ) plate is wavelength specific optical element that allows the user to rotate the polarisation of any linearly polarised light. The polarisation is reflected along the fast axis of the half-wave plate i.e. light with polarisation at  $45^\circ$  to the fast axis becomes  $-45^\circ$  to the same axis, assuming the wavelength is the same as the specification. Half-wave plates are typically made by coating glass with a birefringent material (a material with different refractive indices along two crystal axes). The thickness of this film is chosen such that light passing perpendicularly through the material will have its polarisation delayed by half a wavelength along one axis relative to the other axis, resulting in the described behaviour.

There are four types of beam splitter used in these studies. The simplest is a regular plate beam splitter which splits the beam by the specified ratio, however these can introduce polarisation changes due to the phase shift introduced by passing through the glass, a dielectric material. Therefore, in regions where the polarisation must be un-altered, a non-polarising beam splitter is used instead. These beam splitters have coatings and are made from specific glasses to minimise the phase shifts. The other two are the Glan prism and Wollaston prism, both of which split the incident beam into beams made up of the vertical and horizontal components of polarisation. They both work by sandwiching a thin film of birefringent material between the hypotenuses of two triangular prisms. The only difference between the two is the proportions of the triangles and therefore the angle of the reflected output. The thin film reflects light with polarisation along one axis while the rest is transmitted.

Second harmonic generation (SHG) is the combining of two photons to generate one photon with half the wavelength (double the energy) and can be performed in several non-linear optical media. Conveniently, inputting pulsed light will yield pulsed light of the same frequency and pulse duration. In these studies, a barium borate (BBO) crystal is used as the non-linear medium and the pump beam is converted from red light to blue light using SHG. In

order to perform SHG, the input beam must have its polarisation axis and direction of travel aligned precisely with certain axes in the BBO crystal and the power density, in both space and time, must be very high. To achieve this, Ti:Sapphire lasers provide the temporal density and lenses are used to focus the beams on the centre of the crystal. A half-wave plate is used to select the polarisation. The output beam must be filtered to remove the any light that did not undergo SHG, which can be done using a piece of glass with a wavelength specific reflective coating, called a wavelength selecting mirror (in this case a hot-mirror).

A neutral density (ND) filter is a filter than attenuates all wavelengths of light equally without affecting polarisation. Graduated (adjustable) and uniform ND filters are used to reduce the incident powers of the pump and probe beams.

## 4.4 Methods

This section contains the experimental methods used in three different studies, all using pump-induced demagnetisation-related changes to the polarisation angle, using the Voigt geometries illustrated in Fig. 4.1(b). Two studies used ASOPS, and one used delay-line pump-probe. Firstly, reflection mode ASOPS detection of pump-induced changes to polarisation angle change was performed on a CuMnAs film grown on a GaAs(001) substrate. This is followed by transmission mode measurements in ASOPS for CuMnAs samples grown on GaP(001). Finally, the reorientation of the Néel vector of a CuMnAs film in magnetic field was detected using delay line pump probe. Samples A, B, C and D, from Table 2.1, were used for these studies (20 nm CuMnAs on GaAs(001), 20 nm on GaP(001), 45 nm on GaP(001) and 50 nm on GaP(001) respectively). As described in the Table 2.1, the first three are uniaxial while Sample D is biaxial. Because Sample A is grown on GaAs, it is opaque to the chosen wavelengths and therefore cannot be used in transmission mode. In all cases, the changes in polarisation angle are measured as the change in amplitudes of

the polarisation components split by a Glan prism or Wollaston prism.

#### 4.4.1 Detecting Polarisation Angle Changes in Reflection

In order to confirm that it is possible to measure the demagnetisation-related changes to polarisation angle on a CuMnAs sample grown on GaAs(001), reflection mode ASOPS was performed on Sample A. Figure 4.9 represents the set-up used to detect polarisation changes in reflection mode ASOPS. The ND:YAG 532 nm CW pump lasers enable the Ti:Sapphire lasers to generate  $< 100$  fs pulses at 80 MHz in the 700–1080 nm range. The beams from both lasers are overlapped on the diode of the trigger detector to generate trigger signals when the pulses occur simultaneously. Both beams are incident on a spectrum analyser to monitor the wavelength and ensure that the lasers are pulsing. The SHG doubler converts the red light into blue light at half the input wavelength to be used as the pump beam which is focussed to  $\approx 10 \mu\text{m}$ . The first Glan prism acts as a polarisation filter, filtering the polarisation to be vertical. The following half-wave ( $\lambda/2$ ) plate is used to select the incident polarisation on the sample. The chopper is used to measure the DC amplitude from the split detector, for normalisation purposes. The microscope objective focuses the probe beam down to  $\approx 1 \mu\text{m}$ . The light reflected from the sample is in a confocal scheme and so an image can be extracted by intercepting the reflection with the sliding mirror to direct it into the microscope and camera. The first element in the detection block is a red-pass filter which eliminates any scattered light from the blue pump beam. Next the half-wave plate is used to select the polarisation incident on the second Glan prism. This Glan prism splits the probe beam into components with vertical and horizontal polarisation which are then fed into the split detector. By choosing the polarisation incident on this Glan prism, the intensity of the beams incident on the split detector can be balanced to yield zero signal in the steady state, only detecting changes

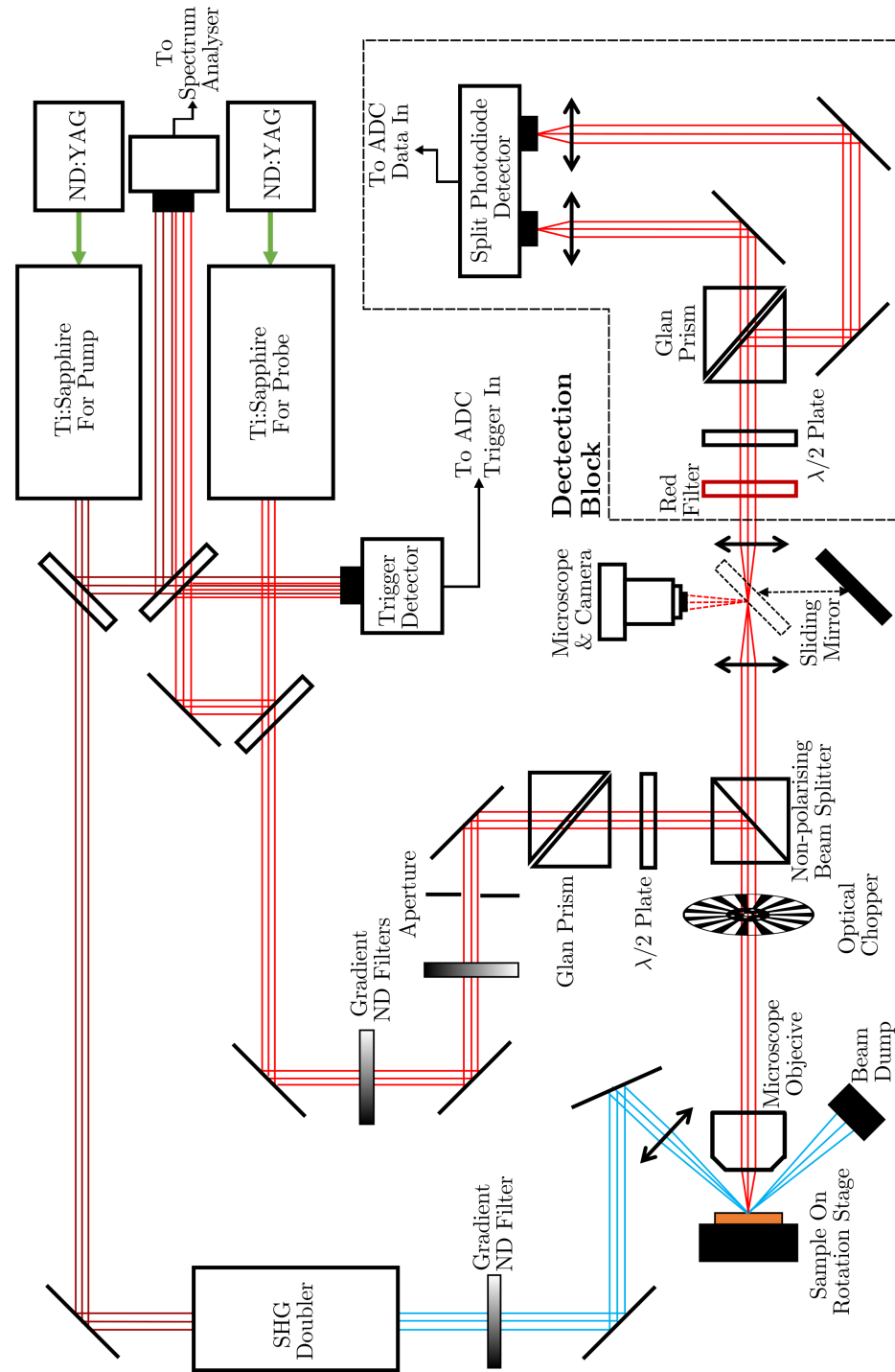


Figure 4.9: A schematic representation of the real space layout of the scheme used to measure linear polarisation changes in reflection mode ASOPS measurements. Double headed arrows represent lenses, black lines are mirrors and narrow black rectangles are beam splitters. All other optical elements are labelled. This needs the detection polarisation optics to be re-labelled and a dotted line around the detector scheme.

from the steady state polarisation.

For these ASOPS reflection measurements, the sample was mounted on a copper backplate. The alignment consists of three stages, first the sample aligned with its surface perpendicular to the incident probe beam, then the pump beam is focussed and overlap between the pump and probe beams is found, before the split detector is balanced. To align the sample, the microscope objective was removed and the sample was adjusted to reflect the probe beam back down the incident path. Then the microscope objective was returned, and the focus was set using the camera with the beam set to very low power. The pump beam alignment was done by first focussing it and overlapping the beams using the image from the camera, and then improved without the camera (because there is aberration in the camera optics), instead using the signal on the oscilloscope. To do this, the position of the pump was adjusted by blocking one input to the split detector, resulting in a measurement of the reflectivity change. The probe power was increased and the input polarisation was chosen, the pump beam temporarily blocked and the detection polarisation was set to balance the detector. The pump beam was unblocked, one input to the split detector was blocked and then the position of the pump beam was adjusted while looking at 10000 averages on the oscilloscope. The signal is obvious in less than a second and so small adjustments to the pump beam lens position were made, first to find overlap and then to maximise the amplitude of the signal. If the signal was poor, the focus could be adjusted iteratively and the overlap returned. To balance the split detector, both photodiodes are exposed to the probe beam. The polarisation incident on the sample was chosen, then the half wave plate in the detection block was adjusted until the voltage from the split detector was minimised. To preserve the sign of the observed signals, the changes to each of these half wave plates was done incrementally.

To perform a measurement, the input polarisation was selected, the split detector was balanced again and the DC magnitude of light was measured by blocking one input to the detector and running the chopper. Then the other

input was blocked and the sum of the two step wise changes in the DC values was used as the intensity value in calculating the polarisation rotation. The frequency difference was set and the PID control was enabled before an ASOPS measurement was conducted. The pump beam was opened and the intensity signal was measured (by blocking the negative input to the detector) and used to monitor alignment/overlap of the beams. Then the balanced scheme was measured with 100,000 or 1,000,000 averages. The Red Pitaya was set to measure these in blocks of 10,000 averages for each point, consisting of 1,250 traces where each point in time is the average of 8 points, binned in time to the centre of those points. The data is collected at a set frequency of 125 MHz and the frequency difference is known, so the measurement time can be calculated, where a measurement consisting of 100,000 averages can be collected in less than 1 hr. Periodic changes present in the room may introduce oscillatory signals in the measured traces and so the measurements were repeated with a different frequency difference in order to identify any signals which were not a result of optical effects. Typically, the frequency differences were 800 Hz and 600 Hz. This whole process is repeated for each desired input polarisation. An incident probe power of 1 mW and pump power in the order of 100 mW was typical for these experiments, measured between the beam splitter and the microscope objective. To measure the angle dependence, the input polarisation was changed in steps of 10° from  $-65^\circ$  to  $65^\circ$ , achieved by rotating the half-wave plate by 5° each time.

#### **4.4.2 Detecting Polarisation Angle Changes in Transmission**

Films of CuMnAs grown on GaP(001) can be measured in transmission mode more readily due to their higher transmittivity than their reflectivity. Therefore, ASOPS was demonstrated as capable of detecting the pump-induced demagnetisation-related changes to polarisation angle in transmission. For

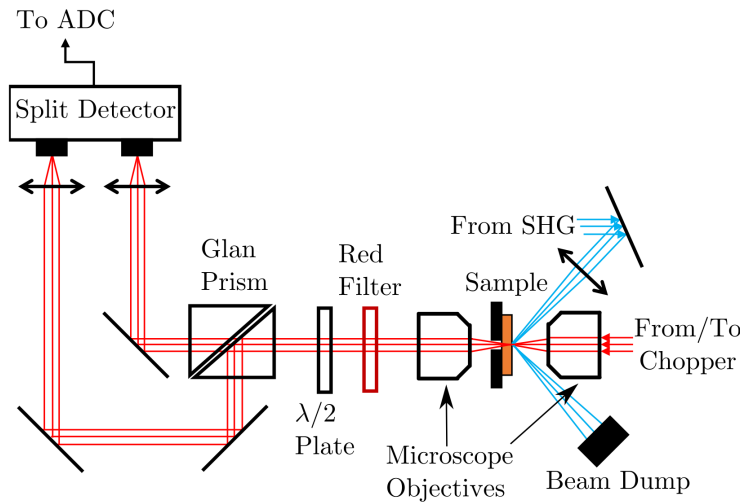


Figure 4.10: A schematic representation of the real space layout of the adjustments to convert the reflection mode scheme into a transmission mode scheme for measuring polarisation changes. This detection block replaces the detection block marked in Fig. 4.9. The dark red and blue lines are ray traces for the pump beam and the light red lines are ray traces for the probe beam. Double headed arrows represent lenses, black lines are mirrors. All other optical elements are labelled.

these studies, uniaxial Sample B and biaxial Sample D were used. The set-up for this is made by replacing some parts in Fig. 4.9 with the elements drawn in Fig. 4.10. The light reflected from the sample was returned through the beam splitter as before, and the confocal scheme required for the microscope view was maintained. The detection scheme was moved to the reverse of the sample and an additional microscope objective was required to refocus the probe beam after transmission. Otherwise, the scheme works as described previously. Alignment works much the same as before, with the overlap done first on the camera and then adjusted by maximising the transmissivity signal on the oscilloscope (by blocking one diode of the split detector). The wavelengths, powers and spot sizes were comparable to before as well.

#### 4.4.3 Detecting Spin Flop in Transmission

To measure the sample undergoing spin flop, Sample C taken to TU Dortmund, Germany. The sample was placed in a cryostat between the poles of a superconducting magnet with optical access windows. A magnetic field,

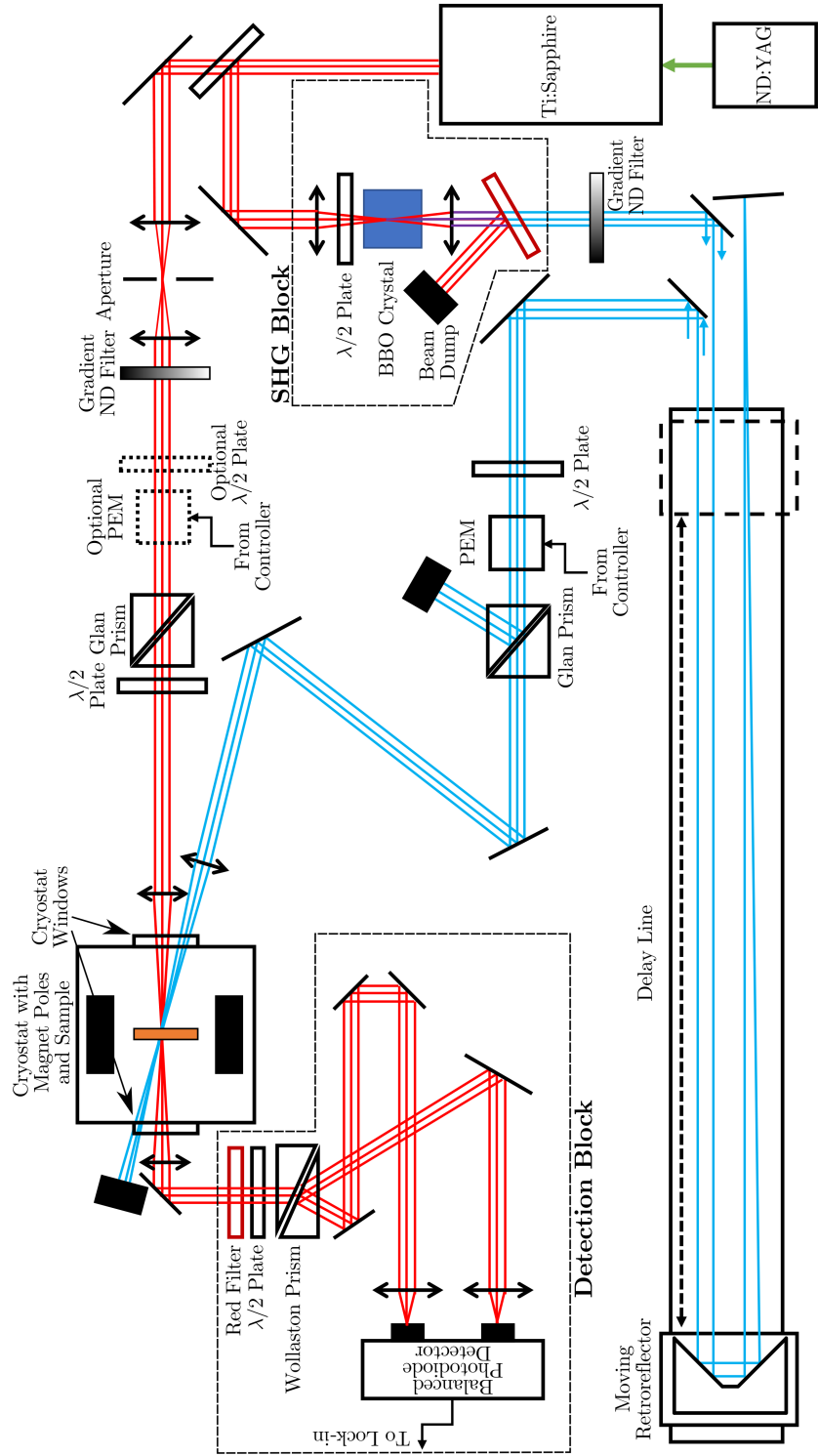


Figure 4.11: A schematic representation of the real space layout of the scheme used to measured polarisation changes in transmission mode delay-line measurements. Red and Blue lines are ray-traces of the probe and pump beams respectively. Double headed arrows represent lenses, black lines are mirrors and narrow black rectangles are beam splitters. All other optical elements are labelled. The optional elements were used to increase the reference frequency for the lock-in amplifier but are not always used or necessary. re-label the polarisation optics here too.

$H$ , was applied along the easy axis and hard axis of the Sample C in two separate measurements. Figure 4.11 illustrates the set-up for the transmission measurement of the demagnetisation-related polarisation angle changes in such a cryostat using the transmission mode Voigt geometry from Fig. 4.1(b). In order to fit the sample between the poles of the magnet, the sample is mounted on the end of a probe, glued to a piece of stiff card, and the measurements were repeated to have the sample in two orientations, one with the field applied along the easy axis and one perpendicular to the easy axis. The sample temperature was heated to 250 K from the  $\approx 4$  K base temperature, bringing the sample closer to the Néel temperature and allowing the pump pulse to demagnetise the sample more readily. The red line represents the probe beam at 815 nm and the blue line represents the pump beam at 407 nm. The PEM acts as an oscillating half-wave plate which, when incident on the Glan prism, generates an oscillating intensity. The PEM oscillates at  $\approx 20$  kHz and the controller has output which was used as the reference signal in a lock-in amplifier. The probe beam was aligned to be as perpendicular to the sample surface as possible to remove aberration and refraction for the transmitted beam. The Wollaston prism split an arbitrarily polarised beam into its vertically and horizontally polarised components. By choosing the angle of the half-wave plate before the Wollaston prism, the intensities of each beam can be equalised resulting in zero voltage on the balanced photodiodes. When the pump beam is then introduced, any changes from the steady state are detected as small changes without saturating the amplifiers in the detector.

The delay-line has a large range so the first step after changing the sample is to find the position corresponding to coincident beams. To do this, first, an approximate overlap is made and then a long scan, with the negative diode of the detector blocked to measure transmissivity, is performed to find the temporal overlap. This often has to be repeated several times to find a starting point for overlap because, if there is no signal, it is not possible to see the start of the signal. Once the temporal overlap is achieved, rapid short scans are

made and iterative adjustments of the pump beam are performed to maximise the transmissivity change signal. After finding temporal and spatial overlap, the scans of a suitable duration and precision can be performed. In these studies, the stage was moved in steps of 1 mm for a total range of 400 mm corresponding to a precision of  $\approx 67$  ps and a total time of  $\approx 3.5$  ns, calculated using the speed of light and path length change (four times the position change, due to doubling back in the delay-line). The lock-in integration time was set to 0.2 s and each resulting trace is the mean of 10 traces. The blue light is generated through two photon absorption in a BBO crystal with a specific incident polarisation and precise positioning of the focal point. This frequency doubling effect of SHG leads to a halving of the wavelength and a loss in power, yielding a pump power of  $\leq 1$  W. The probe beam is set with a fixed path length and the pump beam is passed through delay-lines to adjust the relative arrival time between pulses.

The measurement process for polarisation signals is similar to in ASOPS, whereby the DC intensity can be measured using the PEM incident on a Glan prism (optional components) in the probe beam path and blocking each input to the detector in turn. The input polarisation is set and the detector is balanced as described previously. The scans are performed with the magnetic field set to 0 T first and then the field is set to 4.5T before the same scan is performed with no adjustment to the scheme, and then another zero field measurement is performed for confirmation. The sample was removed, reoriented and replaced before repeating this process.

#### 4.4.4 Data Handling

The traces measured in these studies have their time values adjusted such that the coincidence of the pump and probe pulse occurs at a time value of zero. There is some small period of measurement before this time which is used to adjust the voltage signal zero point, and to visualise any slope on the

signals. The time after the coincidence contains the detected signals which can be analysed or inspected. For the ASOPS measurements the duration of the region before coincidence is determined by the path length difference between the trigger path and the probe beam path to the detector. For the delay-line schemes, the delay-line starting point can be selected to give an appropriate starting time. The traces measured in ASOPS contain bumps at the start of all traces which are due to coupling between the cable carrying the trigger signal and the cable carrying the signals from the split detector. These bumps are erroneous but occur far before the coincidence point and can therefore be ignored.

The change in polarisation angle can be calculated from the split detector voltage using

$$\delta\varepsilon \approx \frac{\Delta V}{\sqrt{2}V_0} \quad (4.9)$$

where  $\Delta V = |V_+| - |V_-|$  is the voltage trace measured from the balanced output of the split detector,  $V_0$  is the steady state DC voltage amplitude on each diode in the absence of pump pulses and  $|V_+|$  and  $|V_-|$  are the voltages on the positive and negative diode, respectively. To determine this dependence, consider light equally split on each diode (polarisation incident on the Glan or Wollaston prism with an angle of  $\beta = \pi/4$  measured from the fast axis) such that the split detector is balanced. If  $I_0$  is half the total intensity, the intensities of the outputs from the prism are given by  $I_+ = I_0 \cos(\beta)$  and  $I_- = I_0 \sin(\beta)$  for beams incident on the positive and negative diodes respectively. A change of  $\delta\varepsilon$  causes a change in voltage measured by each diode given by  $|V_+| = V_0 \cos(\pi/4 + \delta\varepsilon)$  and  $|V_-| = V_0 \sin(\pi/4 + \delta\varepsilon)$ , assuming the measured change is linear with intensity ( $V \propto I$ ). The total voltage is the difference in these magnitudes

$$\Delta V = V_0 \cos(\pi/4 + \delta\varepsilon) - V_0 \sin(\pi/4 + \delta\varepsilon)$$

$$\Delta V = \sqrt{2}V_0 \sin(-\pi/4 + \pi/4 + \delta\varepsilon)$$

$$\Delta V = \sqrt{2}V_0 \sin(\delta\varepsilon).$$

After making  $\delta\varepsilon$  the subject this becomes

$$\sin(\delta\varepsilon) = \frac{\Delta V}{\sqrt{2}V_0}$$

and using a small angle approximation  $\sin(\delta\varepsilon) \rightarrow \delta\varepsilon$  giving Eq. 4.9.

## 4.5 Results

The following section demonstrates and provides insight into the results from the above described methods, starting with the ASOPS experiments. The first results are traces measured in reflection, including a study of the changes dependence on the input polarisation angle. This is followed by the confirmation of transmission mode in ASOPS and then spin-flop is detected using delay-line pump probe in the transmission scheme. The detected magneto-optical signals are a measurement of the extent of change in linear polarisation angle that is a result of the pump-induced demagnetisation. These changes are a deviation from the steady state polarisation rotation induced by the Voigt effect, and are caused by the heat delivered by the pump pulses which leads to (partial) demagnetisation by raising the sample close to (or above) the Néel temperature.

### 4.5.1 Voigt Effect Changes Observed in Reflection Pump-Probe

Figure 4.12 contains example traces for measurements using Sample A, a 20 nm CuMnAs film on GaAs(001), in reflection mode ASOPS. The data was collected using the setup illustrated in Fig. 4.6 with the expected polarisation changes illustrated in Fig. 4.9. Figure 4.12(a) Shows the magneto-optical signals for three incident polarisation angles,  $\varepsilon$ , of  $+45^\circ$ ,  $0^\circ$  and  $-45^\circ$ , measured relative to the Néel vector (which is assumed to be along the [010] uniaxial easy axis), in red, cyan and blue lines respectively. (b) Shows an example reflectivity change measured with an incident polarisation at an angle of  $-45^\circ$  to the Néel vector.

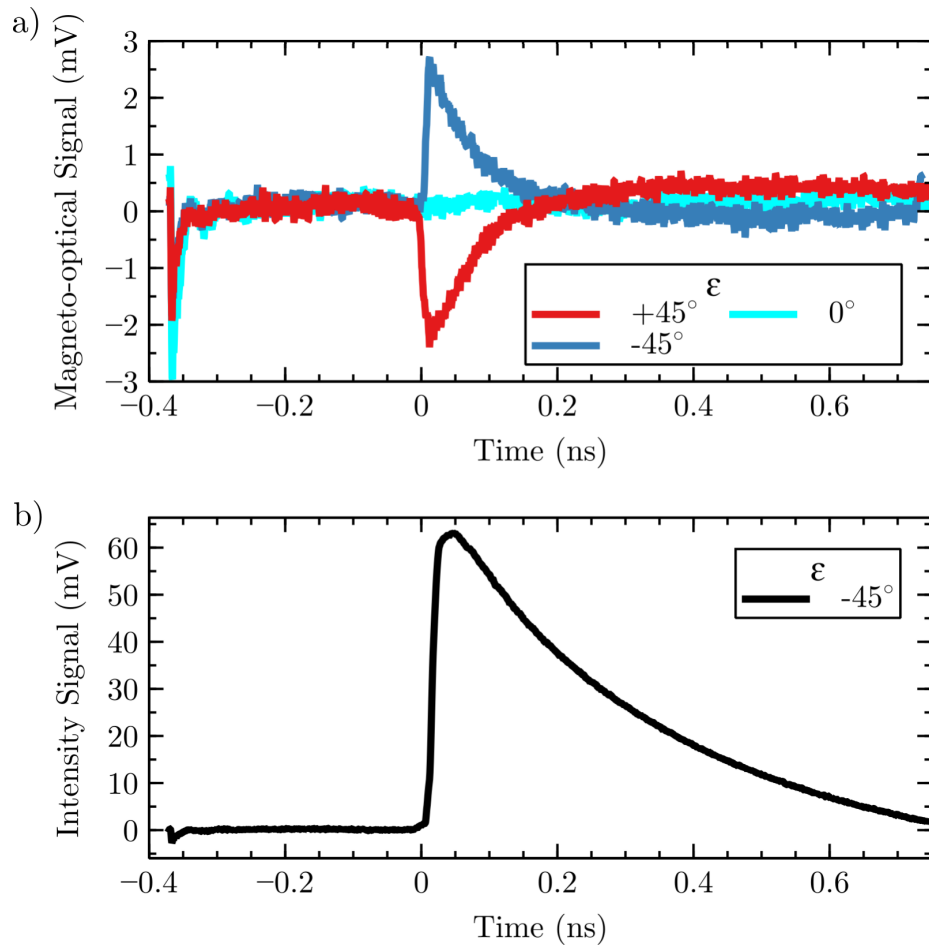


Figure 4.12: Plots of example reflection mode ASOPS traces measured using Sample A of (a) polarisation signals with the detector in balanced mode with the angle between the Néel vector and linear polarisation axis of  $+45^\circ$ ,  $0^\circ$  and  $-45^\circ$  in red, cyan and blue lines respectively. (b) shows the reflectivity change measured by blocking the negative input to the split detector at  $-45^\circ$  relative polarisation. These results were measured using Sample A with 1 mW probe power at 780 nm and a slightly de-focussed 100 mW pump beam at 345 nm.

The reflectivity trace in (b) shows a sharp rise in reflectivity followed by an exponential decay back to the steady state within 1 ns. This follows the expected behaviour associated with electronic relaxation and thermal effects [64]. The magneto-optical signals in (a) have a similar shape but are much smaller and the signals decay more rapidly. The three amplitudes follow the predicted behaviour described by the  $\sin(2\epsilon)$  dependence. The  $+45^\circ$  (red) and  $-45^\circ$  (blue) signals have very similar shapes and show a clear change in sign, while the  $0^\circ$  trace is almost perfectly flat, showing no change in polarisation, indicating that the signals are not some remnants of the intensity signal or due to poor balancing.

Figure 4.13 shows a plot of the rising peak height of magneto-optical signals as a function of relative polarisation,  $\epsilon$ , measured in reflection mode ASOPS. In (a), the red line with circles shows the measured data for the magneto-optical peak heights and the smooth blue line shows a  $\sin(2\epsilon)$  prediction with amplitude set to match the largest signal measured. In (b) the relative reflectivity intensity change signals are plotted (black diamonds), corresponding to the right hand axis, which shows a significant variance in amplitude of the reflectivity change. The incident probe beam power was adjusted such that the reflected beam had the same power for each measurement. This was done to account for variations caused by moving the polariser. Despite the  $\approx 30\%$  changes in intensity signal, the  $\sin(2\epsilon)$  dependence is clearly illustrated in (a) and the change in sign occurs when the polarisation is rotated through the angle parallel to the sample Néel vector, as expected.

The above results have demonstrated that there is a rotation change in reflection mode for CuMnAs films grown on GaAs(001) substrates. The resulting signals were shown to have a dependence on the angle between the incident polarisation axis and the Néel vector,  $\epsilon$ , which obeys the expected  $\sin(2\epsilon)$  dependence. Therefore the uniaxial nature of a CuMnAs film can be confirmed rapidly using ASOPS to find the incident polarisation which gives maximum signal.

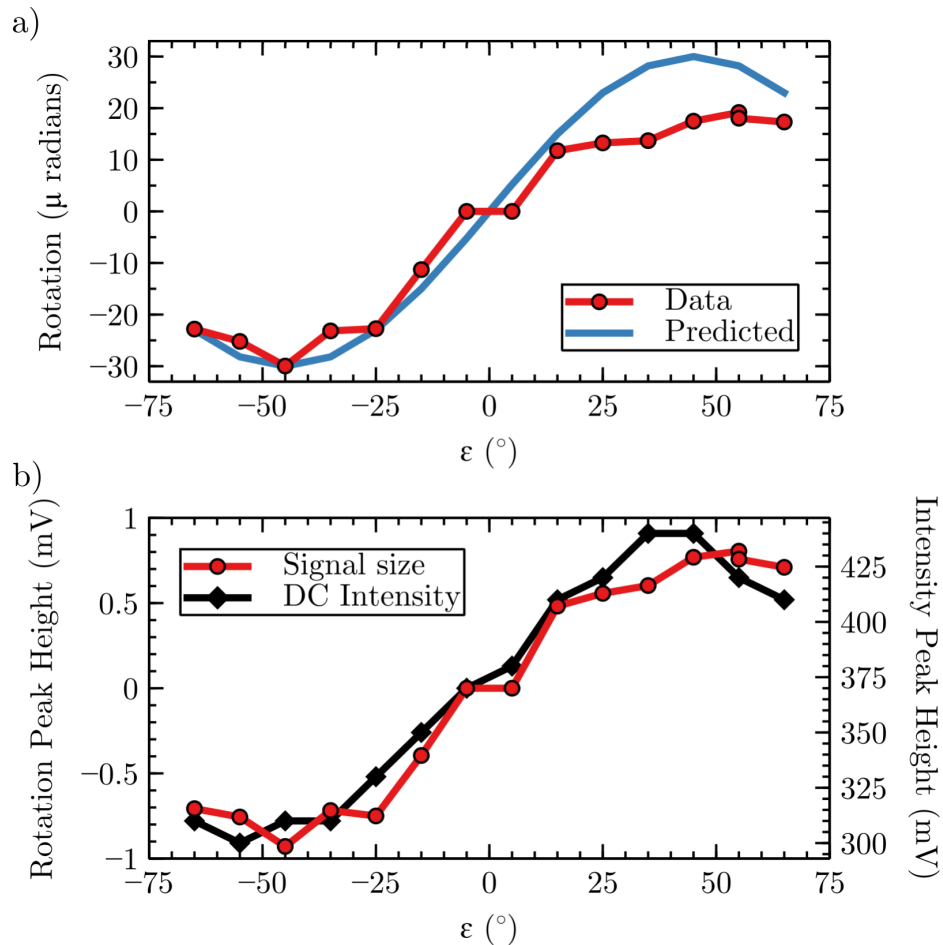


Figure 4.13: Plots of the angle dependence of (a) polarisation changes (red circles) and a reference sinusoid (blue line) and (b) polarisation changes (red circles, left axis) and reflectivity changes (black diamonds, right axis). Measured using Sample A with 1 mW probe power at 780 nm and a slightly de-focussed 100 mW pump beam at 345 nm.

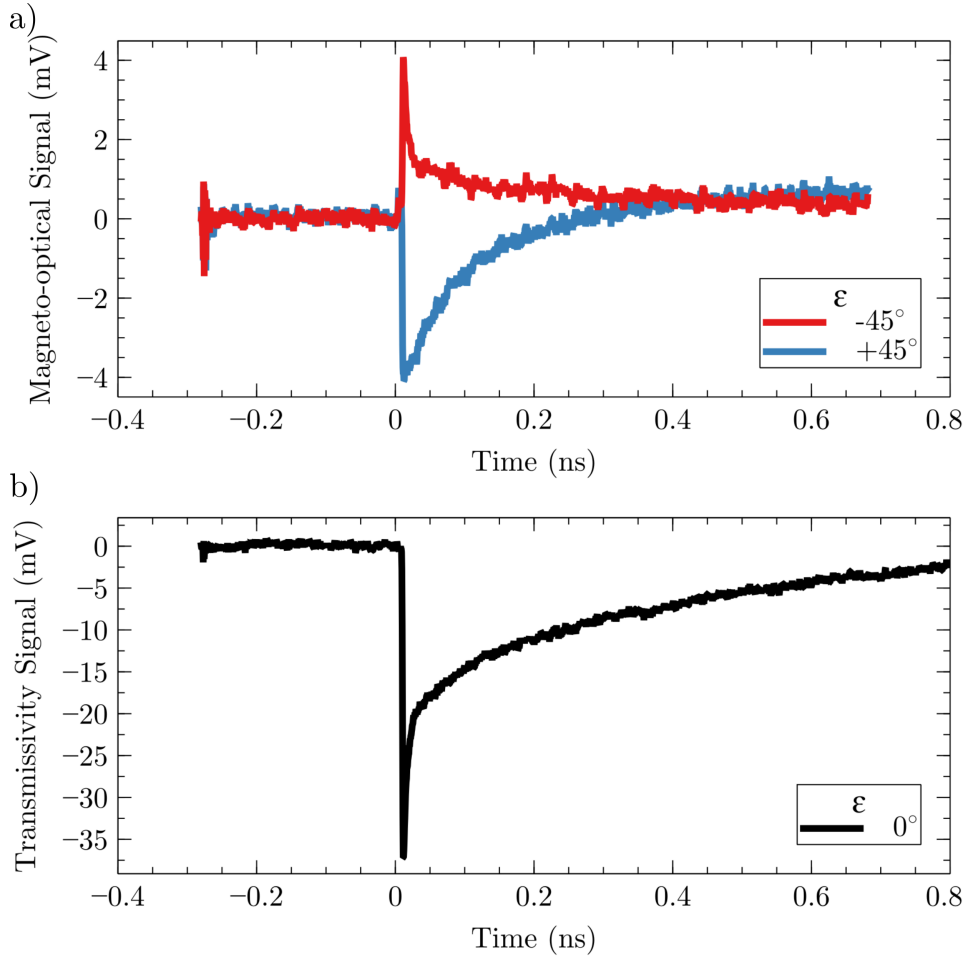


Figure 4.14: Plots of traces measured in the reflectivity mode using Sample B. (a) shows the polarisation signals with the detector in balanced mode and (b) shows the transmissivity signal with the negative input to the detector blocked. An approx 1 mW probe beam at 755 nm and the 50 mW pump beam at 380 nm were used to collect these data.

#### 4.5.2 Voigt Effect Changes Observed in Transmission Pump-Probe

Figure 4.14 contains traces for Sample B, a 20 nm CuMnAs film on GaP(001), measured in transmission in ASOPS using the setup adjustments in Fig. 4.10 following the polarisation changes shown in Fig. 4.7. Figure 4.14(a) shows the traces for relative polarisations of  $\epsilon = +45^\circ$  and  $-45^\circ$  relative to the Néel vector in red and blue respectively. (b) shows the trace for the transmissivity change induced by the pump beam measured with a relative polarisation of  $0^\circ$ . The shape and amplitude of the two signals is not as similar as for the

reflection measurements. The  $-45^\circ$  trace drops off more suddenly directly after the pulse than for the  $+45^\circ$ . It is also of note that the signs of the signals are reversed compared to the reflection measurements. This is because the positive and negative diodes in the split detector are used to the opposite outputs from the Glan prism when compared to the reflection mode measurements.

Here, the transmittivity decreases as a result of the pump pulse heating, shown in Fig. 4.12(b). For these data, the probe power was set such that each diode on the split detector measured 1.4 V (approx 1 mW average power as before) at 755 nm and the pump was set to 50 mW at 380 nm before the lens by the sample. The lower wavelengths and power are due to poor alignment in both the laser cavities and SHG doubler, despite attempts to improve them. This did not seem to drastically effect the results.

The traces from the measurements of Sample D, a biaxial 50 nm CuMnAs film grown on GaP(001), are not shown here. The transmittivity changes were similar to those found in the uniaxial sample measured this way, however this sample yielded no demagnetisation polarisation change signals for incident polarisation angles of  $-45^\circ$ ,  $0^\circ$  and  $45^\circ$ , measured relative to the [110] easy axis of this sample. Apparently, this is because the domains were smaller than the spot size, and so the lack of signal suggests that the population of domains was close to even. This means that the sample was identified as biaxial through this measurement, in agreement with other measurements of the anisotropy of this sample (XMLD-PEEM images and transport measurements).

The magneto-optical signal is shown to change in sign when the angle between the Néel vector and the incident polarisation is changed from  $-45^\circ$  to  $+45^\circ$ . The use of ASOPS to detect the predominant Néel vector of the uniaxial sample, and lack of polarisation change signals in the biaxial sample, demonstrates ASOPS as technique capable of rapid determination of the uniaxial nature of CuMnAs films grown on GaP(001) substrates.

### 4.5.3 Spin Flop Detection Using Linear Polarisation Angle Changes in Transmission Mode

Figure 4.15 summarises the detection of spin flop was conducted using Sample C, a 45 nm CuMnAs film on GaP(001), to observe the decrease in the Voigt effect as a result demagnetisation through the heating from a pump pulse. The sample was placed in a cryostat between the poles of a superconducting magnet and delay-line pump probe was used, following the scheme in Fig. 4.11 and the expected polarisation changes are illustrated in Fig. 4.8. Due to the distance between the cryostat windows and the sample, the spot size in these measurements is larger than in ASOPS, at  $> 50 \mu\text{m}$ . The sample was kept at 250 K and the field was set to 0 T, 4.5 T and then 0 T again. The sample used had a chip in one corner as the only identifying feature, and the sample was mounted to apply the field in two sample directions as shown in Figure 4.15(a) and (b), with CuMnAs crystal axes and beam polarisation axes marked for clarity. (c) and (e) correspond to the orientation in (a) for input polarisations of  $\varepsilon = +45^\circ$  and  $-45^\circ$  respectively. (d) and (f) contain traces for input polarisations of  $+45^\circ$  and  $-45^\circ$  respectively with the sample in the orientation from (b). Omitted are the intensity signals which resemble the data in Fig. 4.14(b) and traces at  $0^\circ$  in which there was no magnetooptical signal.

The traces presented in (d) closely resemble the predicted behaviour for a sample with biaxial anisotropy and domain sizes smaller than the spot size. Before applying the field, there is no MO signal change caused by the pump pulse and above the spin flop field, a positive change in MO signal is detected. This suggests that the applied field increases the proportion of moments perpendicular to the applied field, and therefore spin flop is detected. Similarly, in (f), the zero field case shows a small negative MO signal which is increased under an applied field. This suggests that the proportion of moments is once again changes and indicates spin flop. In (c,e), the application of field slightly suppresses the signal which can be explained by taking into account

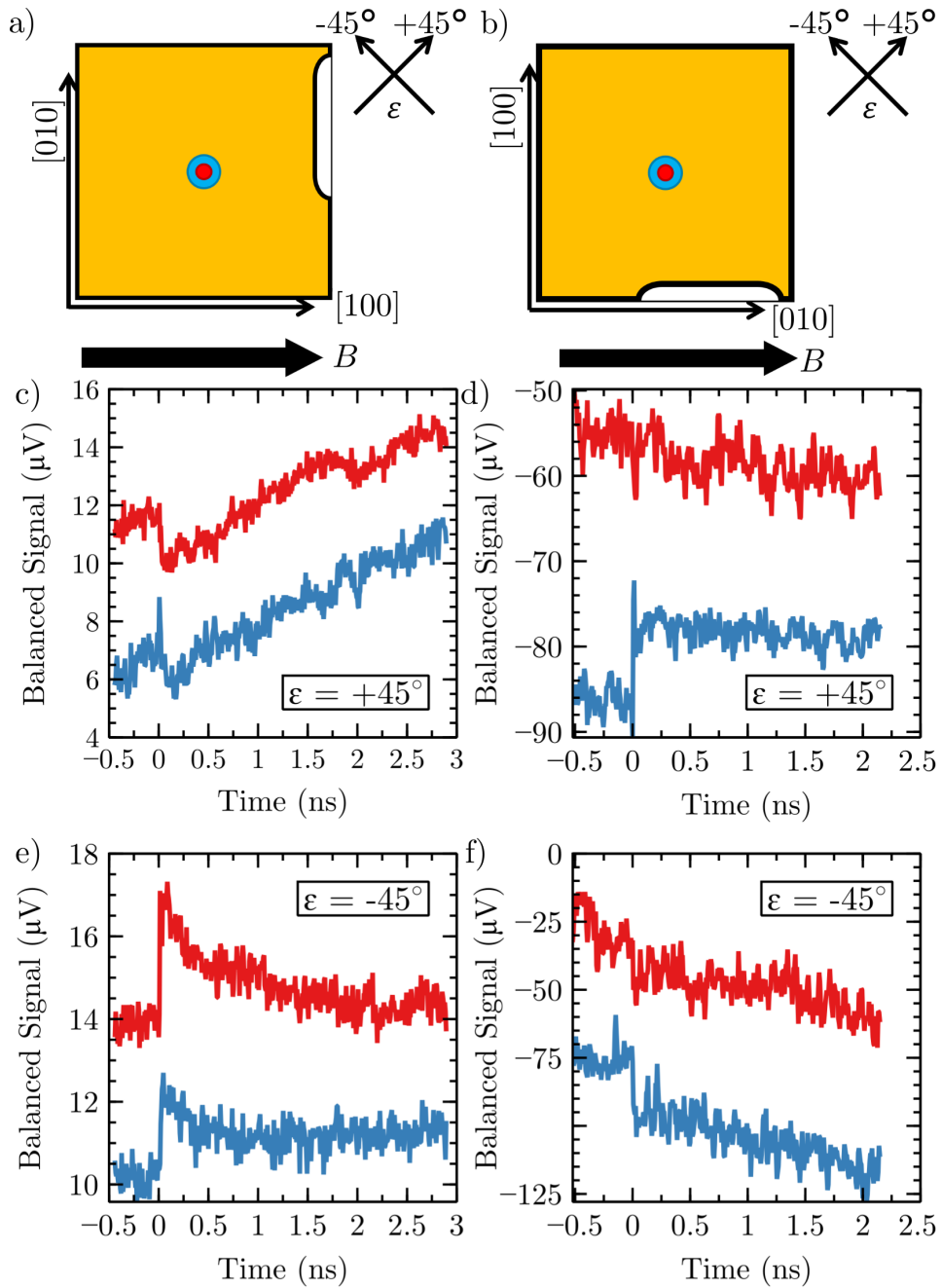


Figure 4.15: Plots to summarise the results detecting spin flop in transmission mode using delay-line pump-probe. (a) and (b) demonstrate the geometry used for the plots below them ((c,e) and (d,f) respectively) where the missing chip was used as reference in mounting the sample. The plots in (c-f) contain traces for the measurements before the field was applied (red) and with a 4.5 T magnetic field applied (blue). (c) and (d) used  $+45^\circ$  relative polarisation and (d) and (f) used  $-45^\circ$ .

inhomogeneity of the sample. In the measured spot, the sample may have a dominant uniaxial component which is parallel to the field, so at zero field the signal is detected. When the field is increased, some moments in the measured region may rotate to be perpendicular to the field and therefore the sample becomes more biaxial.

Regardless of the reason for the small signals and biaxial nature of the sample, the change in Néel vector was detected and spin flop was observed when the a magnetic field was applied along the uniaxial easy axis of Sample C with field strength above the spin flop field. When the magnetic field was applied along the [100] hard axis of the sample, the MO signal was partially suppressed by the field, showing a change in domain populations.

## 4.6 Conclusions

In summary, ASOPS was demonstrated as a rapid tool for the characterisation of the anisotropy of CuMnAs, discerning between uniaxial and biaxial anisotropies in a matter of hours, without the need for cryogens, high magnetic fields or facility time. This was done by detecting changes in polarisation angle that are caused by the reduction in the Voigt effect when the sample was heated by a pump pulse, thus (partially) demagnetising the sample. The results showed that the change in polarisation angle can be detected in transmission and reflection geometries for CuMnAs samples grown on GaP(001) and in reflection mode for samples grown on GaAs(001) substrates. A transmission mode delay line technique was used to measure the rotation of the Néel vector as a result of spin flop by applying a 4.5 T magnetic field along the easy axis of a uniaxial CuMnAs sample. Spin flop was identified, showing behaviour suggesting a biaxial nature for one measured region and uniaxial behaviour in another. Applying a large magnetic field acted to increase the population of one of the orientations and thus increasing the measured polarisation angle change in the biaxial region and decreasing these changes in the uniaxial region.

# **Chapter 5**

## **Optical Determination of CuMnAs Elastic Constants using Strain Pulse Phonon Reflection**

### **5.1 Introduction**

The origins of the domain structures presented in Section 2.4 are not fully understood. Simulation works aiming to explore the interplay or magnetostriction and domain populations require understanding of the elastic behaviour of CuMnAs [65]. To this end, the studies contained in this chapter aim to experimentally determine some of the elastic constants of CuMnAs for use in such simulations. Before the investigation detailed below, none of the elastic constants of CuMnAs had been experimentally measured. Here, a pump-probe optical technique was used to measure the round trip time of strain pulses in layers of CuMnAs and analysis of elasticity equations were combined to determine four of the six unique elastic constants for CuMnAs in order to aid the progression magnetostriction studies in CuMnAs.

There are a few methods for determining the elastic constants of thin film crystalline media. There are robust methods which comprise the generation and detection of surface acoustic waves (SAWs) which enable the measurement

of various modes of phonon oscillation in the crystals. Complex analysis of the resulting spectra is capable of high precision acquisition of the elastic constants and other stress related parameters [66]. The production of the necessary gratings used in SAWs is costly, in time and money, and was not justifiable for us. Nanoindenters are also capable of determining the elastic constants but these are also prohibitively expensive [67]. Instead, a technique requiring very few changes to already existing optical measurement schemes was used to measure some of the elastic constants of CuMnAs by generating a strain pulse that is reflected from the sample-substrate interface of epitaxially grown CuMnAs films. The speeds of sound for the generated modes of oscillation can then be calculated using the round trip time and the round trip distance [64]. The resulting speeds can be used to evaluate the elastic constants after some analysis of linear elasticity equations.

This chapter details the measurement of four of the six unique elastic constants, namely  $c_{11}$ ,  $c_{33}$ ,  $c_{44}$  and  $c_{13}$  for CuMnAs using asynchronous optical sampling (ASOPS) to generate and detect strain pulses in CuMnAs samples grown in three orientations. First, the growth orientations are described before the general principles of strain pulses and the aforementioned linear elasticity analysis are detailed. The experimental principles and methods are described before the results and final evaluation of the elastic constants is performed. The chapter concludes with a summary of the experimental results. The optical elements used are previously described in Section 4.1.

### 5.1.1 Sample Information

Samples F, G and H are three layers of CuMnAs grown at a thickness of  $\approx 230$  nm on three different substrates. Sample F was grown on a GaP(001) substrate with the CuMnAs[001] direction perpendicular to the substrate surface as illustrated in Fig. 5.1(a), which is the usual growth regime for CuMnAs samples. Samples G and G were grown on high-index GaAs substrates,

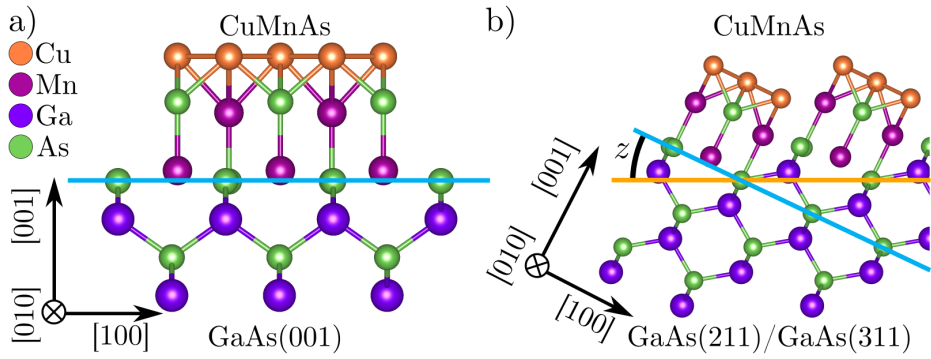


Figure 5.1: Ball and stick models illustrating the growth of CuMnAs on substrates of (a) GaAs(001) and (b) high index GaAs(112B)/(113). In both models, the axes labels correspond to the CuMnAs axes, the blue line represents an exposed GaAs(001) facet onto which the CuMnAs grows. The orange line in b) represents the (112)/(113) planes which are parallel to the surface normal of the wafer. This illustration does not account for the width of growth facets or the expected surface reconstruction which occurs in real systems. The label  $z$  represents the angle of the CuMnAs[001] axis relative to the surface normal and the angle to which the CuMnAs[100] axis points out of the surface plane.

specifically GaAs(113) for Sample G and GaAs(112) for Sample H. These two samples grew such that the CuMnAs[001] direction was tilted at angle  $z$  to the substrate surface with the CuMnAs(001) plane parallel to the GaAs(001) facets, as illustrated in Fig. 5.1(b). The angles were calculated from geometry for Sample G and Sample H as  $z_G = 3/\sqrt{11} = 25.25^\circ$  and  $z_H = 2/\sqrt{6} = 35.26^\circ$  respectively. Here, the CuMnAs[100] or the CuMnAs[010] axis can be defined as the axis that lies in the surface plane, and the other than points out of plane at the angle  $z$  to the surface plane. In this chapter, the choice has been made to specify that the CuMnAs[010] axis is in the plane of the surface and the CuMnAs[100] axis points out of the surface plane, but both configurations are equivalent due to symmetry. The high-index substrates were used to facilitate three different directions of propagation through the material. The two samples grown on high index substrates allow for excitation of additional acoustic modes which incorporate more elastic constants than the GaP(001) or GaAs(001) layers allow on their own; how this happens will be explained in more detail below.

## 5.2 Methods

The speed of sound in each material was measured using ASOPS. The pump pulse was set to a wavelength of 382.5 nm and the probe beam was at 765 nm. The ASOPS reflection setup is illustrated in Fig. 5.2, which is the polarisation detection reflection scheme from Fig. 4.9 with all the polarisation optics removed and no compensation on the split detector. The reflectivity of the sample surface changes when stressed as a result of elasto-optical effects and so the strain pulse echoes generated by the heating pump pulse are detected as changes in the intensity of the reflected light [64].

The samples were mounted on a copper disc which was held by a mirror holder such that precise alignment could be conducted. Each sample was measured for one million repeats (with a decimation factor of 8 for each point) and the measurement was conducted using two repetition rate differences for each sample, 800 Hz and 600 Hz specifically, between the pump laser and the probe laser. This is done to identify any oscillations present in the signal which do not correspond to reflectivity changes in the sample. The resulting traces were then plotted and the time difference,  $t$ , was found by measuring the time between the peak of the initial rise from the pump pulse and the mid-point of the reflected strain pulses. The distance travelled,  $2d$  is double the film thickness, and the speeds,  $v$  were calculated using  $v = 2d/t$ . The first bump is always the longitudinal acoustic mode, by convention, and therefore is labelled  $v_{LA}$  where the next two, in time order, will be the fast transverse acoustic  $v_{FTA}$  and then the slow transverse acoustic  $v_{STA}$  by convention. The speed values can be put into the equations derived in Section 5.3 (Eqs. 5.17, 5.25 and 5.30) to evaluate the appropriate constants.

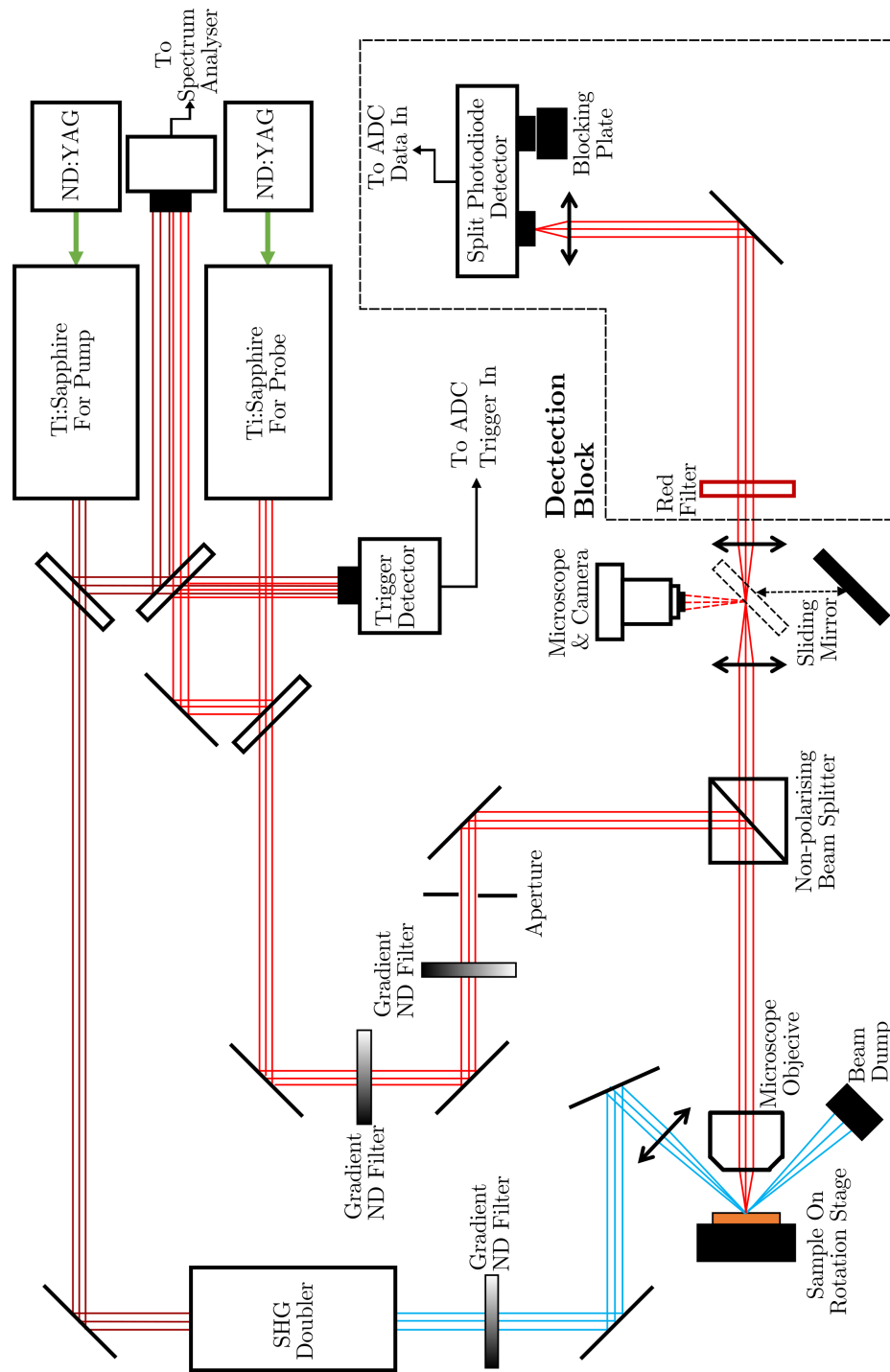


Figure 5.2: A schematic representation of the real space layout of the scheme used to measure round trip times of strain pulses reflected off of the substrate of a CuMnAs sample using reflection mode ASOPS. Double headed arrows represent lenses, black lines are mirrors and narrow black rectangles are beam splitters. All other optical elements are labelled.

## 5.3 Strain Pulses and Elastic Stiffness Coefficients

In ASOPS, two lasers are used such that a pump pulse is used to induce change in the material and a probe pulse is used to observe the changes (see Section 4.3.2). In this case, the pump pulse is incident on the free CuMnAs surface and acts to induce heating at the surface of the material which generates stress and consequent strain [64]. Because the laser spot sizes ( $\sim 5 \mu\text{m}$ ) used are much larger than the thickness of the film ( $\approx 230 \text{ nm}$ ), this strain pulse propagates away from surface and travels into the bulk material as an acoustic wave packet with a planar wavefront. Except in high symmetry propagation directions, this excitation results in up to three allowed modes of oscillation: a longitudinal acoustic mode (the fastest), a fast transverse mode and a slow transverse mode (taken as the slower transverse mode by convention) [68]. All three of these modes travel through the material until they reach an interface, such as the substrate-CuMnAs interface, at which point their waves are partially reflected. Figure 5.3 illustrates the propagation of the wave packets including the reflected echo and the component of the pulse transmitted into the substrate. The reflected strain pulses can then be detected at the surface by the probe pulses, as a change in the reflectivity or transmittivity of the material through elasto-optical effects [64]. The time difference between the pump pulse and when the echo is detected is used as the round trip time and thus the sound velocity of each acoustic mode can be measured as  $v = 2d/t$ .

In order to extract the elastic constants from generation and detection of strain pulses, it is necessary to understand what elastic constants are and how they determine the speed of sound of pulses travelling through a crystalline material.

Elastic stiffness coefficients are the collection of values which describe how a material resists deformation when subjected to a force. In a one-dimensional system, such as a wire, only one stiffness coefficient is required to describe the

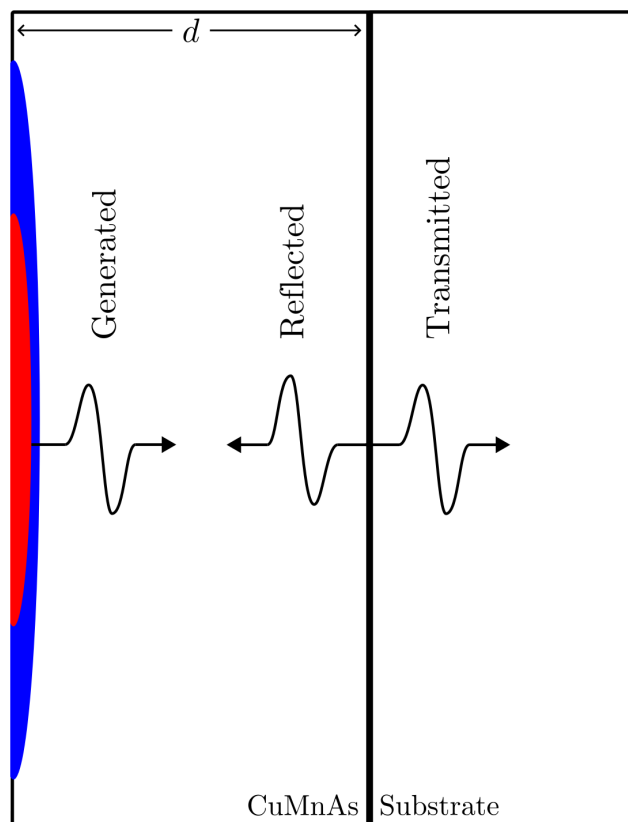


Figure 5.3: Illustration of strain pulse propagation in a CuMnAs layer after a pump pulse (blue dot) is incident on the surface. The probe pulse (red) then observes the same spot such that the reflected pulse echo is detected at a time  $\Delta t = 2d/v$  after the pump pulse.

Table 5.1: A table describing the pairings of  $ij$  and  $kl$  used to reduce the elasticity tensor from  $c_{ijkl}$  to  $c_{ij}$  where  $ij \rightarrow i$  and  $jk \rightarrow j$

$11 \rightarrow 1;$	$23 = 32 \rightarrow 4$
$22 \rightarrow 2;$	$13 = 31 \rightarrow 5$
$33 \rightarrow 3;$	$12 = 21 \rightarrow 6$

stretching of the wire under tension, and this coefficient is the Young's modulus,  $E$ . The Young's modulus is defined as the ratio of stress (applied force),  $\sigma$ , to strain (resulting relative change in length),  $\epsilon$ :  $E = \sigma/\epsilon$ . To generalise this to any given system, the elastic response to an arbitrary force in any number of dimensions requires a stiffness tensor,  $\underline{\underline{C}}$ , to describe the relationship between a stress  $\underline{\sigma}$  and the resulting strain,  $\underline{\epsilon}$ . This is given by Hooke's law:

$$\underline{\sigma} = \underline{\underline{C}} \underline{\epsilon} \quad (5.1)$$

which in three dimensions has the indices  $i, j, k, l = 1, 2, 3$ , having cartesian coordinates

$$\underline{x} = \begin{pmatrix} x_1 \\ x_2 \\ x_3 \end{pmatrix}. \quad (5.2)$$

The resulting elements of Eq. 5.1 are then

$$\sigma_{ij} = c_{ijkl}\epsilon_{kl} \quad (5.3)$$

where  $c_{ijkl}$  can be reduced to up to 21 unique elements by realising that many of the elements of the elastic tensor are equivalent, through the requirement for symmetry [69]. Specifically, the following elements must be equal

$$c_{ijkl} = c_{jikl} = c_{ijlk} = c_{jikl} = c_{klij} = c_{lkij} = c_{klji} = c_{lkji}. \quad (5.4)$$

A change in notation is often used at this stage to reduce the tensor from four dimensions to two dimensions by combining pairs of  $ij$  and  $kl$  according

to the equivalence table in Table 5.1. At this stage, the elasticity tensor is

$$\underline{\underline{C}} = \begin{bmatrix} c_{11} & c_{12} & c_{13} & c_{14} & c_{15} & c_{16} \\ c_{12} & c_{22} & c_{23} & c_{24} & c_{25} & c_{26} \\ c_{13} & c_{23} & c_{33} & c_{34} & c_{35} & c_{36} \\ c_{14} & c_{24} & c_{34} & c_{44} & c_{45} & c_{46} \\ c_{15} & c_{25} & c_{35} & c_{45} & c_{55} & c_{56} \\ c_{16} & c_{26} & c_{36} & c_{46} & c_{56} & c_{66} \end{bmatrix} \quad (5.5)$$

and is a symmetric matrix. For any given crystal unit cell, this matrix can further be reduced by considering the symmetry of the crystal. The results are documented and are the same for any crystal with a given point group. To understand this, it is typically suggested to consider a cubic crystal. In a cubic crystal, the high symmetry leads to any rotation around a coordinate axis of any integer multiple of  $90^\circ$  resulting in the starting configuration. This means that through substitution of any coordinates following  $x_i \rightarrow \pm x_j$ . This will result in  $c_{11} = c_{22} = c_{33}$ ,  $c_{44} = c_{55} = c_{66}$  and  $c_{13} = c_{12}$ . The other constants, in this case, are all zero. To understand why, consider rotating the crystal around the  $x_3$  axis by  $90^\circ$ . This symmetry operation manifests as  $x_1 \rightarrow x_2$ ,  $x_2 \rightarrow -x_1$  and  $x_3 \rightarrow x_3$ . Under this operation, many constants are necessarily equal to their negatives, for example  $c_{56} = -c_{65}$ . As stated before, the symmetry of the system means that  $c_{ij} = c_{ji}$  so all constants with this condition must identically be zero. For a cubic crystal, the elasticity tensor from Eq. 5.5 is reduced to

$$c_{ij} = \begin{bmatrix} c_{11} & c_{12} & c_{12} & 0 & 0 & 0 \\ c_{12} & c_{11} & c_{12} & 0 & 0 & 0 \\ c_{12} & c_{12} & c_{11} & 0 & 0 & 0 \\ 0 & 0 & 0 & c_{44} & 0 & 0 \\ 0 & 0 & 0 & 0 & c_{44} & 0 \\ 0 & 0 & 0 & 0 & 0 & c_{44} \end{bmatrix} \quad (5.6)$$

since there are only 3 unique, non-zero, elastic constants (one constant for

Table 5.2: Table of all non-vanishing elasticity constants for the point group corresponding to CuMnAs.

$c_{11}$	$c_{12}$	$c_{13}$	0	0	0
	$c_{11}$	$c_{13}$	0	0	0
		$c_{33}$	0	0	0
			$c_{33}$	0	0
				$c_{44}$	0
					$c_{66}$

any stress and strain combination containing components in either 1, 2 or 3 coordinate axes simultaneously). For CuMnAs, in the P4/mmm point group, there are six non-zero elastic stiffness coefficients as shown in Table 5.2, where the elements below the diagonal are omitted for simplicity.

In the studies contained in this chapter, strain pulses are generated at the surface of the material with their wavevectors perpendicular to the surface. The generation mechanism only excites modes with displacement vectors, or polarisation vectors, with components parallel to this direction. This means that any mode with polarisation exclusively perpendicular to this direction will not be generated, i.e. pure transverse modes are not excited. For these studies there are two cases to examine. First is the case for the sample grown on GaP(001). Here the strain pulse travels parallel to the CuMnAs  $c$ -axis such that only a pure longitudinal mode is excited. In the case of the samples grown on high-index substrates, the generated pulse still travels perpendicular to the surface but, due to the orientation of the CuMnAs unit cell, the polarisation vectors travel off of a high-symmetry direction in the unit cell, meaning that the generated modes are not parallel to the propagation direction. In order to understand this, the Christoffel equation can be solved to describe propagation of waves through a crystal. The generic form of the Christoffel equation is

$$(\Lambda_{il} - v^2 \delta_{i,l}) e_l = 0 \quad (5.7)$$

where  $\Lambda_{il} = c_{ijkl} \hat{q}_j \hat{q}_k / \rho$  are the elements of a tensor,  $\hat{q}_i = q_i / q$  are the components of the unit vector parallel to the wavevector  $\underline{q}$  and  $i, j, k, l = 1, 2, 3$  are the

indices for the three cartesian axes in a 3D system.  $c_{ijkl}$  are the components of the elasticity tensor containing all elasticity constants,  $e_i$  is component a polarisation vector (pertaining to displacement of particles),  $\rho$  is the density of the material,  $v = \omega/q$  is the speed of the acoustic wave in direction  $\underline{q}$  with angular frequency  $\omega$  and  $\delta$  is the kronecker delta function. In the following, the elastic constants in  $\Lambda_{il}$  have undergone the conversions made using Table 5.1 [68]. The resulting terms were found by considering only the non-zero, unique elastic constants. Using Table 5.2, the terms in  $\Lambda_{il}$  for CuMnAs are

$$\rho\Lambda_{11} = c_{11}\hat{q}_1^2 + c_{66}\hat{q}_2^2 + c_{44}\hat{q}_3^2$$

$$\rho\Lambda_{22} = c_{66}\hat{q}_1^2 + c_{11}\hat{q}_2^2 + c_{44}\hat{q}_3^2$$

$$\rho\Lambda_{33} = c_{44}(\hat{q}_1^2 + \hat{q}_2^2) + c_{33}\hat{q}_3^2$$

$$\rho\Lambda_{23} = (c_{13} + c_{44})\hat{q}_2\hat{q}_3$$

$$\rho\Lambda_{31} = (c_{13} + c_{44})\hat{q}_1\hat{q}_3$$

$$\rho\Lambda_{12} = (c_{12} + c_{66})\hat{q}_1\hat{q}_2$$

and so fully written the Christoffel equation for CuMnAs is

$$\begin{pmatrix} c_{11}\hat{q}_1^2 + c_{44}\hat{q}_3^2 + c_{66}\hat{q}_2^2 - v^2\rho; & (c_{12} + c_{66})\hat{q}_1\hat{q}_2; & (c_{13} + c_{44})\hat{q}_1\hat{q}_3 \\ (c_{12} + c_{66})\hat{q}_1\hat{q}_2; & c_{66}\hat{q}_1^2 + c_{11}\hat{q}_2^2 + c_{44}\hat{q}_3^2 - v^2\rho; & (c_{13} + c_{44})\hat{q}_2\hat{q}_3 \\ (c_{13} + c_{44})\hat{q}_1\hat{q}_3; & (c_{13} + c_{44})\hat{q}_2\hat{q}_3; & c_{44}(\hat{q}_1^2 + \hat{q}_2^2) + c_{33}\hat{q}_3^2 - v^2\rho \end{pmatrix} \begin{pmatrix} e_1 \\ e_2 \\ e_3 \end{pmatrix} = 0. \quad (5.8)$$

If an acoustic wave is generated,  $e$  is necessarily non-zero so the expressions containing elastic constants and components of the wavevector which satisfy Eq. 5.8 are found when the determinant of the remaining term is zero:

$$\begin{vmatrix} c_{11}\hat{q}_1^2 + c_{44}\hat{q}_3^2 + c_{66}\hat{q}_2^2 - v^2\rho; & (c_{12} + c_{66})\hat{q}_1\hat{q}_2; & (c_{13} + c_{44})\hat{q}_1\hat{q}_3 \\ (c_{12} + c_{66})\hat{q}_1\hat{q}_2; & c_{66}\hat{q}_1^2 + c_{11}\hat{q}_2^2 + c_{44}\hat{q}_3^2 - v^2\rho; & (c_{13} + c_{44})\hat{q}_2\hat{q}_3 \\ (c_{13} + c_{44})\hat{q}_1\hat{q}_3; & (c_{13} + c_{44})\hat{q}_2\hat{q}_3; & c_{44}(\hat{q}_1^2 + \hat{q}_2^2) + c_{33}\hat{q}_3^2 - v^2\rho \end{vmatrix} = 0. \quad (5.9)$$

For the three propagation directions in CuMnAs, there are three cases to consider. Without specifying the angle of the CuMnAs *c*-axis to the sample surface normal, *z*, the high index samples can be considered together. In all three cases, the *x*<sub>1</sub>-axis is defined as parallel to CuMnAs[010] direction which lies in the plane of the sample surface. Let us first solve the case of the GaP(001) sample. Here, the propagation direction is given by

$$\hat{q} = \begin{pmatrix} \hat{q}_1 \\ \hat{q}_2 \\ \hat{q}_3 \end{pmatrix} = \begin{pmatrix} 0 \\ 0 \\ 1 \end{pmatrix} \quad (5.10)$$

and yields

$$|\Lambda_{il} - \rho\omega^2\delta_{i,l}| = \begin{vmatrix} c_{44} - v^2\rho & 0 & 0 \\ 0 & c_{44} - v^2\rho & 0 \\ 0 & 0 & c_{33} - v^2\rho \end{vmatrix} = 0 \quad (5.11)$$

with the following solutions:

$$v^2\rho = c_{33} \quad (5.12)$$

$$v^2\rho = c_{44}. \quad (5.13)$$

To determine which solution corresponds to the longitudinal mode, consider the expansion of Eq. 5.8 which yields three terms

$$(c_{44} - v^2\rho)e_1 = 0 \quad (5.14)$$

$$(c_{44} - v^2\rho)e_2 = 0 \quad (5.15)$$

$$(c_{33} - v^2\rho)e_3 = 0. \quad (5.16)$$

The first two correspond to modes with polarisations in the CuMnAs(100) and CuMnAs(010) planes, respectively. Both of these terms are purely transverse modes which are not excited in our experiment, as described previously. The

remaining option found in Eq. 5.16 is a purely longitudinal mode, since the only polarisation term is  $e_3$ , specifying that the oscillation occurs parallel to the propagation direction. Eq. 5.16 can be expressed in terms of the measured speed of sound as

$$v_{\text{LA}} = \sqrt{\frac{c_{33}}{\rho}}. \quad (5.17)$$

For the high index samples, the choice has been made to specify that the  $x_1$ -axis is parallel to the CuMnAs[010] direction which is in the plane of the surface and the  $x_2$ -axis lies along the CuMnAs[100] direction which points out of the surface plane at an angle of  $z$ . The  $x_3$ -axis is at an angle of  $z$  to the surface normal as illustrated in Fig. 5.1(b). The results are identical if the alternative choice for  $x_1$  and  $x_2$  is made. In the chosen case, the propagation direction becomes

$$\hat{q} = \begin{pmatrix} \hat{q}_1 \\ \hat{q}_2 \\ \hat{q}_3 \end{pmatrix} = \begin{pmatrix} 0 \\ \sin(z) \\ \cos(z) \end{pmatrix}. \quad (5.18)$$

Equation 5.9 then becomes

$$\begin{vmatrix} c_{44}\hat{q}_3^2 + c_{66}\hat{q}_2^2 - v^2\rho & 0 & 0 \\ 0 & c_{11}\hat{q}_2^2 + c_{44}\hat{q}_3^2 - v^2\rho & (c_{13} + c_{44})\hat{q}_2\hat{q}_3 \\ 0 & (c_{13} + c_{44})\hat{q}_2\hat{q}_3 & c_{44}\hat{q}_2^2 + c_{33}\hat{q}_3^2 - v^2\rho \end{vmatrix} = 0 \quad (5.19)$$

and the determinant is found to be

$$(c_{44}\hat{q}_3^2 + c_{66}\hat{q}_2^2 - v^2\rho) \dots \{(c_{11}\hat{q}_2^2 + c_{44}\hat{q}_3^2 - v^2\rho)(c_{44}\hat{q}_2^2 + c_{33}\hat{q}_3^2 - v^2\rho) - [(c_{13} + c_{44})\hat{q}_2\hat{q}_3]^2\} = 0 \quad (5.20)$$

with the expanded terms taking the forms

$$(c_{44}\hat{q}_3^2 + c_{66}\hat{q}_2^2 - v^2\rho) e_1 = 0 \quad (5.21)$$

$$(c_{11}\hat{q}_2^2 + c_{44}\hat{q}_3^2 - v^2\rho)e_2 - (c_{13} + c_{44})\hat{q}_2\hat{q}_3e_3 = 0 \quad (5.22)$$

$$(c_{13} + c_{44})\hat{q}_2\hat{q}_3e_2 - (c_{44}\hat{q}_2^2 + c_{33}\hat{q}_3^2 - v^2\rho)e_3 = 0. \quad (5.23)$$

Equation 5.20 has two separable terms. The first yields a solution corresponding to the pure transverse mode with a polarisation vector parallel to the  $x_1$ -axis (evident from Eq. 5.21), and so, as mentioned before, is not excited in our experiments. The other two solutions come from

$$(c_{11}\hat{q}_2^2 + c_{44}\hat{q}_3^2 - v^2\rho)(c_{44}\hat{q}_2^2 + c_{33}\hat{q}_3^2 - v^2\rho) - [(c_{13} + c_{44})\hat{q}_2\hat{q}_3]^2 = 0 \quad (5.24)$$

which correspond to the two non-pure modes. Eq. 5.24 be expanded to yield

$$\begin{aligned} v^4\rho^2 - [c_{11}\hat{q}_2^2 + c_{44}(\hat{q}_3^2 + \hat{q}_2^2) + c_{33}\hat{q}_3^2]v^2\rho + \dots \\ (c_{11}\hat{q}_2^2 + c_{44}\hat{q}_3^2)(c_{44}\hat{q}_2^2 + c_{33}\hat{q}_3^2) - [(c_{13} + c_{44})\hat{q}_2\hat{q}_3]^2 = 0 \end{aligned} \quad (5.25)$$

which is in the standard form of a quadratic ( $\alpha y^2 + \beta y + \gamma = 0$ ) where  $\alpha = 1$ ,  $y = v^2\rho$ ,  $\beta = -[c_{11}\hat{q}_2^2 + c_{44}(\hat{q}_2^2 + \hat{q}_3^2) + c_{33}\hat{q}_3^2]$  and  $\gamma = (c_{11}\hat{q}_2^2 + c_{44}\hat{q}_3^2)(c_{44}\hat{q}_2^2 + c_{33}\hat{q}_3^2) - [(c_{13} + c_{44})\hat{q}_2\hat{q}_3]^2$ . This yields two solutions from the quadratic formula

$$y_1 = -\beta + \sqrt{\frac{\beta^2 - 4\gamma}{2}} \quad (5.26)$$

$$y_2 = -\beta - \sqrt{\frac{\beta^2 - 4\gamma}{2}} \quad (5.27)$$

where  $y_1$  and  $y_2$  contain the values for  $v_{\text{LA}}$  and  $v_{\text{FTA}}$ , respectively. By combining these two solutions algebraically, the dependence of the speed on  $c_{13}$  can be isolated by taking the sum of the solutions

$$y_1 + y_2 = -2\beta \quad (5.28)$$

which, after substituting  $\beta$  in to Eq. 5.28, gives

$$v_{\text{LA}}^2 + v_{\text{FTA}}^2 = \frac{2}{\rho} [c_{11}\hat{q}_2^2 + c_{44}(\hat{q}_2^2 + \hat{q}_3^2) + c_{33}\hat{q}_3^2] \quad (5.29)$$

$$v_{\text{LA}}^2 + v_{\text{FTA}}^2 = \frac{2}{\rho} [c_{11}\sin^2 z + c_{44}(\sin^2 z + \cos^2 z) + c_{33}\cos^2 z]. \quad (5.30)$$

There are two samples with different values of  $z$  and therefore there are two values for  $v_{\text{LA}}^2 + v_{\text{FTA}}^2$  available. If  $c_{33}$  is found using Sample F, there are only two

remaining unknowns,  $c_{44}$  and  $c_{11}$ , in Eq. 5.30, and there are two simultaneous equations. It is then trivial to evaluate  $c_{11}$  and  $c_{44}$  using Eq. 5.30 and the four values of  $v$  and the two values of  $z$ . Finally,  $c_{13}$  can be found by evaluating Eq. 5.25 using any one of the values for speed and the previously calculated values of  $c_{33}$ ,  $c_{44}$  and  $c_{11}$ .

## 5.4 Results

To measure the thickness of the films, a selective etchant was used for the GaP(001) sample such that a step edge was formed by removing all the CuMnAs but without etching away the substrate. A step profiler was used to measure the size of this step edge and was found to be  $d = 229 \pm 5$  nm. A selective etchant was not known for the other samples so the thicknesses are assumed to be the same, since the calibrations used to grow all the films are the same.

Figure 5.4 contains the plots for the speed of sound measurements in ASOPS for the three samples used. Each of the repetition rates yield the same resulting reflections confirming that they are real reflected pulses. In (a), Sample F yielded only one peak as expected with  $t_{LA,F} = 100 \pm 2$  ps. In (b), Sample G contains two reflections with times of  $t_{LA,G} = 104 \pm 2$  ps and  $t_{FTA,G} = 151 \pm 3$  ps. In (c), Sample H gave times of  $t_{LA,H} = 108 \pm 2$  ps and  $t_{FTA,H} = 160 \pm 3$  ps. When taking the round trip distance,  $2d = 458 \pm 10$  nm, the speeds were found to be

$$v_{LA,F} = 4580 \pm 190 \text{ ms}^{-1}$$

$$v_{LA,G} = 4400 \pm 180 \text{ ms}^{-1} \quad v_{FTA,G} = 3030 \pm 130 \text{ ms}^{-1}$$

$$v_{LA,H} = 4240 \pm 170 \text{ ms}^{-1} \quad v_{FTA,H} = 2860 \pm 120 \text{ ms}^{-1}$$

The values for growth angles are  $z_G = 25.25^\circ$  and  $z_H = 35.26^\circ$  for Samples G and H, respectively. The density was calculated by summing the atomic masses within the unit cell and dividing by the unit cell volume to give

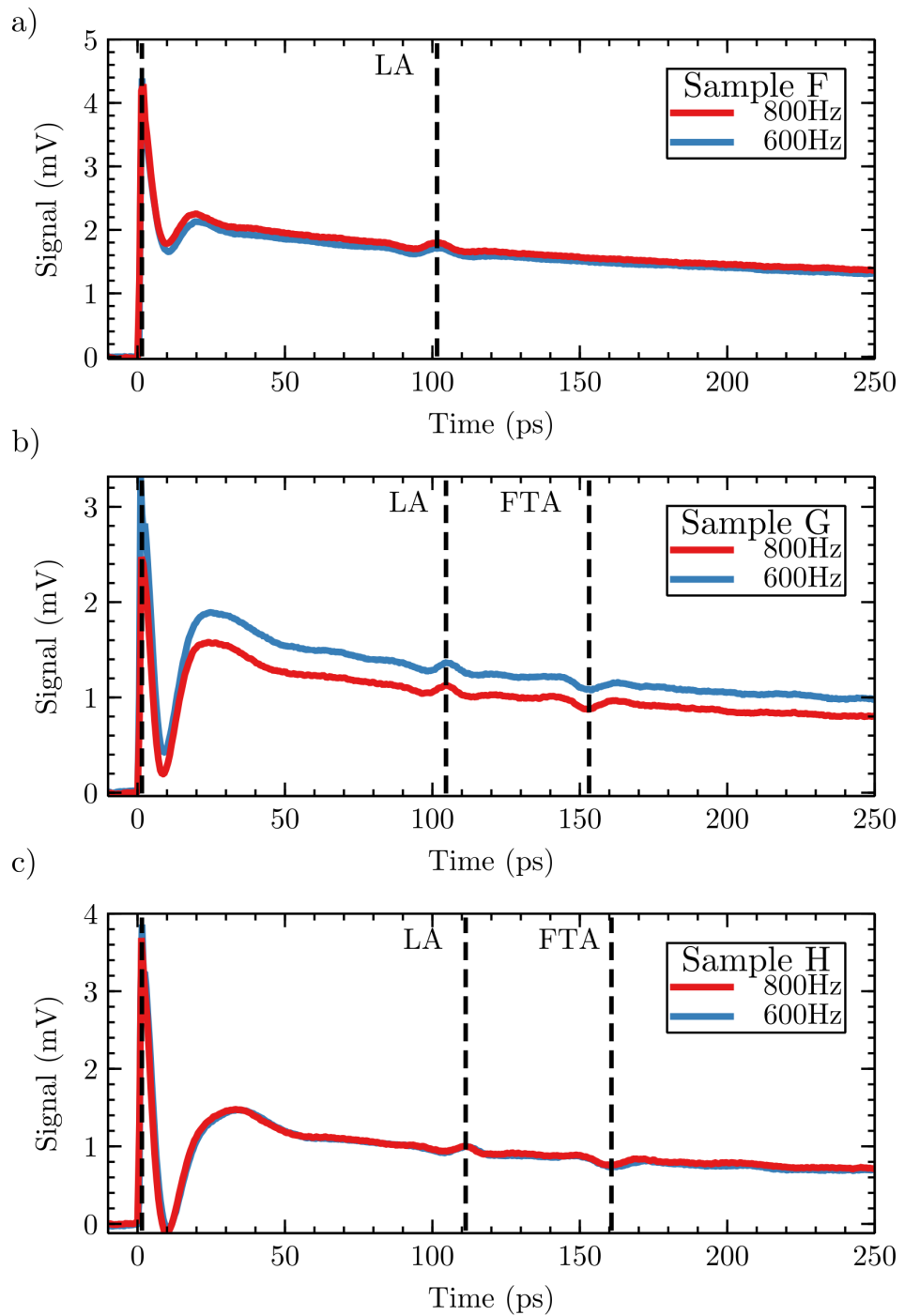


Figure 5.4: Plots of speed of sound traces collected using an ASOPS frequency difference of 800 Hz (red) and 600 Hz (blue) for light incident on (a) Sample F, the sample grown on the GaP(001) substrate (b) Sample G, the sample grown on the GaAs(113) high index substrate and (c) Sample H, the sample grown on the GaAs(112) high index substrate. The leftmost dashed line indicates the time of coincidence for the two beams, and the following dashed lines indicate the time values used in calculations for the labelled modes of oscillation.

Table 5.3: Table of results for non-vanishing elasticity constants for CuMnAs containing all calculated values in units of GPa.

$37 \pm 1$	$c_{12}$	$-40 \pm 6(-104 \pm 7)$	0	0	0
$37 \pm 1$		$-40 \pm 6(-104 \pm 7)$	0	0	0
		$146 \pm 12$	0	0	0
			$146 \pm 12$	0	0
				$73 \pm 7$	0
					$c_{66}$

$\rho = 6963 \text{ kg/m}^3$ . Using Eq. 5.17, the first elastic constant can be calculated as  $c_{33} = 146 \pm 12 \text{ GPa}$ . From Eq. 5.30, the longitudinal value for the velocities for each of the samples can be used to find two simultaneous equations including  $c_{11}$  and  $c_{44}$  as

$$v_{LA,G}^2 + v_{FTA,G}^2 = \frac{2}{\rho} [c_{11} \sin^2(z_G) + c_{44} + c_{33} \cos^2(z_G)] \quad (5.31)$$

$$v_{LA,H}^2 + v_{FTA,H}^2 = \frac{2}{\rho} [c_{11} \sin^2(z_H) + c_{44} + c_{33} \cos^2(z_H)] \quad (5.32)$$

which, when combined, yield values of  $c_{11} = 37 \pm 1 \text{ GPa}$ ,  $c_{44} = 73 \pm 7 \text{ GPa}$ . Equation 5.25 can be evaluated using any speed and the previous calculate values. Doing so yields  $c_{13} = -40 \pm 6 \text{ GPa}$  or  $c'_{13} = -104 \pm 7 \text{ GPa}$  depending on the chosen values used. Negative elastic constant values, although possible, are unlikely in our material and so this result is surprising. These results are summarised in Table 5.3 where the uncertainties were propagated by finding the maximum possible difference using values within the ranges and taking half of this difference as the uncertainty.

## 5.5 Conclusions

The round trip times for strain pulses were successfully measured for three directions of propagation using ASOPS and relatively thick CuMnAs layers. The speed of sound for a pure longitudinal acoustic mode was successfully calculated and used to evaluate one elastic constant:  $c_{33} = 146 \pm 12 \text{ GPa}$ . Two other positive elastic constants were measured as  $c_{11} = 37 \pm 1 \text{ GPa}$  and

$c_{44} = 73 \pm 7$  GPa with the final measurable constant having two possible values, both of which are negative:  $c_{13} = -40 \pm 6$  GPa or  $c'_{13} = -104 \pm 7$  GPa.

# Chapter 6

## Design, Development and Testing of a Room Temperature Vacuum System

### 6.1 Introduction

For AMR transport measurements, such as those described in Chapter 3 or in electrical switching experiments such as in Ref. 25, the normalisation of AMR by linear resistance induces a strong dependence of AMR signal amplitudes on temperature. When performing electrical switching experiments, this temperature dependence of AMR does lead to some small variation in the readout signal amplitudes. The switching threshold, however, is very sensitive to temperature. Changes in this threshold lead to a much more significant effect than the base resistance change. The typical switching pulses require a high current density ( $\sim 10^7 \Omega\text{cm}^{-2}$ ), generating a lot of heat in the sample, and then a lower power density ( $\sim 10^5 \Omega\text{cm}^{-2}$ ) DC current is used to perform an AMR measurement after the pulse. The power dissipated in the sample during this pulse-measure cycle can lead to temperature drift, both within the cycle and between cycles, and can lead to damage in the devices. Sinking the heat away from the device, therefore, is paramount to the survival of these

devices and repeatability of the measurements. Cryostats are a commonplace solution for controlling the temperature in similar measurements and perform very well at temperatures close to the temperatures of the chosen cryogen. Due to the reduction in threshold current with increasing temperature the switching experiments, and other characterisation measurements of CuMnAs, are ideally performed at or near room temperature. At room temperature, however, the precision of control can be lacking in cryostats. For these measurements, it is desirable to have a means of stable control of the sample temperature near to room temperature, with the sample in an oxygen free environment to avoid damage through oxidation.

In this chapter, the design, manufacture and characterisation of an inexpensive, stable temperature controlled vacuum chamber for electrical transport measurements at and near room temperature are reported. This system, dubbed the room temperature system (RTS), uses a Peltier device to control the sample temperature and has a short thermal path between the sample and a thermal reservoir to aid in the removal of waste heat from the sample. A routine electrical switching measurement is performed with and without the temperature control active in the RTS as a demonstration of the importance of temperature control in such an experiment.

A Peltier device is a bi-directional heat pump capable of high precision temperature control within a narrow temperature window. They are therefore a popular solution for temperature control near ambient temperature in many non-vacuum applications. A Peltier device can rapidly switch between heating and cooling to achieve stable and high precision temperature control. In Ref. 70, Raihane et al. report on a system in which a Peltier device, mounted outside a vacuum chamber, is used to control the temperature for measurements of the glass transition temperature in thin film polymers. Their design is effective for their specific requirements, however, for transport measurement applications several features could be optimised.

In their system the vacuum chamber is sealed with copper gaskets making

swapping samples expensive and difficult; the sample cell is separately sealed introducing more complexity; and the number of electrical connections to the sample is fewer than required for more general transport measurements. Our aim was to create a system that is more widely applicable for condensed matter research and to also include the following performance criteria: pressure  $<10^{-6}$  hPa, stability within  $\pm 10^{-2}$  K and range of -5–50 ° C. The system requires 12 possible electrical connections and a good thermal path between the Peltier device and the sample. Additionally, the Peltier power wires must be shielded from the measurement wires to avoid crosstalk.

The resulting design, developed by the author and photographed in Fig. 6.1, utilises a large mass of high purity copper as a thermal feedthrough, to which the Peltier device and sample space is attached. This copper is thermally regulated external to the vacuum using a conventional passive method. In the following, the key design features are explained with some important compromises being highlighted before the performance in terms of vacuum and temperature control are reported and an example switching experiment is provided as a demonstration of the typical application and the significance of stable temperature control in such an application.

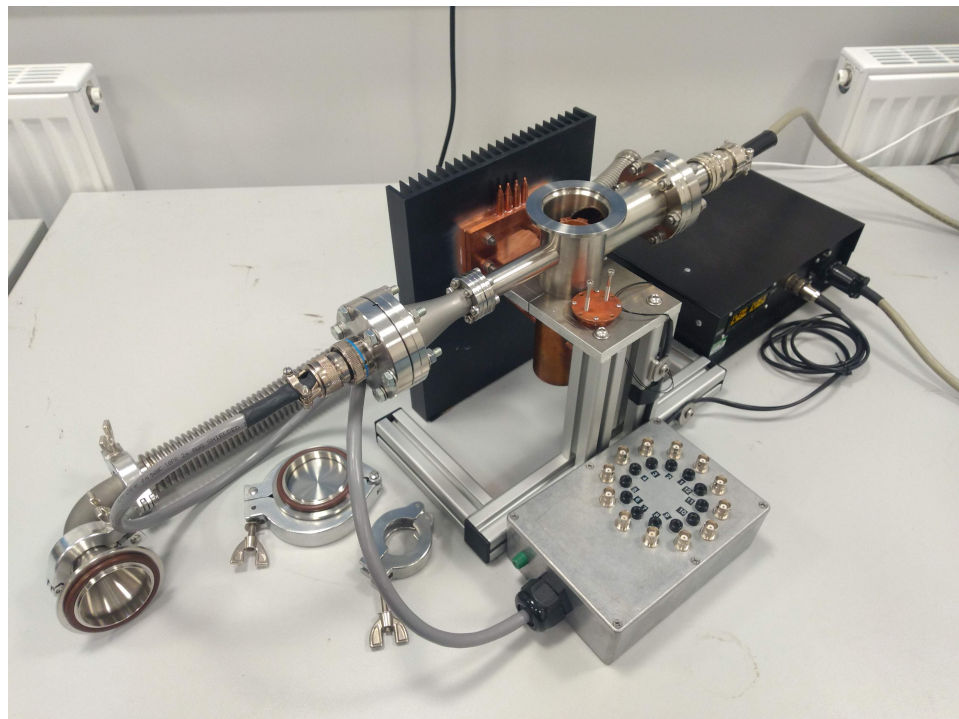


Figure 6.1: Photograph of the equipment and paraphernalia laid out including a break-out box and temperature control unit. The photograph shows the fully assembled system and demonstrates how the feedthroughs are utilised. The beige cable connects a Peltier device and PT100 sensor to temperature control unit which is in a housing with the mains AC to DC converter, screen and connectors. The think black cable connects the external thermocouple to the TEC controller. The grey cable leads to the the breakout box which provides convenient access to each of the 12 sample wires using either the central pin of a BNC or a 4mm banana plug.

## 6.2 Design

The system comprises a tee shaped vacuum chamber, as shown in the computer aided design (CAD) drawing of Fig. 6.2(a), with a pumping port on top and a sealed bottom achieved by vacuum brazing a copper cylinder inside it. This copper cylinder acts both as a mounting point and as a thermal feedthrough. The two arms of the tee are used for signal feedthroughs. The Peltier device is sandwiched between a copper sample space and the bottom copper cylinder of the vacuum chamber, with a bracket to tidy the wiring and keep the Peltier device central. Four holes in the copper cylinder below the vacuum chamber allow L-shaped heat pipes to conduct heat between the Peltier device and a heatsink with a two-part copper bracket sandwiching the pipes. A large passive heatsink was chosen over more common, small, fan assisted heatsinks because the vibrations of a fan may induce additional noise to sensitive measurements. The signal feedthroughs facilitate a 12-pin header on one side and the two power pins of the Peltier device and four pins of a PT100 platinum resistor on the other. The stand was made from extruded aluminium for the base and aluminium plate for the bracket. Stainless steel threaded rod was used to secure the heatsink to the stand and regular nuts and machine screws were used to apply mounting pressure to the copper bracket and heatsink contact areas. A thermocouple was inserted into the copper cylinder as centrally and as close to the Peltier as possible to provide heatsink temperature monitoring.

The sample space houses the resistor and the 12-pin sample header's matching socket as shown in Fig. 6.2(b). The sample is attached to a copper slug which runs through the center of the sample header, using thermally conductive and electrically insulating adhesive, and wires are ultrasonically bonded to connect the sample to the pins of the header. The sample header is placed into the sample socket to enable conduction from the sample to the external equipment. The lid and the raised stem of the sample space are designed to apply a small amount of pressure onto the header to ensure good thermal

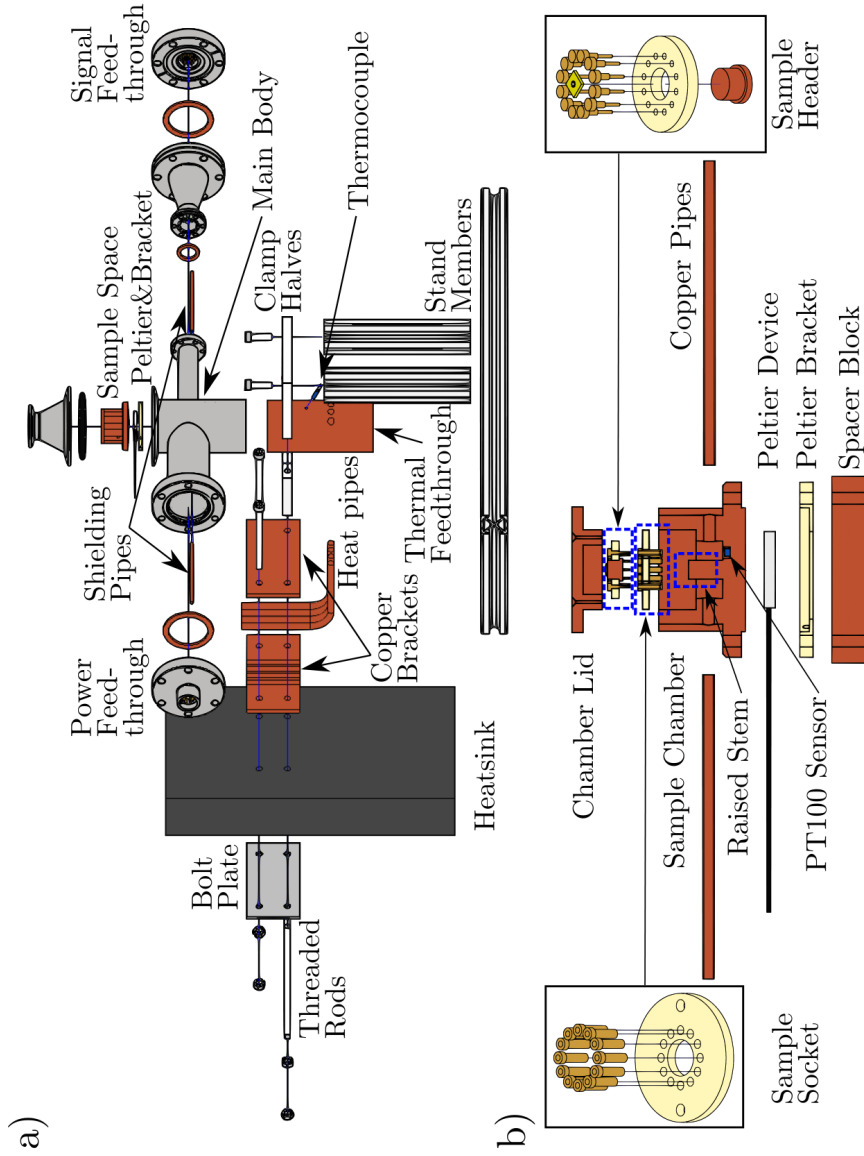


Figure 6.2: Exploded views of the 3D CAD drawings for the system excluding wiring and most fasteners. (a) shows the assembly of the whole system while (b) focuses on the smaller parts of the sample space.

contact between the sample and the Peltier device through this raised stem. The spacer block is simply the correction of a miscalculation whereby the pipes could not be inserted unless the sample space was raised by a centimetre. The sample socket is mounted to the sample space using two machine screws made from polyether ether ketone (PEEK), a machinable polymer suitable for high vacuum applications. The sample space, Peltier bracket and space block are all fastened to the copper cylinder of the vacuum chamber using steel screws.

To control the temperature, an off the shelf 20 W, 20 mm × 20 mm Peltier device is controlled by a Meerstetter Engineering<sup>TM</sup> TEC-1089 precision Peltier temperature controller. This reads both the sample space temperature and the external copper block temperature and has a range of features including protections and auto-tuning processes.

### 6.3 Manufacture

The main body of the vacuum chamber was made by welding the tubes and flanges to make the arms of the tee and then vacuum brazing the copper cylinder into the large tube. The body is a 50.8 mm outer diameter (OD) stainless steel tube with one 40 mm OD tube and one 19 mm OD tube. The 50 mm tube has a Klein flange for quick and easy access while the other two flanges are copper flanges for a better and more permanent seal. The 19 mm tube is expanded with an adapter to accommodate a 19-pin signal feedthrough and the 40 mm tube has a 6-pin power feedthrough. Four of these pins are used for the PT100 and the remaining two for the Peltier device itself. Any internal thermal contacting face is joined with vacuum-safe thermally conductive varnish while all external thermal contacts are joined with thermal paste.

Computer numerically controlled (CNC) milling machines and manual lathes were used in the manufacture of the three custom parts and to drill the four holes in the copper cylinder. These machines are also utilised to manufacture the proprietary headers. All the mounting holes were drilled using the CNC

mill and the heatpipe holes in the thermal feedthrough were first drilled and then reamed to enable a press fit.

The sample space and lid were first turned on a lathe before the internal geometries were milled. Through holes were drilled for bolting to the vacuum chamber and holes were drilled and tapped for attaching the lid and sample socket. The Peltier bracket, sample socket body and sample header bodies are made from PEEK. The pins and sockets were press fitted to their respective bodies. The Peltier device is inserted into the bracket with its wires fed through holes in this bracket. The copper heatpipe brackets were made by first drilling four holes in a block of copper and then splitting the block in half using a slitting saw on the mill. The meeting face of one bracket and the heatsink were polished, removing the anodising on the heatsink, to maximise thermal conduction. The stand members are made from extruded aluminium and the clamp halves were made by milling a 50.8 mm hole in a piece of 10 mm thick aluminium and then splitting it in twain. One half has a through hole to clear the threaded rods and the other is tapped to a matching thread.

The wiring uses vacuum safe solder to connect single core enamelled wires to the 12-pin sample socket and the PT100 sensor. The Peltier power wires are multi-core wires protected with ceramic beads. The feedthroughs have been designed such that the feedthrough can be removed from the wires on the inside and outside. The signal feedthrough uses crimp connectors to make a plug that can be inserted to the feedthrough as one piece. The power feedthrough uses double-ended copper screw terminals to make it possible to disconnect the wires so no solder is needed on these connections. On the outside, mil-spec connectors are typical and so these were used. The Peltier controller and necessary power supply and connectors are all housed in one box.

The external thermocouple is press fitted into the copper cylinder with thermal paste to improve thermal conductivity and the thermocouple has its own connector on the controller housing.

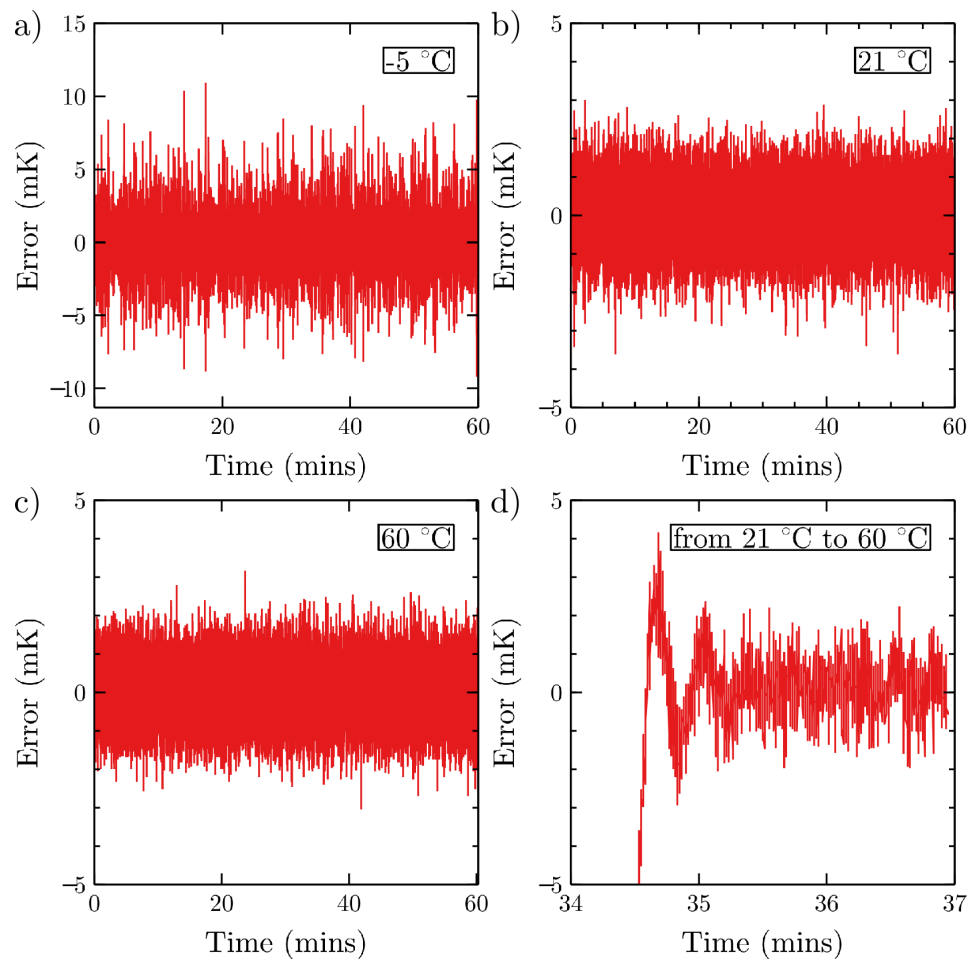


Figure 6.3: (a-c) Show plots of thermal stability over time for (a) -5°C, (b) 21°C and (c) 60°C with a room temperature of around 18 °C. (d) shows the stabilisation portion of a ramp from 21°C to 60°C with a target ramp rate of 0.01 °C/s.

## 6.4 Testing and Results

The key performance criteria are vacuum pressure, temperature control range and thermal stability. The control range was explored by increasingly moving the setpoint away from the ambient temperature until the controller could no longer reach that temperature. The stability was measured as the standard deviation of the error of the temperature measured by the PT100 resistor and the pressure was measured using the vacuum gauge on the inlet to the turbo pump.

Pressures of  $10^{-6}$  hPa are readily achieved by pumping with a turbopump. If lower pressures are required, by heating the sample space using nothing but the Peltier device, it is possible to reduce the pressure to  $10^{-8}$  hPa.

The maximum temperature range was found to be -8 °C to +65 °C with an ambient temperature of 22 °C. This corresponds to -30 K to +43 K from ambient. The stability was tested and can be seen in Fig. 6.3 (a-c). The stability was measured at (a) -5 °C, (b) 21 °C and (c) 60 °C, yielding standard deviations from the setpoint of 1.6 mK, 0.7 mK and 0.7 mK respectively. Figure 6.3 (d) shows the amount of overshoot when ramping the temperature from 21 °C to 60 °C using the ramp rate suggested by the autotuning. The maximum overshoot is 4 mK. The system is fully stable within a minute after reaching the target temperature.

A room-temperature switching experiment, following the procedures from Refs. 25,26,28,71, was carried out in the Peltier controlled vacuum system. An 8-arm device, with 10 μm arm width, was fabricated from Sample D, a 50 nm layer of CuMnAs epitaxially grown on GaP(001) using established methods [47,48]. Figure 6.4(a) shows an optical micrograph of the patterned device. The device was secured onto the sample header using thermally conductive adhesive and wire bonds were made between the device contact pads and the sample header pins. Once the device was loaded into the system sample socket, situated in the sample chamber as shown in Fig. 6.2(b), the system was evacuated to  $10^{-6}$  hPa pressures.

Current pulses of 51 mA amplitude ( $10^7 \Omega\text{cm}^{-2}$ ), 1 ms duration, were applied alternately along the diagonal arms of the device, as shown by the red and blue arrows in Fig 6.4(b). After each pulse, a continuous 1 mA ( $2 \times 10^5 \Omega\text{cm}^{-2}$ ) probe current was applied along the vertical arm of the device and the longitudinal voltage,  $V_{xx}$ , and transverse voltage,  $V_{yx}$ , were measured for the following  $\sim 200$  s. The plots in Fig. 6.4(c) show the measured sample space temperature (top row),  $R_{yx}$  (middle row), and  $R_{xx}$  (bottom row) during a pulsing sequence conducted with the Peltier controller turned off (left column) and set to 21 °C (right column). Note that the  $R_{yx}$  signals are centred on zero by subtracting the mean of the final 100 points in each trace.

Both the  $R_{yx}$  and  $R_{xx}$  signals exhibit appreciable temperature dependence.

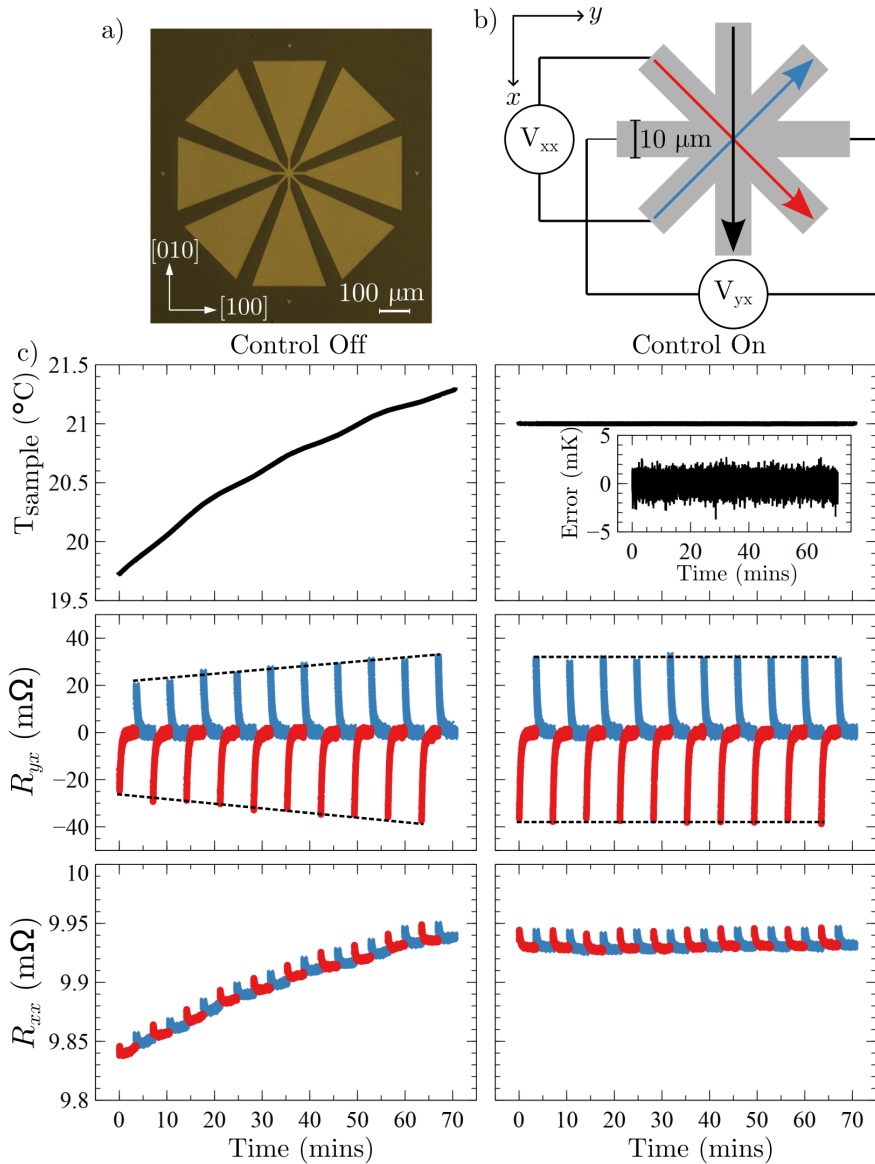


Figure 6.4: Current-induced resistive switching experiment conducted in the room-temperature system. (a) Optical micrograph of the 8-arm device, with 10  $\mu\text{m}$  arm width. (b) Schematic of the pulse and probe geometry. Pump pulses were applied along the diagonal arms of the device (red and blue arrows corresponding to red circles and blue crosses in (c)). After each pulse a continuous probe current was applied along the vertical arm of the device (black arrow, defining the  $x$ -axis) and the longitudinal voltage,  $V_{xx}$ , and transverse voltage,  $V_{yx}$ , were measured. (c) Switching measurements were carried out with uncontrolled temperature (left column) and with controlled temperature set to 21 °C (right column). The top two plots show the sample space temperature measured by the PT100 sensor, indicated in Fig. 6.2(b). The middle and bottom two plots show the respective  $R_{yx}$  and  $R_{xx}$  measured during a sequence of 10 pairs of pulses. As shown comparing the left and right plots, stable temperature is crucial for achieving reproducible switching data. The size of the  $R_{yx}$  signal increases as the system temperature increases and the base  $R_{xx}$  value follows the temperature drift.

With the Peltier controller turned off, a sample space temperature drift of  $\sim 1.5$  °C caused a change in the  $R_{yx}$  signal amplitude of  $\approx 30$  %, indicated by the dashed lines, and an  $R_{xx}$  base value drift of  $\approx 1$  %, following the shape of the sample temperature. When the Peltier controller was turned on, a stable sample temperature of  $21.000 \pm 0.003$  °C was achieved. The  $R_{yx}$  amplitude was consistent for the complete pulsing set, as shown by the dashed horizontal lines. The  $R_{xx}$  base value was stable within an 0.02 % variation.

## 6.5 Conclusions

A smaller thermal mass, and therefore more rapid thermal response and reduced costs, may appear attractive, however our experiments often include applying high current, short electrical pulses to a sample repeatedly. Because of this, a large thermal mass is preferable to diffuse the generated heat as quickly as possible. It is also helpful simply by increasing the heat capacity and thus reducing the effect of convection on the external side of the Peltier device. It is also for thermal stability reasons that we chose to place the Peltier device inside the vacuum chamber instead of having it exposed to air. Finally, we chose to cool the heatsink passively to avoid vibrations which may introduce noise in sensitive electrical measurements.

It may seem preferable for the system to be designed such that a heatsink could be directly attached to the thermal feedthrough, eliminating the need for heatpipes. This approach, however, necessitates added complexity in either manufacturing the system or changing the sample, since the system would either need to be designed with a complex shape of thermal feedthrough or be upside down to mount the heatsink to (what is currently) the bottom of the thermal feedthrough. This was deemed worse than the chosen solution for this application.

In its current form, a magnetic field can be applied along one axis (the in plane axis perpendicular to the arms of the tee) but the system cannot be

rotated between the poles of a magnet for full in plane measurements. To enable this, the changing of samples must become more fiddly or complicated because the arms of the system would have to be high enough to clear the poles of the magnet. It may be possible to design the system for this application but we did not prioritise magnetic field rotation measurements.

The use of thermally conductive varnish to create good thermal contacts means that replacing the Peltier device in case of failure is most likely to be arduous, requiring the vacuum chamber to be flooded in solvent to soften the varnish. It also requires delicate handling of the sample space and its fragile wires. The feedthrough has a removable connector on the inside making it possible to remove all the feedthrough entirely, the 19 mm tube is not big enough to fit the connector through. If the chamber was to be made again, the sample space would be raised even more to make swapping samples easier and both arms of the tee would be 40 mm tubes.

With some adaptation, the sample space could be used for many applications requiring this temperature range, however, if there is no need for a large number of signal wires or a small bore, it may be possible to find a simpler solution such as that by Raihane et al. [70]. There are many configurations possible for a Peltier controlled vacuum system, each with different priorities and drawbacks. In our case, thermal stability, ease of sample swapping and mitigation of electrical noise are our three top priorities with cost, simplicity and ease of manufacture suffering in exchange. We were set on having the Peltier device within the vacuum where this may not be necessary for all applications and we decided to not flip the system to change samples so that the system can stay rigidly mounted and easy to access.

Overall, this room temperature system has outperformed our other alternatives and provided a relatively cheap (compared to cryostats and cryogens) and convenient way to ensure only minimal thermal fluctuations occur in our transport measurements. The system allows for our samples to be protected from oxidation while under testing and has since become a staple in our research

for switching experiments and the experiments described in some experiments contained in Chapter 7. With some modifications we are confident that most researchers requiring transport measurements would benefit from such a system in their repertoire. There are a few possible quality of life changes that could be made and a couple of oversights that can easily be addressed, but these are minor and do not strongly affect the use of the system. The hope is that this design inspires and helps readers looking for a such a solution to discover their ideal system.

# **Chapter 7**

# **Developing a Pulsed Magnetotransport Measurement Technique for Investigating Néel Order Spin Orbit Torques**

## **7.1 Introduction**

When performing transport measurements, such as performing field sweeps to observe spin flop, the probing currents used are typically DC currents with low amplitude ( $\sim 10^4$  A cm $^{-2}$ ). This is because higher currents lead to heating in the device and this heating can lead to changes in the measured resistance values and damage to the device. The technique of delta-pulsing, which will be described in this chapter, allows for much higher (up to fifty times larger) probing currents by using short pulses of high currents to probe the sample instead of using DC current. Delta-pulsing is used to attempt to measure the deflection of moments as a result of Néel order spin orbit torque (NSOT). The resulting effect, dubbed quadratic magnetic deflection (QMD), is introduced and the expected dependence of QMD on applied current amplitude is explained. The experimental methods used to observe this effect at zero field and near

room temperature are described. The measurements are then repeated at low temperature ( $\leq 12$  K) in high magnetic field as an attempt to induce spin flop to change the sign of the signals. In doing these experiments, some new signal appeared and the rest of the chapter describes attempts to explore these signals and their origin.

### 7.1.1 Quadratic Magnetic Deflection (QMD)

As described in Section 2.7, the symmetry of the CuMnAs unit cell creates a spatially inhomogeneous spin polarisation when a current is passed in the *ab* plane through the inverse spin galvanic effect (ISGE). This inhomogeneous spin polarisation leads to opposite effective fields on each sublattice which act together to enable efficient reorientation of magnetic moments as a result of torques generated by NSOT [24]. The deflection of the moments due to the NSOT interaction results in an anisotropic magnetoresistance (AMR) change, the detection of which during the current pulse is referred to here as the QMD signal.

Godinho et al. [46] induced electrical switching of CuMnAs films using current pulses which, through NSOT, reorient some moments. They probed the corresponding changes to AMR using AC electrical transport measurements, observing changes in the second harmonic AC signals corresponding to second order AMR contributions. These were shown to be capable of distinguishing between  $180^\circ$  changes in the moments, which are not distinguished in DC measurements. Inspired by that study, the aim in this chapter is to extract the second order signals using high current pulses with alternating sign, with the intention of measuring the second harmonic effects but with a larger signal size. In the following explanation, the dependence of the size of the detected QMD signal on the applied current amplitude, and relative directions between the applied current and the magnetic moments, is derived by combining the form of the effective fields in Ref. 24 with the analysis in Ref. 72.

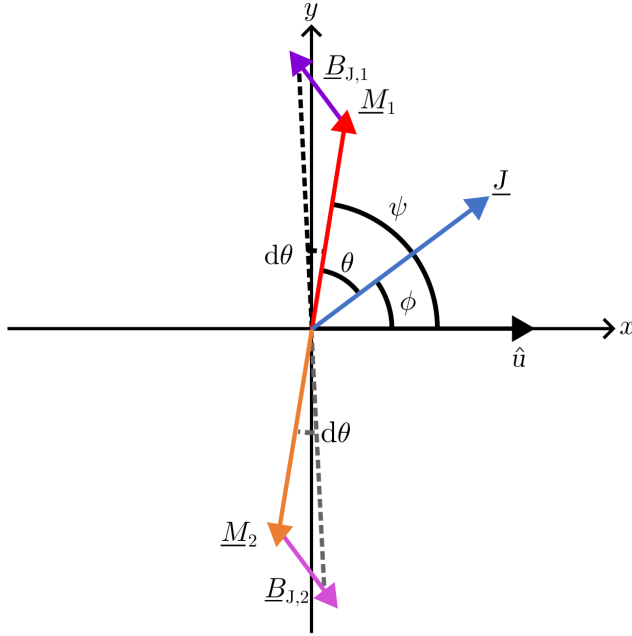


Figure 7.1: Geometry of the effective fields,  $\underline{B}_{J,1,2}$  on each sublattice  $\underline{M}_{1,2}$  with uniaxial anisotropy direction  $\hat{u}$ , with deflection through angle  $d\theta$ , as a result of spin orbit torque generated by an applied current  $\underline{J}$  causing NSOT.

The magnetic structure of CuMnAs can be considered as two ferromagnetic sublattices with antiparallel moments, labelled sublattices 1 and 2. Figure 7.1 illustrates the geometry of the system of CuMnAs in which an applied current,  $\underline{J}$ , magnetic sublattices 1 and 2 with magnetic vectors  $\underline{M}_1$  and  $\underline{M}_2$  respectively, with uniaxial anisotropy direction  $\hat{u}$  are shown. The resulting effective fields  $\underline{B}_{1/2}$ , and the extent of deflection,  $d\theta$ , are also drawn while the resulting torques, which are out of plane, are not drawn. Under the influence of the current each torque,  $\underline{T}_{1/2}$ , can be considered as the result of effective fields in the form of

$$\underline{T}_{1/2} \sim \underline{M}_{1/2} \times \underline{B}_{1/2} \quad (7.1)$$

where  $\underline{M}_1 = +m[\cos(\psi)\hat{x} + \sin(\psi)\hat{y}]$  is the magnetisation vector for sublattice 1 and  $\underline{M}_2 = -m[\cos(\psi)\hat{x} + \sin(\psi)\hat{y}]$  is the magnetisation vector for sublattice 2. The effective field is given by the sum of the anisotropy field,  $\underline{B}_u$ , and the

current induced NSOT field,  $\underline{B}_J$ , such that

$$\underline{B} = \underline{B}_J + \underline{B}_u \quad (7.2)$$

where

$$\underline{B}_{J,1} \sim +\hat{z} \times \underline{J} \quad (7.3)$$

$$\underline{B}_{J,2} \sim -\hat{z} \times \underline{J} \quad (7.4)$$

are the NSOT fields from Ref. [24]. The anisotropy field is given by

$$\underline{B}_u = -\frac{1}{\mu_0} \frac{\partial E_{\text{ani}}}{\partial \underline{M}} \quad (7.5)$$

$$= -\frac{1}{\mu_0} \frac{\partial}{\partial \underline{M}} [-k_u (\underline{M} \cdot \hat{u})^2] \quad (7.6)$$

$$= \frac{2k_u}{\mu_0} \hat{u} (\underline{M} \cdot \hat{u}) \quad (7.7)$$

where  $E_{\text{ani}}$  is the uniaxial anisotropy energy (see Sections 2.3 and 2.6). In the equilibrium state,  $\underline{M} \parallel \hat{u}$ , and the uniaxial anisotropy direction can be defined along the  $x$ -axis ( $\hat{u} = \hat{x}$ ). Therefore, the total effective fields are given by

$$\underline{B}_1 = \underline{B}_{J,1} + \underline{B}_{u,1} \quad (7.8)$$

$$= \left( -I \sin \phi + \frac{2k_u}{\mu_0} m \cos \psi \right) \hat{x} + I \cos \phi \hat{y} \quad (7.9)$$

$$\underline{B}_2 = \left( I \sin \phi + \frac{2k_u}{\mu_0} m \cos \psi \right) \hat{x} - J \cos \phi \hat{y}. \quad (7.10)$$

where  $I = |\underline{J}|$  is the applied current amplitude. The angle between the total effective field,  $\underline{B}$ , and a magnetic moment,  $\underline{M}$ , can be defined as  $\beta$ . This angle can be found using

$$\tan \beta = \frac{I \cos \phi}{-I \sin \phi + \frac{2k_u}{\mu_0} m \cos \psi} = \frac{\cos \phi}{-\sin \phi + \frac{2k_u}{\mu_0} \frac{m}{I} \cos \psi}. \quad (7.11)$$

Applying the earlier assumption that  $\underline{M} \parallel \hat{x}$  at  $I = 0$ ,  $\psi = 0$  and Eq. 7.11

reduces to

$$\tan \beta = \frac{\cos \phi}{-\sin \phi + \frac{2k_u m}{\mu_0 I}}. \quad (7.12)$$

In the steady state,  $\underline{M}$  tracks  $\underline{B}$  so that  $\psi = \beta$ . Under small applied current, i.e.  $\mu_0 I \ll 2k_u$ , the total effective field induces a deflection of the moments through  $\tan(\beta) \approx \beta \approx d\theta$  and Eq. 7.12 becomes

$$d\theta = \frac{I\mu_0}{2k_u m} \cos \phi. \quad (7.13)$$

Extending this to have  $\underline{B}_u$  and  $\underline{M}$  along arbitrary axes, such that these vectors are at an angle of  $\psi$  to the  $x$ -axis,  $\phi \rightarrow \theta$  since  $\theta = \psi - \phi$  (shown in Fig. 7.1) giving

$$d\theta = \frac{I\mu_0}{2k_u m} \cos \theta. \quad (7.14)$$

The deflection can be detected as a change in the measured AMR signals. The transverse voltage measured in AMR can be found by multiplying the equivalent resistance, from Eq. 2.5, by current (Ohm's law,  $V = IR$ ) which gives

$$V_{yx}(\theta) = R_{0,yx} \cdot I + \gamma I \sin(2\theta) \quad (7.15)$$

where  $\gamma$  is redefined to replace resistance with voltage to give

$$\gamma = \frac{1}{2} [V_{xx}(\underline{M}_{1,2} \parallel \underline{J}) - V_{xx}(\underline{M}_{1,2} \perp \underline{J})]. \quad (7.16)$$

where  $R_{0,yx}$  is added to account for linear voltage contributions generated by the device geometry and encapsulates the temperature dependence of this base resistance. If the applied current also induces a deflection based on the Néel

fields described above then the angle changes as  $\theta \rightarrow \theta + d\theta$  giving

$$V_{yx}(\theta) \rightarrow V_{yx}(\theta + d\theta) \quad (7.17)$$

$$V_{yx}(\theta + d\theta) = R_{0,yx} \cdot I + \gamma I \sin [2(\theta + d\theta)] \quad (7.18)$$

$$\begin{aligned} V_{yx}(\theta + d\theta) &= R_{0,yx} \cdot I + \dots \\ &\quad \gamma I [\sin(2\theta) \cos(2d\theta) + \cos(2\theta) \sin(2d\theta)] \end{aligned} \quad (7.19)$$

Taking the limit of small  $d\theta$  once more, and combining Eq. 7.19 with Eq. 7.14, produces

$$V_{yx}(\theta + d\theta) \approx R_{0,yx}I + \gamma I[\sin(2\theta) + 2d\theta \cos(2\theta)] \quad (7.20)$$

$$V_{yx}(\theta + d\theta) \approx R_{0,yx}I + \gamma I[\sin(2\theta) + \frac{I\mu_0}{k_u m} \cos\theta \cos(2\theta)]. \quad (7.21)$$

In delta-pulsing, two current pulses are applied with opposing directions. It is possible to consider these as the same system undergoing current inversion given by  $I \rightarrow -I$ . From Eq. 7.21, these become

$$V_{yx}(\theta + d\theta, I) \approx R_{0,yx}I + \gamma I \sin(2\theta) + \gamma \frac{\mu_0}{k_u m} I^2 \cos(\theta) \cos(2\theta) \quad (7.22)$$

$$V_{yx}(\theta + d\theta, -I) \approx -R_{0,yx}I - \gamma I \sin(2\theta) + \gamma \frac{\mu_0}{k_u m} I^2 \cos(\theta) \cos(2\theta). \quad (7.23)$$

If these two equations are summed the result is

$$\begin{aligned} V_{yx}(\theta + d\theta, I) + V_{yx}(\theta + d\theta, -I) &\approx R_0I - R_0I + \gamma I \sin(2\theta) - \dots \\ &\quad \gamma I \sin(2\theta) + 2\gamma \frac{\mu_0}{2k_u M} I^2 \cos(\theta) \cos(2\theta) + \gamma \frac{\mu_0}{k_u m} I^2 \cos(\theta) \cos(2\theta) \end{aligned} \quad (7.24)$$

which simplifies to

$$\text{QMD}_\perp = V_{yx}(\theta + d\theta, I) + V_{yx}(\theta + d\theta, -I) \approx \gamma \frac{\mu_0}{k_u m} I^2 \cos(\theta) \cos(2\theta) \quad (7.25)$$

where  $\text{QMD}_\perp$  is the transverse QMD signal. This removes the contribution from linear resistance and normal AMR measurements, leaving only a quadratic

dependence on current amplitude. It is because of this quadratic dependence that the name quadratic magnetic deflection (QMD) is chosen within this chapter, and it is QMD that delta-pulsing aims to measure by pulsing in opposing directions and varying the magnitude of the current.

Taking the same approach for the  $V_{xx}$  signal, starting with the voltage version of Eq. 2.5:

$$V_{xx}(\theta) = R_0 \cdot I + \gamma \cos(2\theta)I \quad (7.26)$$

gives

$$\text{QMD}_{\parallel} = V_{xx}(\theta + d\theta) + V_{xx}(\theta + d\theta + \pi) \approx -\gamma \frac{\mu_0}{k_u m} I^2 \cos(\theta) \sin(2\theta) \quad (7.27)$$

where  $\text{QMD}_{\parallel}$  is the longitudinal QMD signal. Both QMD measurements give a signal proportional the square of the applied current magnitude but with the largest signals appearing at different relative angles between the magnetic moments and applied current (maximum  $\text{QMD}_{\perp}$  for  $J \parallel L$  i.e.  $\theta = 0$  and maximum  $\text{QMD}_{\parallel}$  for  $\theta = \pm 35.26^\circ$ ). The observed QMD signal can be understood as deviations from linear AMR behaviour as a result of the rotation of moments caused by NSOT.

### 7.1.2 The effect of NSOT on Domains and Domain Walls

In the case of an even domain system (a system with all domain populations being equal), the contributions to the QMD signal will equal zero because each antiparallel domain will contribute oppositely to the deflection signal. If the system is not even, then the QMD signal will be proportional to the relative difference in domain populations. In the case of a sample with large domains ( $\sim 1 \mu\text{m}$ ) and small device geometry ( $\sim 10 \mu\text{m}$ ), the number of domains and domain walls of each type are very much finite and an even population is statistically very unlikely, however the total signal is still expected to be reduced because of the competition between all the contributions. If, instead,

the effects of domain wall (DW) motion are considered, a larger signal can be expected because the pulse itself may disrupt the steady state and lead to a significantly higher proportion of moments in a certain direction.

To understand this, consider the DW illustrated in Fig. 7.2(a), consisting of one  $180^\circ$  DW separating two antiparallel domains for a uniaxial system. In the illustrated example, the current,  $\underline{J}$ , is applied perpendicular to the Néel vector,  $\underline{L} = \underline{M}_1 - \underline{M}_2$ , on both sides of the DW. The direction of expected deflection (curved black arrows) as a result of the NSOT effective fields (purple and pink arrows) for moments in each domain is opposite on each side of the DW. This means that the total deflection will be zero and will yield no modification to the AMR signal in the steady state. The domain on the left (with  $\underline{M}_{1/2} \parallel \underline{B}_{1/2}$ ), however, is energetically favourable because of the Zeeman energy term associated with the effective field. This leads to the expansion of the left domain and shrinking of the right domain through DW motion, indicated by the straight black arrow. If the applied current is reversed, the DW motion is also reversed and so any signal generated by this motion will be doubled when the difference in these two signals is calculated. If the domains are rotated through  $90^\circ$  through spin flop, then the configuration in (a) becomes one of the configurations in (b-c) whereby the current is applied collinear to the magnetic moments within the domains while the effective field is parallel or antiparallel to the moments in the centre of the domain walls. The difference between Fig. 7.2(b) and (c) is in the chirality (direction of rotation) of the DW with (b) having counter-clockwise chirality and (c) having clockwise chirality. In (b) the applied current generates an effective field antiparallel to the centre of the domain wall and so the domain wall is caused to shrink, while in (c) the effective field is parallel to the centre of the domain wall and so the domain wall is energetically favourable and expands. If the current is applied at an arbitrary direction to  $\underline{L}$ , then the exact resulting modification to the domain wall is dependent on the chirality of the DW but, in general, the most energetically favourable domain will expand while the unfavourable domain will contract.

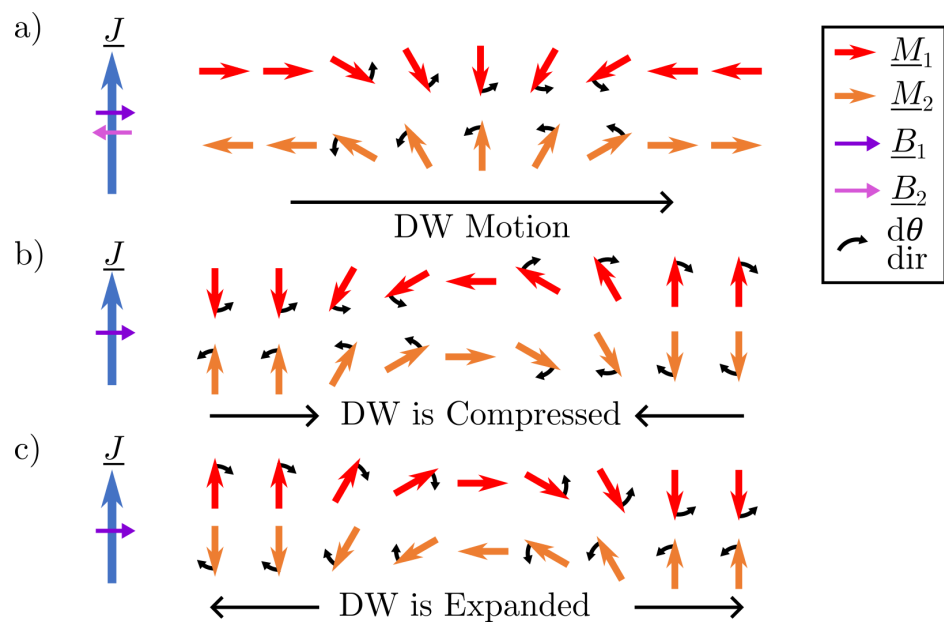


Figure 7.2: Diagrams showing the effects of NSOT on a uniaxial 180° domain wall with the current induced NSOT effective fields (a) parallel to the moments in one domain and antiparallel to the moments in the other (b) antiparallel to the moments in the centre of the domain wall and (c) parallel to the moments in the centre of the domain wall. The resulting effects are (a) the expansion of the energetically favourable domain type through domain wall motion (b) the contraction of the domain wall and (c) the expansion of the domain wall.

The resulting DW motion leads to a dominant domain population which creates a deviation from zero QMD signal. The sign of this change in QMD signal should be opposite for opposite directions and thus should lead to the same sign of measured voltage if the voltage measurement geometry is unchanged. If the QMD signals are measured for multiple directions, the signal for  $\underline{J} \parallel \underline{L}$  should be largest and  $\underline{J} \perp \underline{L}$  should be smallest. If spin flop is induced in the sample,  $\underline{L}$  will rotate through  $90^\circ$  and so the direction which results in each magnitude of signal should rotate through  $90^\circ$  with respect to the crystallographic directions as well. It is to this end that delta-pulsing is used to try and detect this spin flop reorientation using the QMD signal.

### 7.1.3 Delta-Pulsing

The term delta-pulsing, used throughout this chapter, refers to the application of a series of measurements using pulsed current (called pulse delta measurements) with the goal of determining the current-induced effective fields in an antiferromagnet by measuring the extent of QMD along various crystal directions. To do this, the measurement was repeated along four crystallographic directions and the measured voltages were processed to extract the parts of the signal that were symmetric in applied current amplitude, which should correspond to the QMD signal. By analysing the directional dependence of QMD it is hoped that some magnetic information can be determined.

The general process for the technique is described below and the methods implemented to develop the technique and confirm the magnetic origin of the resulting signals are detailed. These methods are separated into two sections: those performed in the RTS, in the absence of magnetic fields, and those performed in magnetic fields, requiring a superconducting magnet and corresponding cryostat.

Delta-pulsing utilises, specifically, the combination of two products from Keithley Instruments, LLC, namely the model 6221 AC/DC current source and

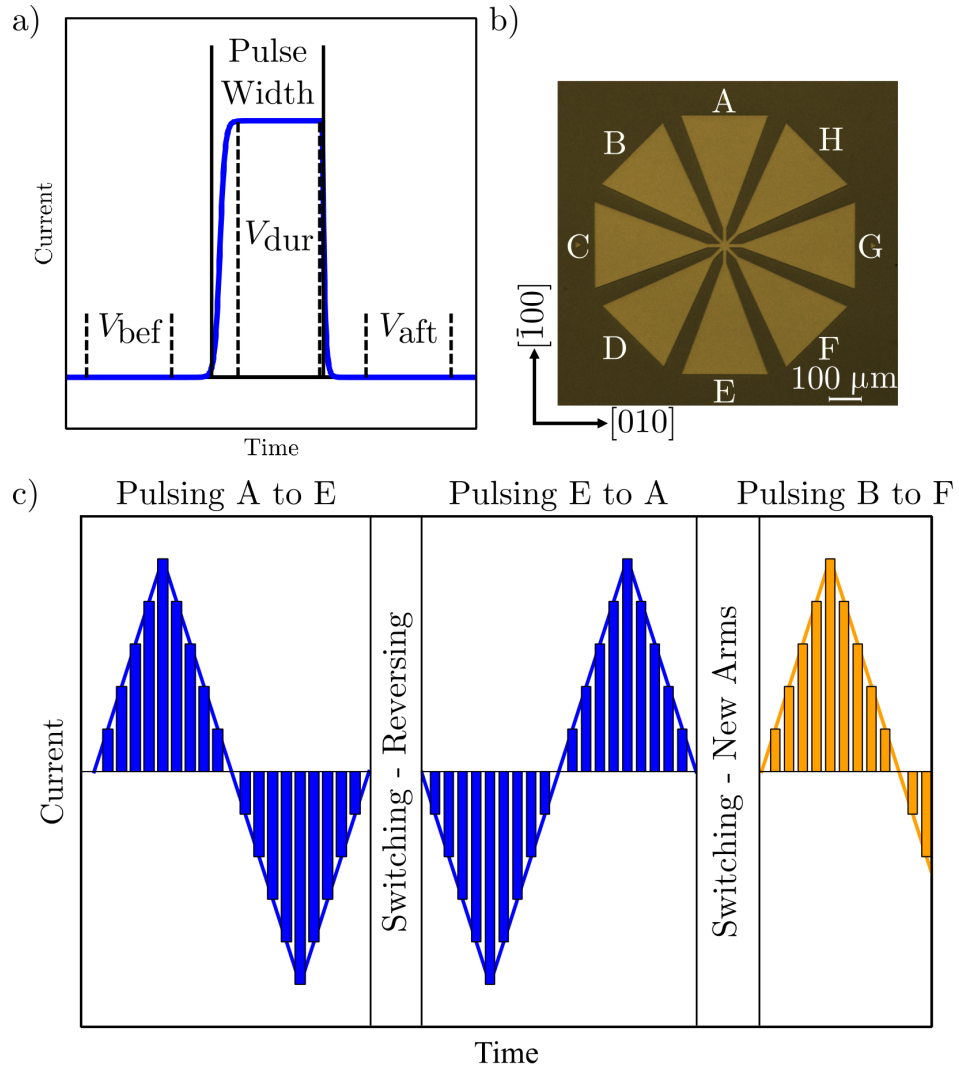


Figure 7.3: Schematics to describe the delta-pulsing technique. (a) An illustration of the pulse shape and measurement times used in a pulse delta measurement. (b) Micrograph image of an 8-arm asterisk device fabricated through wet etching photolithography techniques. (c) An illustration of the staircase pulse method as a function of time in which pulses are applied with increasing amplitude up to a maximum before being decreased. The pulses have duration of  $\sim 500 \mu\text{s}$  with a typical delay between pulses of either 1 ms or 100 ms. The pulse staircase is repeated multiple times before the geometry is switched, first to reverse the order of the sign of the pulses before rotating the geometry through  $-45^\circ$ .

the model 2182A nanovoltmeter, to perform pulse delta voltage measurements. The instruments are designed to communicate directly to enable rapid and short duration, and therefore low total energy, transport measurements by synchronising the pulsing from the sourcemeter with the measurement by the nanovoltmeter. Figure 7.3(a) illustrates the structure of a pulse delta measurement in which a voltage measurement is taken just before ( $V_{\text{bef}}$ ), during ( $V_{\text{dur}}$ ) and just after ( $V_{\text{aft}}$ ) a current pulse. The resulting value,  $V_{\text{PD}}$ , is calculated from these three measurements as

$$V_{\text{PD}} = V_{\text{dur}} - \frac{(V_{\text{bef}} + V_{\text{aft}})}{2} \quad (7.28)$$

which is explicitly the difference between the measurement during the pulse and the mean of the measurements in the absence of the pulse. The two background measurements remove any impact of floating voltages or remnant charge in the device. In a pulse delta measurement using these instruments, the pulse width (duration) can be set as low as 50  $\mu\text{s}$ , but in our testing, the shape of the pulse applied to our devices is only consistent at pulse widths above 0.2 ms, presumably due to impedance matching.

To enable the measurement of QMD along four crystallographic directions, the materials were patterned into 8-spoked asterisk shaped devices, photographed in Fig. 7.3(b). As shown, the device arms are labelled in alphabetical order, progressing counter-clockwise from A through to H, choosing A such that a line from A to E is parallel to the CuMnAs[100] or CuMnAs[ $\bar{1}00$ ] direction (the hard axis for uniaxial samples). The measurements were performed along each pair of arms in the device (connections between A&E, B&F, C&G and D&H form the pairs) with varying applied current amplitudes.

Delta-pulsing requires many combinations of connections to the device in order to measure QMD along all the pairs of arms. A piece of equipment, referred to here as the switch box, was employed to provide a means to change which arms of the device the instruments were connected to. The switch

box has the capacity for six instrument connections to be connected to up to eight device contacts, and the connections can be changed quickly ( $\sim 5$  ms) through serial communication and software. Thusly, the switch-box allows for convenient automation of delta-pulsing. The nanovoltmeter used cannot simultaneously measure both desired voltages,  $V_{xx}$  and  $V_{yx}$ , so only four input connections are required in this case. A shorthand format is used throughout this chapter to describe the connection configurations whereby the letters for each arm on the device is assigned to the instrument pins in the order of  $I+$ ,  $I-$ ,  $V+$  then  $V-$ . As an example, AECG would describe a configuration in which positive current flows from A to E and a voltage is measured between C (positive) and G (negative). Because the path from A to E is perpendicular to path from C to G, this corresponds to measuring  $V_{yx}$ . Similarly, BFCE would describe a configuration in which positive current flows from B to D, with  $V_{xx}$  being measured between C and E. If, instead, a two character code is used, this corresponds only to the axis of the pulsing and contains the suggestion of the reversed current without changing the probing configuration (AE would correspond to a measurement consisting of AECG followed by EA corresponding to EACG).

In delta-pulsing, pulses of varying current density are used to induce QMD, and the resulting voltages,  $V_{xx}$  or  $V_{yx}$ , are measured during each pulse. The specific structure of the delta-pulsing process was varied as part of the development of the technique but the most common method used here was to apply sweeps of pulses as illustrated in Fig. 7.3(c), in which current pulses were applied in a staircase sweep up to a maximum, down through zero to a negative maximum and back to zero. This sweep was repeated multiple times before the contacts for the applied current were swapped. Swapping the current direction means that the first current pulse was applied in the opposite direction, but the voltage measurement maintains its polarity (AECG becomes EACG). This is equivalent to running the sweeps in reverse, but was simpler to program. By swapping the order of pulsing, any hysteretic effects that are polarity dependent

can be removed or accentuated in processing by combining these two sets of sweeps. The measurement geometry was then rotated through  $-45^\circ$  and the next pair of sets of sweeps was performed. The rotation was repeated twice more such that a total of eight configurations were measured. For  $V_{yx}$ , the eight usual configurations were AECG, EACG, BFDH, FBDH, CGEA, GCEA, DHFB and HDFB. For  $V_{xx}$ , the eight usual configurations were AEBD, EABD, BFCE, FBCE, CGDF, GCDF, DHEG and HDEG .

In order to measure QMD, the first sweep can be added to the second sweep such that the pulse along AE at the start of the sweep is added to the pulse along EA at the start of the sweep. This results in a plot of the sums of opposing current pulse signals as a function of applied current, as required to plot Eq. 7.25. This was done for four crystallographic directions ( $[100]$ ,  $[110]$ ,  $[010]$  and  $[1\bar{1}0]$ ) and the results were interpreted with the aim of extracting some magnetic information from the sample, such as the magnetic anisotropy directions or the predominant domain type.

The RTS (described in Chapter 6), was used for the initial measurements of delta-pulsing because short duration, high amplitude current pulses are applied to the sample and the RTS is effective at extracting the heat generated by Joule heating. In order to get a good signal-to-noise when making such short measurements, many repeats were required and so the high stability of the RTS chamber enables long measurement durations without changes in temperature.

Delta-pulsing can also be used to continuously probe a device with a constant current amplitude while some other process is used to manipulate the magnetic ordering. Typically, a DC probe current is used to measure magnetoresistance in spin flop experiments (see Section 3.2.2). To demonstrate this capability, magnetic field sweeps were used to induce spin flop while  $V_{yx}$  or  $V_{xx}$  was probed using continuously applied pairs of short, constant amplitude, delta-pulses of alternating sign.

## 7.2 Characterisation of Delta Pulsing Signals

Each of the following sections contain the experimental details and corresponding results and discussion for each investigation performed, using two samples: Sample C, a uniaxial 45 nm layer of CuMnAs and sample E, a biaxial 50 nm layer of CuMnAs, both grown on GaP(001) substrates. Three distinct studies are described. First are basic delta-pulsing staircase sweeps conducted in the RTS in the absence of field, followed by high magnetic field measurements using delta-pulsing staircases at various magnetic field strengths, and last are the field dependence measurements of signals measured using antiparallel pulses with continuous current amplitude.

### 7.2.1 Delta-Pulsing in the RTS

Devices with 10  $\mu\text{m}$  arm widths of the geometry shown in Fig. 7.3(b) were fabricated on Samples C and E. These were mounted onto copper-slug headers as shown in Fig. 6.2(b) such that the samples are thermally connected to the Peltier device in the RTS (described in Chapter 6). The samples were mounted in the RTS and the chamber was evacuated to  $10^{-6}$  hPa with the temperature set to 21  $^{\circ}\text{C}$ . Delta-Pulsing was conducted on each sample following the pattern shown in Fig. 7.3(c) with current amplitudes up to  $\pm 15$  mA, achieved in steps of 0.5 mA .

The plots in Fig. 7.4 show the resulting plots of  $V_{yx}$  as a function of current amplitude for each sample. Figure 7.4(a) corresponds to  $V_{yx}$  measurements conducted on uniaxial Sample C. The dependence appears linear, with very little difference between orthogonal or antiparallel pulse directions, however the lateral and diagonal arms are of significantly different amplitudes, with the diagonal arms (BF, DH) having gradients almost ten times larger than the lateral arms (AE, CG). This is probably due to the crystallographic contributions to the AMR, but may have some contribution from small patterning asymmetry hence requiring the addition of  $R_{0,yx}$  in Eq. 7.15. Figure 7.4(b) corresponds

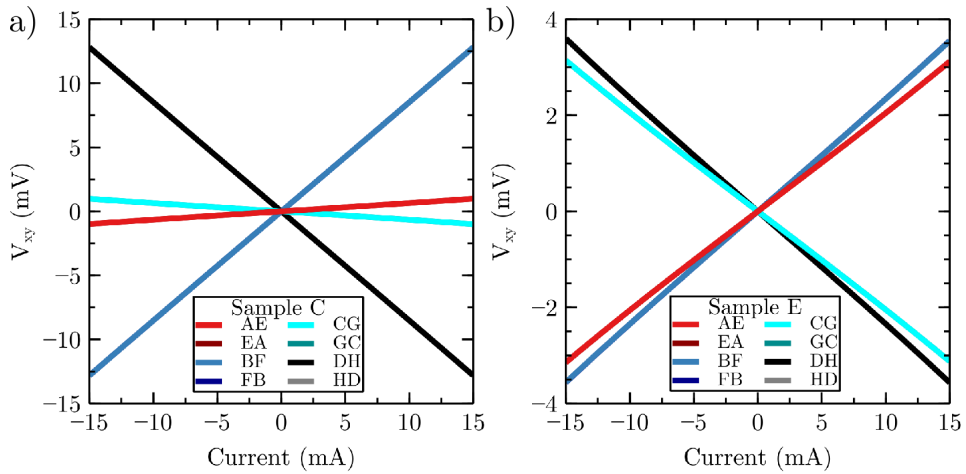


Figure 7.4: Examples of delta pulsing  $V_{yx}$  results as a function of applied current for (a) uniaxial Sample C, 45 nm CuMnAs on GaP(001) and (b) biaxial Sample E, 50 nm CuMnAs on GaP(001). Each measurement is the result of 10 averages using current steps of 0.25 mA up to  $\pm 15$  mA.

to the  $V_{yx}$  measurements conducted on Sample E, a biaxial, 50 nm CuMnAs layer grown on GaP(001). Each plot appears to show a linear dependence with a similar gradient, however there is a small difference between the lateral (AE, CG) and diagonal (BF, DH) arms, where the lateral in Sample E arms gave smaller gradients. The biaxial anisotropy in this device suggests that these should have the same gradient and so these are probably caused by the aforementioned patterning asymmetry.

The differences in each antiparallel staircase sweep are hidden by the scale of the plots in Fig. 7.4, so the  $\text{QMD}_\perp$  signal is not visible in them. Therefore, Fig. 7.5 is made containing the plots of the  $\text{QMD}_\perp$  signals, calculated by taking the sum of each pair of pulse sweeps (i.e. AE $\text{CG}$  is added to EA $\text{CG}$ ) from Fig. 7.4, following Eq. 7.25. In the  $\text{QMD}_\perp$  plots, there is a clear parabolic shape to all the signals. The measurements of uniaxial Sample C are shown in (a). In these plots, three of the parabolas are negative and only one is positive. The magnitudes of all parabolas are similar, between 5 and 15  $\mu\text{V}$  at 15 mA, are largest for pulses along the CG easy axis. The parabolas with current along the diagonal arms (BF and DH), have some step-like behaviour visible, which is attributed to a measurement range change within the voltmeter which only occurs along the arms with larger crystalline anisotropy contributions to

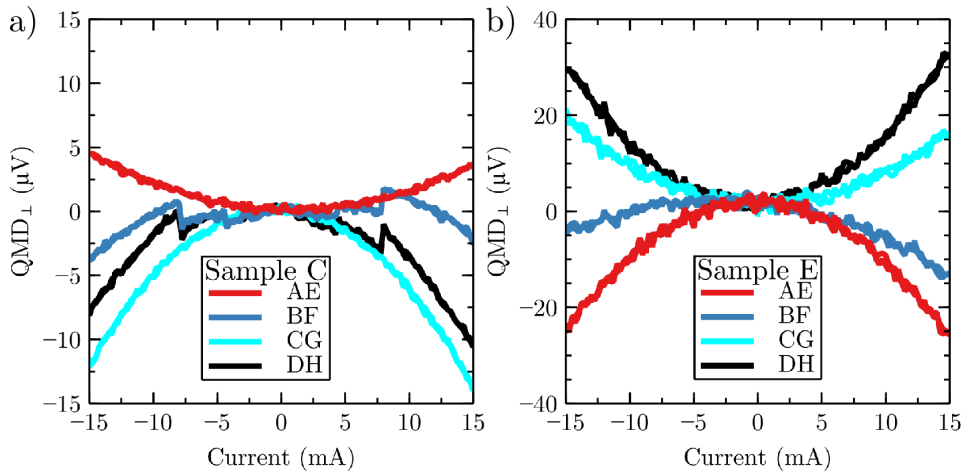


Figure 7.5: Examples of delta pulsing  $\text{QMD}_\perp$  results measuring  $\text{QMD}$  by taking the sum of pairs of I-V curves from Fig. 7.4 for (a) uniaxial Sample C and (b) biaxial Sample E. Each measurement is the result of 10 averages using current steps of 0.25 mA up to  $\pm 15$  mA.

$V_{yx}$ . The data in (b) is for Sample E, the biaxial sample, which displays four parabolas, two positive and two negative, with no clear symmetry dependence with the expected QMD geometries.

The fact that the symmetry of the parabolas is different between the uniaxial and biaxial sample suggests that the origin of the signals is related to the anisotropy. The largest magnitude of signals appears for an applied current parallel to the easy axis in Sample C which does suggest some dependence of signal amplitude on the  $\underline{L}$ -vector. Understanding the biaxial results is more difficult but the similarity in all signals suggests that domain wall motion may be enabling signals for all current directions.

### 7.2.2 Delta-Pulsing Field Steps

Reorienting the moments and repeating the delta-pulsing sequences should lead to evidence of the magnetic origin of the signals so this is done using spin flop. New devices with 10  $\mu\text{m}$  arm widths of the geometry shown in Fig. 7.3(b) were fabricated on Samples C and E. These were mounted on 12-pin headers similar to the ones used in the RTS, but lacking the copper slug. The samples were placed into the bore of a cryostatic solenoid magnet capable of field strengths

over 16 T. The samples were set to a temperature of 10 K while delta-pulsing was conducted at various applied field strengths in each sample. The same procedure was used for each measurement, taking 10 averages and using a maximum current amplitude of 40 mA, achieved in steps of 0.2 mA, with a delay of 0.1 s between each pulse cycle and a delay of 5 ms between each pulse. At high fields, bond wires were breaking due to the Lorentz force in the bond wires and so not all sets of measurements reach 16 T. To solve this, two wires were bonded to each pad instead of one, roughly halving the force on each wire at a given current.

The field strength dependence of  $\text{QMD}_\perp$  and  $\text{QMD}_\parallel$  signals were investigated by measuring each QMD signal as a function of applied current amplitude using uniaxial Sample C with a magnetic field applied along the CG easy axis. Plots of the corresponding  $V_{yx}$  signals are given for a set of data measured above the spin flop field to highlight the magnitude of the observed changes. In order to investigate the dependence of the observed signals with respect to applied field direction, the magnetic field was also applied along two more directions of Sample C, namely along the DH diagonal and the AE hard axis. In those measurements, field strengths of 0 T and 4.5 T was used in order to investigate the dependence of the magnetic field direction on the appearance of the winging signals. The directional dependence investigation was repeated using biaxial Sample E, in which  $\text{QMD}_\perp$  was measured as a function of current amplitude at various applied field strengths, with the field applied along one easy axis (DH) and one hard axis (AE). Finally, measurements of  $\text{QMD}_\parallel$  were performed using eight probing directions instead of four, in order to compare the results from two equivalent pairs of collinear pulses, but which have different contacts used for the measurement of  $V_{xx}$ . Conclusions are hard to draw from the resulting plots so various additional plots are given to highlight details not visible when all current pulse directions are shown in one plot. Several additional figures are also included to highlight specific results.

Figure 7.6 contains plots of the  $\text{QMD}_\perp$  signals measured on the uniaxial

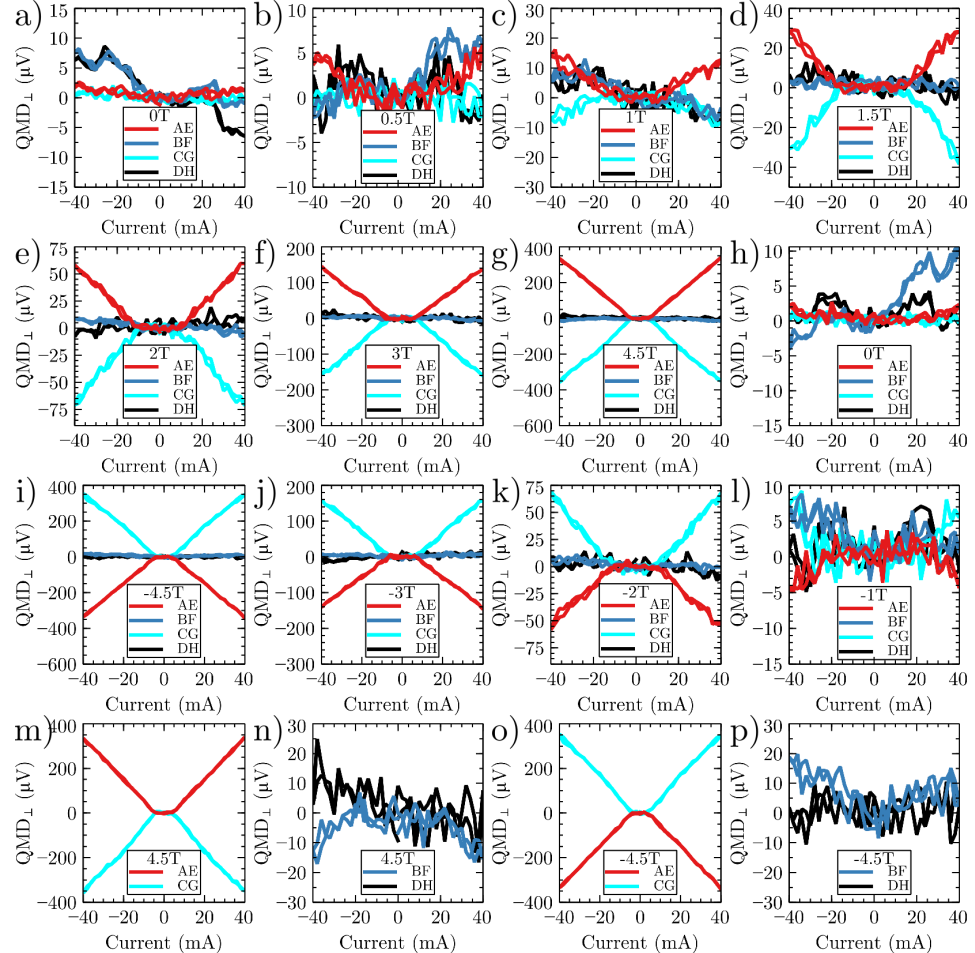


Figure 7.6: Plots of  $\text{QMD}_{\perp}$  signals of uniaxial Sample C, measured at 10 K with the field applied along the CG easy axis at various applied field strengths as shown by legend titles. (a-l) Contain plots of all four  $\text{QMD}_{\perp}$  directions in chronological order. (m-p) shows repeated plots of the 4.5 T (m-n) and -4.5 T (o-p) measurements where the signals which become very large (AE and CG, parallel and perpendicular to the applied field) are separated to show details in the smaller signals (BF and DH, diagonal to the field).

sample at various applied field strengths with the field applied along the easy axis, parallel to the CG pulsing direction. Below 1.5 T, there seems to be no quadratic behaviour and the signals are only remnants of noise or other changes in the system. This is probably because the anisotropy barrier is higher at low field strengths. At 1.5 T there seems to be a parabolic signal when pulsing parallel (CG) or perpendicular (AE) to the applied field direction, corresponding to pulses parallel or perpendicular to the easy axis. This is the sort of signal expected from QMD. As the field strength is increased, however, a new signal seems to appear in these arms, but only above a threshold current. As field is increased, the threshold current decreases and the gradient of the linear section of the signal increases drastically. The sign of this signal is reversed when the applied field is reversed, so it is antisymmetric with applied field. For clarity, Figs 7.6 (m-p) show the 4.5 T and -4.5 T results with the signals showing the large linear change above the threshold current separated from the signals lacking it. In these smaller signals there does not seem to be any strong parabolic dependence, although there is some hint in the blue lines, for pulsing along one of the diagonals (BF).

In order to illustrate the magnitude of these magnetoresistance changes, Fig. 7.7 contains the plots of the  $V_{yx}$  signals at +4.5 T, corresponding to the measurements in Fig. 7.6(g,m-n). The linear changes and thresholds are very visible in these plots when the current is applied parallel (CG) and perpendicular (AE) to the easy axis of the sample. The change is so large in (c) that the gradient changes sign.

Figure 7.8 contains plots of the  $QMD_{||}$  signals measured on the uniaxial sample. Delta-pulsing was conducted at various applied field strengths with the field applied along the CG easy axis. A similar behaviour to the  $V_{yx}$  measurements is observed in which a large linear region is present when the current is above some threshold, with the gradient of the linear region increasing with increasing field. The pulse directions in which the signals manifest, however, has changed to be perpendicular to the applied field (AE) and at 45° to the easy

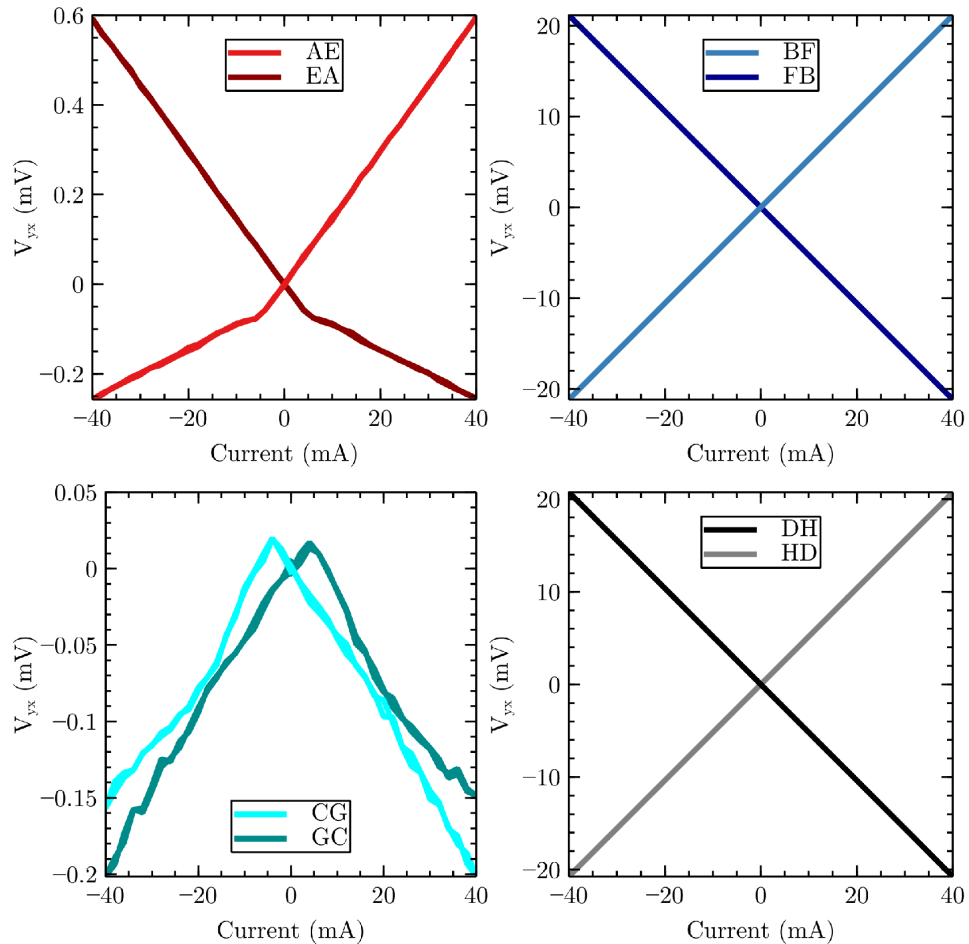


Figure 7.7: Plots of the  $V_{yx}$  values as a function of current for Sample C at 4.5 T along the CG easy axis where each plot contains the pairs of data summed to calculate the QMD signals shown in Fig. 7.6(g,m-n). Each pulsing direction is indicated by the legend in each plot.

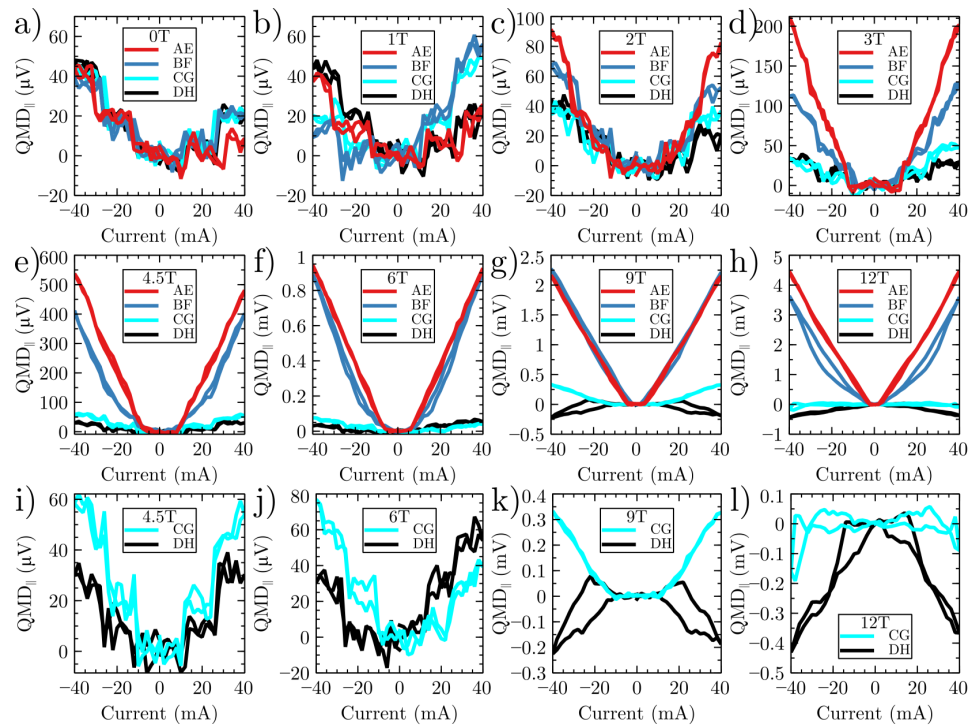


Figure 7.8: Plots of  $\text{QMD}_{\parallel}$  signals as a function of current with an external fields applied along the CG easy axis of Sample C with magnetic field strengths indicated by the titles of each legend. (a-h) Contain plots of all four QMD directions while (i-l) contain repeated plots with the large signals removed for clarity.

axis (BF). How it could be along only one diagonal and one lateral direction is puzzling. As well as the large linear signals, some complicated hysteretic behaviour is present in the other two pulsing directions (CG and DH), forming some kind of butterfly shape at 9 T and above, as highlighted in Fig 7.8(k-l).

Figure 7.9 contains plots of the  $V_{yx}$  signals for three different field directions set to 4.5 T (a,c-e,g-h) and one set to -4.5 T (b,f) in order to explore how the applied field direction affects which current directions the large winging signals appear along. The plots in (a-d) contain the signals for all four current directions while (e-h) contain only the arms which exhibit the smallest maximum signals, in order to adjust the scale for clarity. The results show that, for the field along the hard axis (AE), the threshold for the winging signals is too large or is not present. For all the other directions, the winging signals appear for current directions parallel and perpendicular to the applied field.

Figure 7.10 contains plots of the 12 T measurements corresponding to the field direction of Figure 7.9(d,h). Even at 12 T, applying the field along the hard axis did not manifest the winging signals, but did create butterfly hysteresis patterns in both  $\text{QMD}_\perp$  (a) and  $V_{yx}$  (c) for currents applied along the AE and CG directions. One large parabolic signal appears in  $\text{QMD}_\perp$  for when the current is applied along the BF direction, at  $45^\circ$  to the applied field direction. This dependence on both field amplitude and direction, and the dependence on current, suggests that this winging signal, whatever it is, can only be observed after spin flop. This could be because, after spin flop, the moments are near their maximum anisotropy energy and thus are in unfavourable positions and are unstable. If the origin was instead based on canting, then applying the field along the hard axis would manifest these signals, but it does not.

Figure 7.11 contains plots for delta-pulsing staircase sweeps measuring  $\text{QMD}_\perp$  using biaxial Sample E while applying increasing magnetic field strengths along the DH easy axis. The zero field appears to be a smaller version of the RTS results on the same sample, showing a parabolic dependence of the signals on current amplitude. The winging signals have opposing signs to each other, as

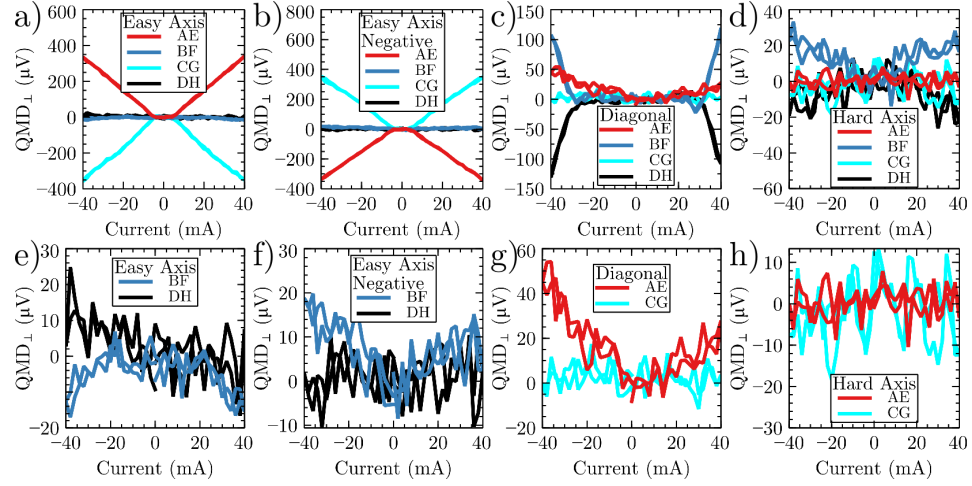


Figure 7.9: Plots of  $\text{QMD}_{\perp}$  signals as a function of applied current with an external field, measured using uniaxial Sample C. In (a-b,e-f) the field was applied along the CG easy axis, at +4.5 T (a,e) and -4.5 T (b,f) while (c,g) contains plots for the field applied along the DH diagonal direction and (d,h) are for the field along the AE hard axis. The plots in (a-d) contain all four current directions while (e-h) only show the smaller signals for clarity.

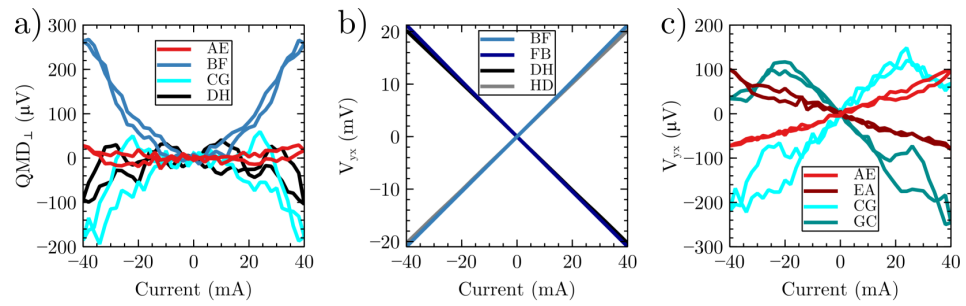


Figure 7.10: Plots of transverse signals as a function of applied current with an external field applied along the AE hard axis of Sample C with a field strength of 12 T. Plots in (a) contain all four current directions measuring  $\text{QMD}_{\perp}$  while (b) contains the larger gradient  $V_{yx}$  signals and (c) contains the smaller gradient  $V_{yx}$  signals.

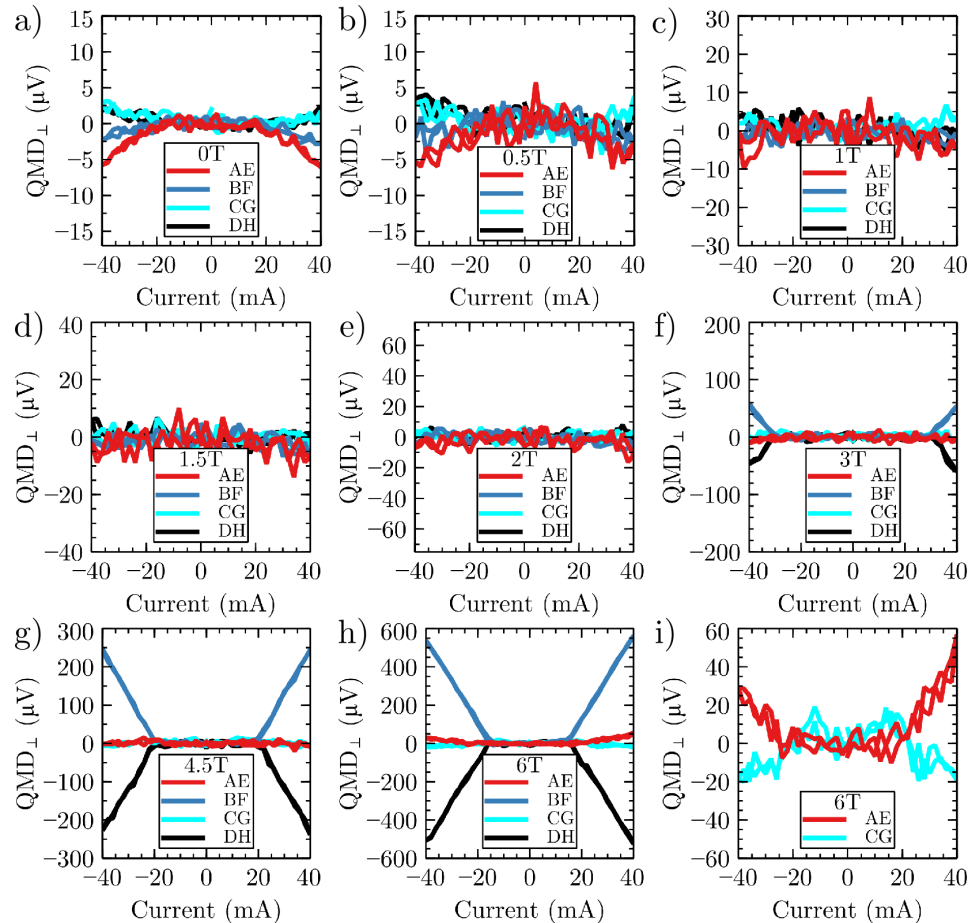


Figure 7.11: Plots of  $\text{QMD}_{\perp}$  signals as a function of applied current with an external field applied along the DH easy axis of biaxial Sample E at various field strengths as indicated by the legend title in each plot. (a-h) Contains plots of all four  $\text{QMD}_{\perp}$  directions in chronological order. The plots in (i) show repeated plots of the 4.5 T measurement in (g), after removing the large signals for clarity.

seen in the Sample C measurements contained in Fig. 7.6, and appear above 3 T. These signals manifested along the BF and DH current directions only, corresponding to current applied parallel to the easy axes of the sample. A large enough field was not reached before the electrical connections to the sample broke, so any hysteretic butterfly behaviour was not observed.

The field was then applied along the AE hard axis of Sample E while  $\text{QMD}_\perp$  was measured as a function of applied current with various applied field strengths. Figure 7.12 contains the resulting plots. At zero field, the signals still appear to be smaller versions of the RTS results, showing four small parabolic dependencies on the applied current, with two positive parabolas and two negative. As the field is increased, the large winging signals begin to appear at higher fields as seen before, but the non-winged signals seem to contain increasing amplitude parabolas, all of which are negative. The winging signals are larger and both positive in these data, but appear in the arms parallel and perpendicular to the applied field as before. At 9 T (i,o) and 16 T (j,p) the hysteretic behaviour in the smaller signals manifests as butterfly shaped hysteresis loops, similar to those seen in Fig. 7.8(k-l).

The samples were probed using eight probing directions in both parallel voltage and perpendicular voltage measurements such that the probing geometry was rotated by  $360^\circ$  around the device, where previously only a  $180^\circ$  was used. To clarify, this means that both AECG/EACG and EAGC/AEGC were probed for the perpendicular voltage measurements, which should be exactly the same, but for the parallel measurements BFCE becomes FBGA and so different arms are used to probe  $V_{xx}$  in opposing applied current directions. For the  $\text{QMD}_\perp$  measurements, each pair of equivalent probing directions were compared and showed no difference in signals. In the  $\text{QMD}_\parallel$  case, there were some interesting results. Figure 7.13 contains plots of the  $\text{QMD}_\parallel$  signals as a function of current, measured using Sample C with the field applied along the CG easy axis. The plots in (a) show all eight probing directions in one plot and (b-e) show each pair of antiparallel probing geometries, which were expected to be equivalent,

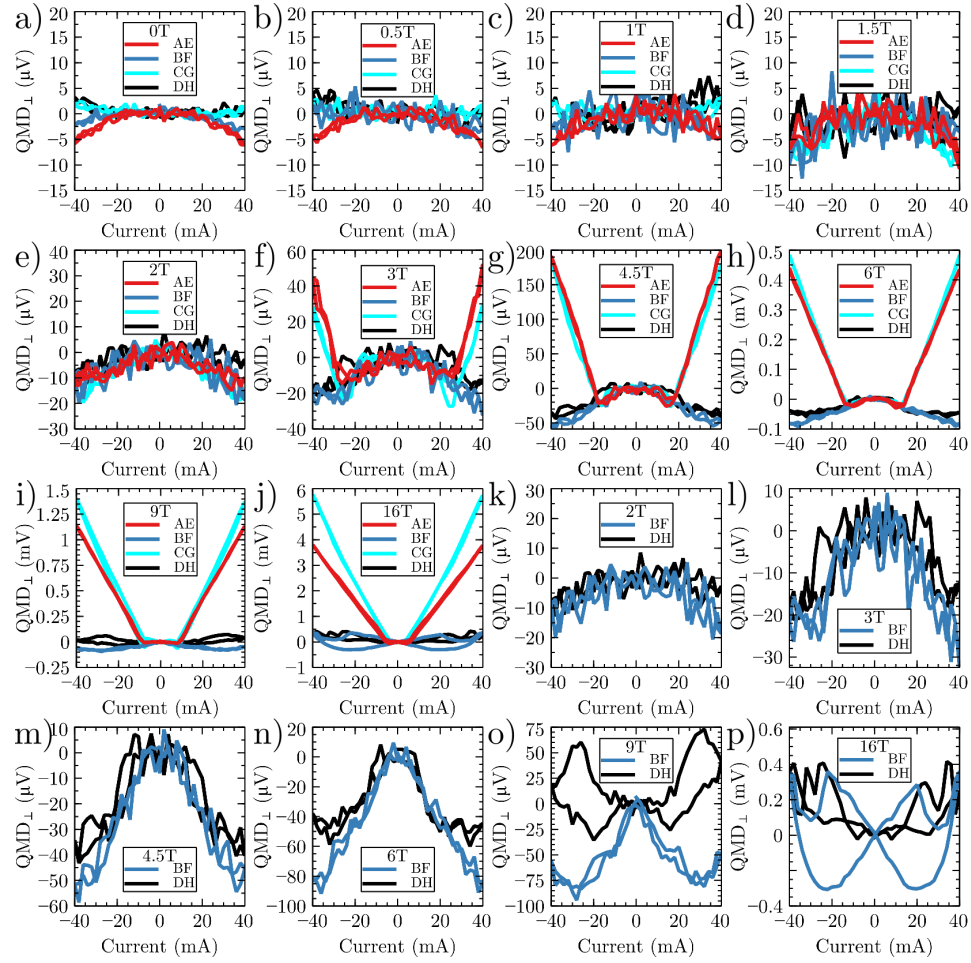


Figure 7.12: Plots of QMD<sub>⊥</sub> signals as a function of applied current with an external field applied along the AE hard axis of biaxial Sample E at various field strengths as indicated by the legend title in each plot. (a-h) Contains plots of all four QMD directions in chronological order. (i) shows repeated plots of the 4.5 T measurement, after removing the large signals for clarity. Please note that the scale of voltage units changes between (h) and (i), since the signal changes by 3 orders of magnitude.

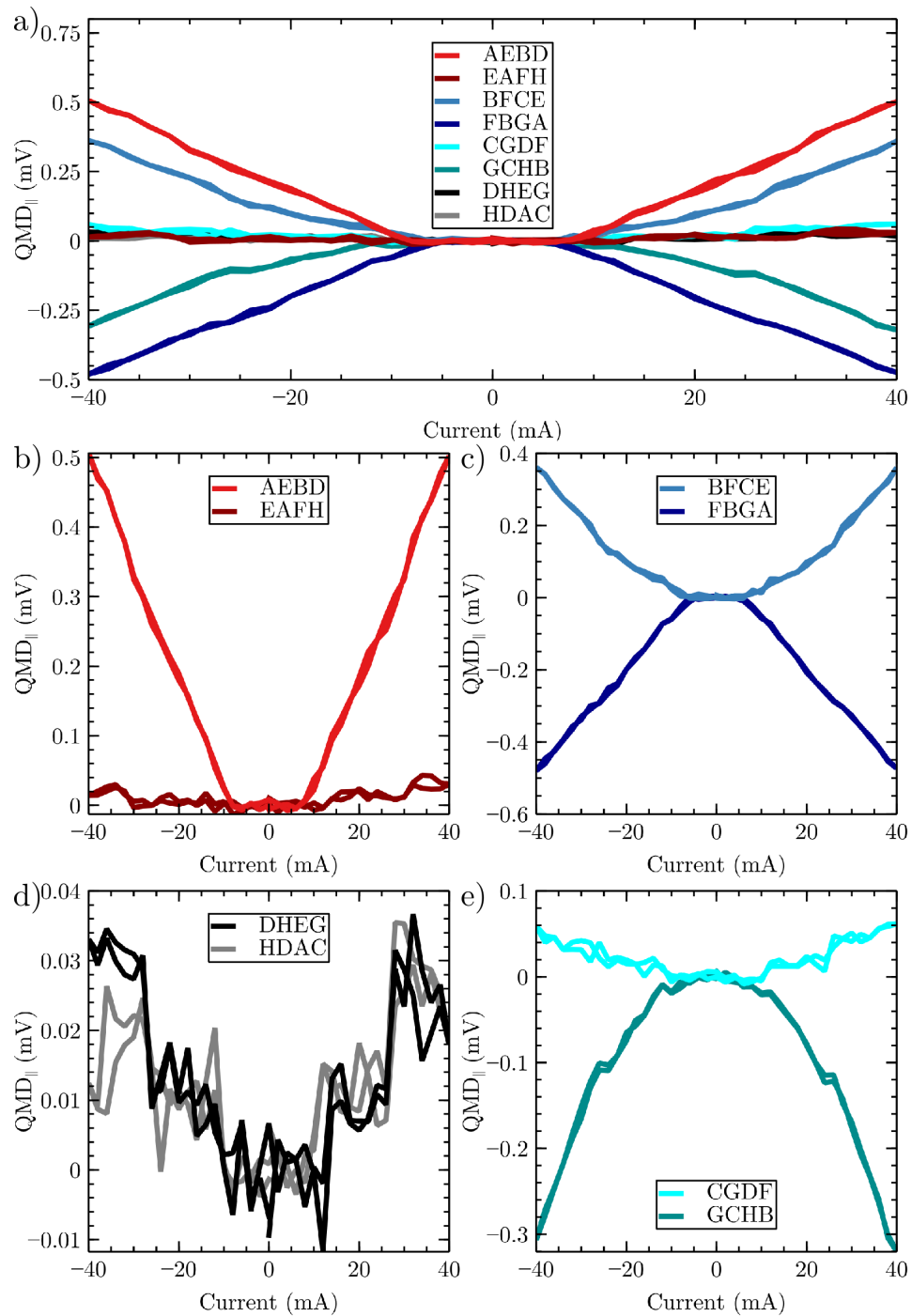


Figure 7.13: Plots of  $QMD_{||}$  signals as a function of applied current for eight geometries with an external field applied along the CG easy axis of uniaxial Sample C at a field strength of 4.5 T. (a) contains all eight plots while (b-e) contain pairs of signals with the current applied along the same axis of the sample with rotated probing geometry as indicated by the legends, which were expected to be antisymmetric.

although of opposite sign. It can be seen here that the winging signals only appear in four probing directions: AEBD, BFCE, FBGA and GCHB. Each of these winging signals has a partner of the same magnitude with opposite sign, namely the signal measured along AEBD is the negative of the signal measured along FBGA while BFCE and GCHB form the other pair. This is very puzzling because they are not pairs of antiparallel or perpendicular pulsing directions, but instead are rotations through inconsistent angles. In the line drawn from C to G is taken as the positive  $x$  direction, then the winging signals appear when the positive current direction is at angles of  $135^\circ$ ,  $180^\circ$ ,  $270^\circ$  and  $315^\circ$  to the  $x$ -axis, corresponding to FBGA, GCHB, AEBD and BFCE respectively.

### 7.2.3 Field Sweeps with Continuous High-Current Delta-Pulses

In order to better understand the dependence of applied field on the magnitudes of the winging signals, the same samples were used and pulse delta measurements with alternating sign, but constant amplitude, were continuously applied to the sample. The resulting  $V_{xx}$  and  $V_{yx}$  signals were measured as a function of applied field strength and converted to AMR resistance measurements by dividing by the applied current, analogous to the spin flop measurements performed in Section 3.2.2. For this, alternating pulses of  $\pm 40$  mA, the maximum current amplitude from the above measurements, were used with a delay of 100 ms between each pulse. Uniaxial Sample C is measured first, with the field along the easy axis. The probing current pulses were applied in two directions: first collinear with the applied field and then at  $45^\circ$  to the applied field. Next, biaxial Sample E is measured with the field along the hard axis and the current is applied collinear with the field.

Figure 7.14 contains plots for measurements conducted on uniaxial Sample C with magnetic field applied along the easy axis. Two probing directions were used: one with current perpendicular to the applied field (a-b) and the other at

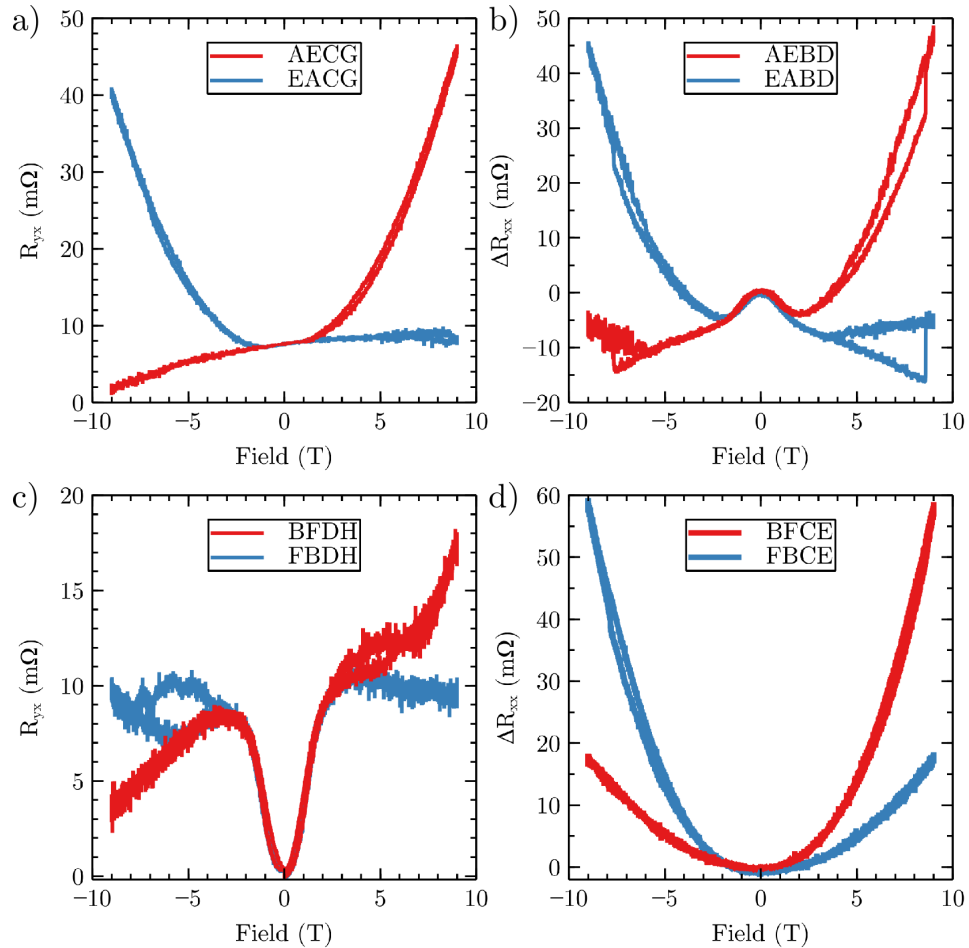


Figure 7.14: Plots of (a,c)  $R_{yx}$  and (b,d)  $\Delta R_{xx}$  as a function of applied field strength for a field applied along the CG easy axis of Sample C at a sample temperature of 12 K. The legend indicates the applied current and probing directions, in which current pulses were alternated between each direction with amplitudes of 40 mA in all cases.

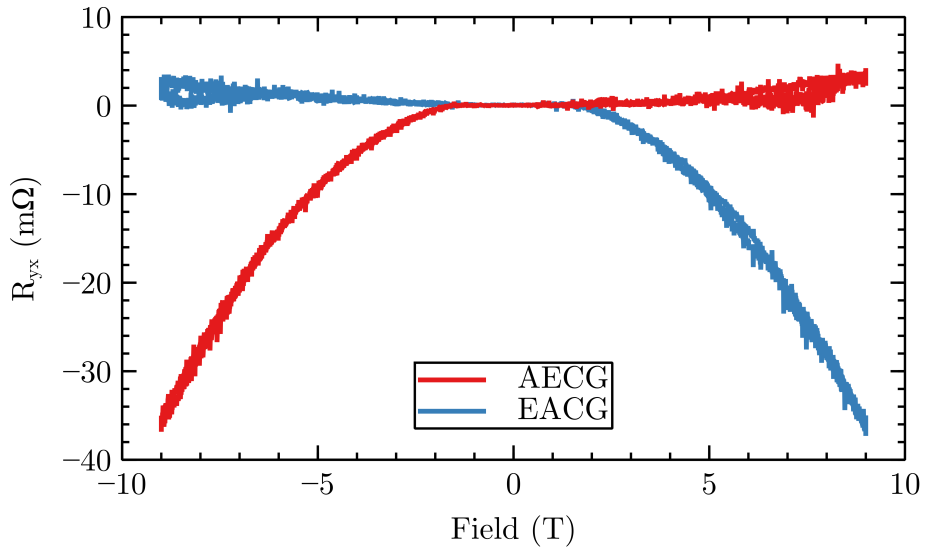


Figure 7.15: Plots of  $R_{yx}$  as a function of applied field strength for a field applied along the AE hard axis of Sample E at a sample temperature of 4 K. The legend indicates the applied current and probing directions, in which current pulses were alternated between each direction with amplitudes of 40 mA.

45° to the applied field (c-d). The plots in (a,c) show  $V_{yx}$  as a function of field strength and (b,d) contain the equivalent  $V_{xx}$  plots, in which the values are adjusted to be zero at zero field. When the current is applied parallel to the applied field, the separation between positive and negative voltages shows a large field dependence in both  $R_{yx}$  and  $R_{xx}$  ( $> 40$  mΩ at 9 T in both cases) and the sign of the separation changes when the sign of the applied field changes. When the probing pulses are applied diagonally, the separation is smaller in the  $R_{yx}$  case, and is no longer symmetric. Instead, the negative current pulses do not generate the separation, remaining almost constant with increasing field above the spin flop field, and instead only the positive current generates the deviation from constant value in the higher field measurements. The  $R_{xx}$  values, in contrast, are symmetric with the arm which deviates from constant value being swapped when the sign of the applied field is swapped. This highlights the strange symmetry observed when comparing the  $V_{yx}$  and  $V_{xx}$  measurements using delta-pulsing current staircases in Figs. 7.6 and 7.8.

Figure 7.15 contains the plots of  $V_{yx}$  as a function of applied field with

the field applied along a hard axis and collinear to the applied current pulse direction. These data show a similar magnitude of separation as the uniaxial results in Fig. 7.14(a,c) and the extent of deviation from a constant value is symmetric under the reversal of the field direction, however the arm which deviates from a constant value changes under this change in sign.

To better understand the directional dependence, the field sweeps in Section 7.2.3 should be conducted using all four probing directions to measure  $V_{yx}$  and  $V_{xx}$  in both materials. Instead of using 8-arm asterisk devices, simple hall bars should be used. Doing so should either eliminate, or prove the magnetic origin of, the asymmetry observed when changing which arms are used to measure  $V_{xx}$  in Fig. 7.13.

The base  $R_{xx}$  value is  $\approx 3 \Omega$  for Sample C and  $\approx 5 \Omega$  for Sample E. This means that the  $\approx 40 \text{ m}\Omega$  changes correspond to a normalised AMR signal of  $\sim 1\%$ , which is  $\approx 5$  times larger than the AMR changes measured in the same uniaxial material (Sample C) when using DC probing currents in Sec 3.3.2.

#### 7.2.4 Verifications

Several further investigations were conducted in order to isolate or eliminate possible origins of the signals experienced, both in the RTS measurements, and in the high field measurements. To ensure that the parabolic shapes from Fig. 7.5 were the result of the sample, and not systematic errors in the equipment, a delta-pulsing staircase sweep measurement was performed on a metallic resistor with a 2-wire resistance similar to the devices used, with a smaller resistor added to enable a similar 4-wire signal. The resulting signals showed no difference between pulses in opposing polarity and therefore confirmed that the device is generating the quadratic QMD signal. A more robust test would be to measure a thin film metallic sample with the same geometry as used in this chapter but this has not been performed yet.

In order to confirm that the signals presented were not dependent on the

prior pulses, the order of the pulses was changed and the delay between pulses was changed. Instead of using a staircase sweep as described previously, the pulses were also applied with one of each polarity at a given current amplitude before increasing the amplitude. The field step measurements were repeated using this alternative probing method and led to no changes in the resulting signals. The pulse trains were sent with three different delays between each pulse, 1 s, 0.1 s and 1 ms. These also had no effect on the resulting signals. This is evidence that any changes caused by the pulses are instigated by each pulse individually and are not dependent on heating from prior pulses.

An attempt was made to measure delta-pulsing at a temperature close to the Néel temperature and then above the Néel temperature, hoping that the signal would disappear when the sample was no longer magnetic. Unfortunately, the temperature stability in the equipment used to reach such temperatures was too poor and the QMD signals were drowned out by thermal changes in the system, even at temperatures much lower than the Néel temperature. It would be valuable to try and create a more stable high temperature system in order to facilitate this measurement. Instead of this ideal measurement, delta-pulsing was performed in the RTS at temperatures of -5 to 40 °C in steps of 5 °C. Each of these measurements showed no discernible difference in amplitude or shape of the signals, indicating minimal dependence of the QMD signals on temperature when near room temperature, so long as the temperature is constant throughout the measurement. Any changes in base resistance during the measurement would, naturally, lead to large QMD signals because of the way the QMD signal is obtained from the difference between two measurements.

In order to avoid any mixing of parallel and perpendicular signals as a result of device geometry, an L-shaped hall bar was fabricated on a piece of Sample C with arm widths of 100 µm. These were measured using staircase delta-pulsing in the room temperature system. These devices show no parabolic signal and were destroyed at lower current amplitudes than expected. If the experiment is to be repeated, the maximum current should be increased more carefully to

avoid destroying the device.

In the spin flopped state, the energetics of an uniaxial system (see Section 2.6) are such that the moments are at minimum energy from the Zeeman term, roughly unchanged in the exchange term and are at the maximum energy from the anisotropy term (they are parallel to the hard axes). This contribution from the anisotropy term may lead to the destabilisation of domain walls, leading to increased domain wall motion under the influence of electrical pulses. This is the only possible explanation for origin of the signals, but the exact consequence of such destabilisation requires further investigation. If this is instead considered for the biaxial sample, however, it is not clear how the spin flop field allows for the observed signals. It is not readily apparent how domain wall motion affects the measured signals, so more consideration and investigation is necessary to draw better conclusions.

### 7.3 Discussion and Conclusions

Delta-pulsing has been demonstrated as an effective way to enable transport measurements at higher currents without damaging devices. At room temperature, some parabolic signal was present in all measured CuMnAs samples with a clear difference in the symmetry of these parabolas between the uniaxial and biaxial sample. In trying to observe the magnetic origin of the parabolas, the delta-pulsing measurements were conducted in the presence of high magnetic fields inside a cryostat. By using these high current probing pulses in the high field, attempts to measure the difference between opposing polarity pulses has led to the discovery of some signal in CuMnAs samples with unknown origin.

The new signal manifests as sudden change in the gradient of the current-voltage characteristics of magnetoresistance measurements above some threshold current which is dependent on applied magnetic field strength. This threshold appears to be codependent on external magnetic field strength and applied current density with the gradient becoming steeper and the current threshold

becoming smaller at higher fields. Several studies were performed in attempts to understand the symmetry and behaviour of these signals with reference to the magnetic ordering in the CuMnAs samples, but the true nature still remains hidden. These studies have illustrated that this new signal must be magnetic in some way due to its dependence on both applied current and external magnetic field strength.

The further investigations have been suggested: measuring a thin, non-magnetic, metallic film with a similar resistivity to the CuMnAs samples as verification that the signals are a result of CuMnAs and not something else in the system; measuring the signals below and above the Néel temperature in both zero field and high field measurements; repeating the field sweep measurements using pulses with alternating sign to probe  $R_{yx}$  and  $R_{xx}$  using more field and current direction combinations; and measuring the signal using L-shaped hall bars instead of 8-arm asterisk devices to reduce contributions to observed resistance signals from device geometry. Meanwhile, simulations of QMD and the effects of domain wall motion should be conducted to further progress understanding of the possible causes for the signal.

Although QMD was not measured conclusively in CuMnAs, the applications of delta-pulsing as a transport measurement technique were made clear. The resulting new signals, although puzzling, could be very interesting, especially when the normalised resistance change is as large at 10 % at 9 T. With further study and some progression in understanding, there is hope for determining the magnetic ordering of a sample using high current delta-pulsing as independent method for determination on the Néel vector of an antiferromagnetic sample.

# Chapter 8

## Concluding Remarks

The thesis began by summarising magnetism and the field of spintronics before bringing the reader up to speed on some recent developments in antiferromagnetic spintronics. It proceeded by introducing some vital spintronic effects present in AFMs for which CuMnAs has been used as a tool to study. The rest of the thesis aimed to make progress towards convenient lab-based characterisation techniques capable of extracting more information from AFM spintronic devices with various levels of success.

The studies in Chapter 3 aimed to determine the extent of spin flop in CuMnAs thin films and to test the limit of thinness in neutron diffraction. To observe this, neutron diffraction was conducted on two uniaxial thin films of CuMnAs, one 20 nm and one 45 nm thick. A purely magnetic neutron diffraction peak's amplitude was monitored as the applied field was increased in steps up to 8 T. Spin flop was detected as a decrease in these peak amplitudes since the moments rotate from a direction allowing contribution to the diffraction, into a direction that does not. The resulting reduction was found to demonstrate a rotation of 98 % of the moments in a 45 nm uniaxial sample of CuMnAs and > 90 % in the 20 nm film. The remaining moments were assumed to be the result of domain walls and pinned sites due to defects. Overall, neutron diffraction was shown to be a useful tool in probing manipulations in AFM thin films as thin as 20 nm. This is possible in any crystal with the required symmetry

and which can experience a sustainable change to magnetic structure. A good agreement was found between the neutron diffraction data and an electronic transport measurement utilising anisotropic magnetoresistance, indicating that both techniques are effective, though for a quantitative measurement of spin flop reorientation, AMR is insufficient.

Chapter 4 described the use of ASOPS to enable rapid characterisation of the Néel vector, and determined whether a sample was uniaxial and biaxial, in CuMnAs films epitaxially grown on GaP(001) and GaAs(001) substrates. This was done by detecting pump-induced changes in the linear polarisation angle of reflected or transmitted light. These studies have demonstrated ASOPS as a benchtop technique capable of characterising CuMnAs samples grown on GaP(001) and GaAs(001) substrates in a matter of hours without the need for facilities, cryogens or high magnetic fields. The same transmission mode polarisation angle changes were detected in delay line pump probe to detect the reorientation of the Néel vector of moments undergoing spin flop in a CuMnAs sample grown on GaP(001).

Besides the ability to measure the Néel vector orientation, pump probe techniques may be capable of detecting dynamic changes to the magnetic moments. The ability to measure changes to magnetisation with high temporal resolution may mean it is possible to observe antiferromagnetic resonance by tilting the magnetic moment of CuMnAs slightly out of plane and using pump probe to detect the relaxation using THz spectroscopy. In order to do this, the sample must have a large magnetic field applied at an angle to the anisotropy plane of the sample such that a pump pulse would demagnetise the material enough to destabilise the moment such that it points out of the plane. As it remagnetises, the moment should precess from parallel to the field to relax back to the easy axis, detectable as an oscillation of the outgoing polarisation angle as the Néel vector precesses.

The studies in Chapter 5 aimed to determine size of the elastic constants of CuMnAs thin films using optical pump probe techniques. In order to find these,

the non-vanishing elastic constants present in tetragonal CuMnAs were found to be  $c_{11}$ ,  $c_{33}$ ,  $c_{12}$ ,  $c_{13}$ ,  $c_{44}$  and  $c_{66}$ . Three  $\approx 230$  nm layers of CuMnAs were grown on different substrates such that the angle between the CuMnAs c-axis and the substrate surface normal were achieved. This allowed for one measurement of  $c_{33}$  and the excitement of four modes containing combinations of  $c_{13}$ ,  $c_{44}$  and  $c_{66}$ . Pump-probe asynchronous optical sampling was used to measure the round trip time of optically induced strain waves which reflect off the substrate-CuMnAs interface back to the surface which are detected as a change in reflectivity. The speed of sound on the typical substrate yielded a value of  $c_{33} = 146 \pm 12$  GPa. The constants measured using the high-index samples were found to be  $c_{11} = 37 \pm 1$  GPa,  $c_{44} = 73 \pm 7$  GPa and  $c_{13} = -40 \pm 6$  GPa or  $c'_{13} = -104 \pm 7$  GPa where the final constant had two possible negative values, which is surprising. In order to corroborate these values and to measure the other two elastic constants, the choice between using a nano indenter and fabricating gratings in order to generate and detect surface acoustic waves must be made, and the appropriate measurements and analysis must be conducted.

Chapter 6 described the design, manufacture and use of a system for room temperature transport measurements with precise control of the temperature while keeping the sample in a vacuum. A vacuum chamber was designed by the author which enabled a peltier device to control the temperature of a sample at any temperature within the range of  $-8$  °C from ambient temperature of  $22$  °C and up to  $60$  °C, with a stability of  $\pm 5$  mK at all temperatures in this range. The vacuum chamber can be evacuated down to  $10^{-8}$  hPa. The resulting system was used to perform some switching experiments as a demonstration of the need for temperature control near room temperature. The system has since become a ubiquitous tool for Nottingham's FM and AFM spintronics research. The ability to place the sample within the bore of a magnet is attractive for many spintronic applications. In order to develop a variant of the RTS capable of this, the means of changing samples must be considered carefully to make sure that it is convenient enough while also making good thermal contact.

The studies in Chapter 7 aimed to develop a high amplitude, short duration pulsed electrical transport technique aiming to unlock the antisymmetric second order component of AMR changes from NSOT. The shortness of the pulse, and consequent low energy output of the pulse, allows access to higher currents than are accessible with DC or AC measurements. This part was a success and led to very little temperature change in the devices when used in the system described in Chapter 6. While trying to induce spin flop and detect the change in the detected signal, the combination of high current amplitudes and high magnetic field strengths lead to the appearance of large changes in the AMR signal which were not observed before. Attempts to determine the origin of these signals is so far inconclusive but the dependence on the amplitude of the current and on the strength of the applied magnetic field strongly suggest that it is magnetic in origin and the large detected signal sizes imply that the signal may be of use if its origin can be found.

In order to discover the origins of the new signals, a simulation to explore the dependence of the effect various parameters should be developed while more measurements of the QMD signals should be conducted. In order to develop the simulation, the effective fields used to derive the QMD signal should be considered more robustly and should take into account anisotropy and exchange fields. Using hall bars instead of asterix shaped devices would reduce the effects of fabrication asymmetries and may improve the reproducibility of the longitudinal QMD signals when the probing contacts are changes to the other side of the bar. Performing more in-field measurements with more field directions and strengths, possibly on more CuMnAs samples should be performed. A non-magnetic metallic film with similar resistance to the CuMnAs devices should be measured in the same way. This would demonstrate that the measured signals require the magnetic ordering to be present.

In summary, the demonstration of neutron diffraction as a means to detect spin flop has shown the extent of reorientation from a magnetic field is large and occurs throughout the material. This provides additional confidence when

using spin flop as a tool when testing other techniques. The development of the room temperature vacuum system has already proved its worth in other studies within the group. The ability to detect spin flop using the Voigt effect shows promise for magneto-optical techniques capable of imaging domain structures using a benchtop technique. Four of the elastic constants were measured using the pump probe technique which, with corroborating works, will increase the accuracy of magnetostrictive studies in CuMnAs. The newly detected large signal in high current, high field pulsing measurements is promising as a means to discover some new effect but until the origin is determined, it remains a novel side effect of an attempt to detect a different effect.

Overall, the works contained have made progress towards benchtop techniques capable of characterising and imaging AFM magnetic structure and have detected a new form of magnetic signal. With the suggested further studies, the ability to easily and cheaply characterise AFMs should become ever closer to reality.

# Bibliography

- [1] S. Blundell, “Magnetism in condensed matter,” 2003.
- [2] W. Wolf, “Ferrimagnetism,” *Reports on Progress in Physics*, vol. 24, no. 1, p. 212, 1961.
- [3] S. K. Kim, G. S. Beach, K.-J. Lee, T. Ono, T. Rasing, and H. Yang, “Ferrimagnetic spintronics,” *Nature materials*, vol. 21, no. 1, pp. 24–34, 2022.
- [4] J. Mydosh, “Spin glasses: redux: an updated experimental/materials survey,” *Reports on Progress in Physics*, vol. 78, no. 5, p. 052501, 2015.
- [5] G. Ju, Y. Peng, E. K. Chang, Y. Ding, A. Q. Wu, X. Zhu, Y. Kubota, T. J. Klemmer, H. Amini, L. Gao *et al.*, “High density heat-assisted magnetic recording media and advanced characterization—Progress and challenges,” *IEEE Transactions on Magnetics*, vol. 51, no. 11, pp. 1–9, 2015.
- [6] R. B. Goldfarb, B. Dieny, and K.-J. Lee, *Introduction to magnetic random-access memory*. John Wiley & Sons, 2016.
- [7] S. Bhatti, R. Sbiaa, A. Hirohata, H. Ohno, S. Fukami, and S. Piramanayagam, “Spintronics based random access memory: a review,” *Materials Today*, vol. 20, no. 9, pp. 530–548, 2017.
- [8] E. Gomonay and V. Loktev, “Spintronics of antiferromagnetic systems,” *Low Temperature Physics*, vol. 40, no. 1, pp. 17–35, 2014.
- [9] O. Gomonay, T. Jungwirth, and J. Sinova, “Concepts of antiferromagnetic spintronics,” *physica status solidi (RRL)–Rapid Research Letters*, vol. 11, no. 4, p. 1700022, 2017.
- [10] D. Li, Y. Haga, H. Shida, T. Suzuki, H. Fukuma, T. Kasuya, R. Akimoto, and M. Kobayashi, “Susceptibility and specific heat of EuSe,” *Journal of Alloys and Compounds*, vol. 219, no. 1-2, pp. 211–214, 1995.
- [11] J. Lamazares, F. Gonzalez-Jimenez, E. Jaimes, L. D’Onofrio, R. Iraldi, G. Sanchez-Porras, M. Quintero, J. Gonzalez, J. Woolley, and G. Lamarche, “Magnetic, transport, X-ray diffraction and Mössbauer measurements on CuFeSe<sub>2</sub>,” *Journal of Magnetism and Magnetic Materials*, vol. 104, pp. 997–998, 1992.

- [12] B. G. Park, J. Wunderlich, X. Martí, V. Holý, Y. Kurosaki, M. Yamada, H. Yamamoto, A. Nishide, J. Hayakawa, H. Takahashi *et al.*, “A spin-valve-like magnetoresistance of an antiferromagnet-based tunnel junction,” *Nature materials*, vol. 10, no. 5, pp. 347–351, 2011.
- [13] A. J. Devasahayam and M. H. Kryder, “Biasing materials for spin-valve read heads,” *IEEE transactions on magnetics*, vol. 35, no. 2, pp. 649–654, 1999.
- [14] B. Kocaman and N. Akdoğan, “Reduction of shunt current in buffer-free IrMn based spin-valve structures,” *Journal of Magnetism and Magnetic Materials*, vol. 456, pp. 17–21, 2018.
- [15] L. Néel, “Propriétés magnétiques des ferrites; ferrimagnétisme et antiferromagnétisme,” in *Annales de physique*, vol. 12, no. 3, 1948, pp. 137–198.
- [16] ——, “Magnetism and local molecular field,” *Science*, vol. 174, no. 4013, pp. 985–992, 1971.
- [17] J. Lenz and S. Edelstein, “Magnetic sensors and their applications,” *IEEE Sensors journal*, vol. 6, no. 3, pp. 631–649, 2006.
- [18] B. Diény, “Giant magnetoresistance in spin-valve multilayers,” *Journal of Magnetism and Magnetic Materials*, vol. 136, no. 3, pp. 335–359, 1994.
- [19] C. Chappert, A. Fert, and F. N. Van Dau, “The emergence of spin electronics in data storage,” *Nature materials*, vol. 6, no. 11, pp. 813–823, 2007.
- [20] Y. Lee, J. Hayakawa, S. Ikeda, F. Matsukura, and H. Ohno, “Effect of electrode composition on the tunnel magnetoresistance of pseudo-spin-valve magnetic tunnel junction with a MgO tunnel barrier,” *Applied physics letters*, vol. 90, no. 21, p. 212507, 2007.
- [21] W. Rudziński and J. Barnaś, “Tunnel magnetoresistance in ferromagnetic junctions: Tunneling through a single discrete level,” *Physical Review B*, vol. 64, no. 8, p. 085318, 2001.
- [22] S. Yuasa and D. Djayaprawira, “Giant tunnel magnetoresistance in magnetic tunnel junctions with a crystalline MgO (0 0 1) barrier,” *Journal of Physics D: Applied Physics*, vol. 40, no. 21, p. R337, 2007.
- [23] J. Železný, P. Wadley, K. Olejník, A. Hoffmann, and H. Ohno, “Spin transport and spin torque in antiferromagnetic devices,” *Nature Physics*, vol. 14, no. 3, pp. 220–228, 2018.
- [24] J. Železný, H. Gao, K. Výborný, J. Zemen, J. Mašek, A. Manchon, J. Wunderlich, J. Sinova, and T. Jungwirth, “Relativistic Néel-order fields induced by electrical current in antiferromagnets,” *Physical review letters*, vol. 113, no. 15, p. 157201, 2014.
- [25] P. Wadley, B. Howells, J. Železný, C. Andrews, V. Hills, R. P. Campion, V. Novák, K. Olejník, F. Maccherozzi, S. Dhesi *et al.*, “Electrical switching of an antiferromagnet,” *Science*, vol. 351, no. 6273, pp. 587–590, 2016.

- [26] K. Olejník, V. Schuler, X. Martí, V. Novák, Z. Kašpar, P. Wadley, R. P. Campion, K. W. Edmonds, B. L. Gallagher, J. Garcés *et al.*, “Antiferromagnetic CuMnAs multi-level memory cell with microelectronic compatibility,” *Nature communications*, vol. 8, no. 1, pp. 1–7, 2017.
- [27] P. Wadley, S. Reimers, M. J. Grzybowski, C. Andrews, M. Wang, J. S. Chauhan, B. L. Gallagher, R. P. Campion, K. W. Edmonds, S. S. Dhesi *et al.*, “Current polarity-dependent manipulation of antiferromagnetic domains,” *Nature nanotechnology*, vol. 13, no. 5, pp. 362–365, 2018.
- [28] K. Olejník, T. Seifert, Z. Kašpar, V. Novák, P. Wadley, R. P. Campion, M. Baumgartner, P. Gambardella, P. Němec, J. Wunderlich *et al.*, “Terahertz electrical writing speed in an antiferromagnetic memory,” *Science advances*, vol. 4, no. 3, p. eaar3566, 2018.
- [29] J. J. Heitz, L. Nádvorník, V. Balos, Y. Behovits, A. L. Chekhov, T. S. Seifert, K. Olejník, Z. Kašpar, K. Geishendorf, V. Novák *et al.*, “Optically Gated Terahertz-Field-Driven Switching of Antiferromagnetic CuMnAs,” *Physical Review Applied*, vol. 16, no. 6, p. 064047, 2021.
- [30] Z. Kašpar, M. Surýnek, J. Zubáč, F. Krizek, V. Novák, R. P. Campion, M. S. Wörnle, P. Gambardella, X. Marti, P. Němec *et al.*, “Quenching of an antiferromagnet into high resistivity states using electrical or ultrashort optical pulses,” *Nature Electronics*, vol. 4, no. 1, pp. 30–37, 2021.
- [31] M. Wörnle, P. Welter, Z. Kašpar, K. Olejník, V. Novák, R. Campion, P. Wadley, T. Jungwirth, C. Degen, and P. Gambardella, “Current-induced fragmentation of antiferromagnetic domains,” *arXiv preprint arXiv:1912.05287*, 2019.
- [32] M. Grzybowski, P. Wadley, K. Edmonds, R. Beardsley, V. Hills, R. Campion, B. Gallagher, J. S. Chauhan, V. Novak, T. Jungwirth *et al.*, “Imaging current-induced switching of antiferromagnetic domains in CuMnAs,” *Physical review letters*, vol. 118, no. 5, p. 057701, 2017.
- [33] T. Shiino, S.-H. Oh, P. M. Haney, S.-W. Lee, G. Go, B.-G. Park, and K.-J. Lee, “Antiferromagnetic domain wall motion driven by spin-orbit torques,” *Physical review letters*, vol. 117, no. 8, p. 087203, 2016.
- [34] O. Gomonay, T. Jungwirth, and J. Sinova, “High antiferromagnetic domain wall velocity induced by Néel spin-orbit torques,” *Physical review letters*, vol. 117, no. 1, p. 017202, 2016.
- [35] V. Saidl, P. Němec, P. Wadley, V. Hills, R. Campion, V. Novák, K. Edmonds, F. Maccherozzi, S. Dhesi, B. Gallagher *et al.*, “Optical determination of the Néel vector in a CuMnAs thin-film antiferromagnet,” *Nature Photonics*, vol. 11, no. 2, pp. 91–96, 2017.
- [36] I. Gray, T. Moriyama, N. Sivadas, G. M. Stiehl, J. T. Heron, R. Need, B. J. Kirby, D. H. Low, K. C. Nowack, D. G. Schlom *et al.*, “Spin Seebeck imaging of spin-torque switching in antiferromagnetic Pt/NiO heterostructures,” *Physical Review X*, vol. 9, no. 4, p. 041016, 2019.

- [37] T. Janda, J. Godinho, T. Ostatnický, E. Pfitzner, G. Ulrich, A. Hoehl, S. Reimers, Z. Šobáň, T. Metzger, H. Reichlova *et al.*, “Magneto-Seebeck microscopy of domain switching in collinear antiferromagnet CuMnAs,” *Physical Review Materials*, vol. 4, no. 9, p. 094413, 2020.
- [38] V. Barthélémy, C. Colin, H. Mayaffre, M.-H. Julien, and D. Givord, “Revealing the properties of Mn<sub>2</sub>Au for antiferromagnetic spintronics,” *Nature communications*, vol. 4, no. 1, p. 2892, 2013.
- [39] S. Y. Bodnar, L. Šmejkal, I. Turek, T. Jungwirth, O. Gomonay, J. Sinova, A. Sapozhnik, H.-J. Elmers, M. Kläui, and M. Jourdan, “Writing and reading antiferromagnetic Mn<sub>2</sub>Au by Néel spin-orbit torques and large anisotropic magnetoresistance,” *Nature communications*, vol. 9, no. 1, p. 348, 2018.
- [40] X. Chen, X. Zhou, R. Cheng, C. Song, J. Zhang, Y. Wu, Y. Ba, H. Li, Y. Sun, Y. You *et al.*, “Electric field control of Néel spin-orbit torque in an antiferromagnet,” *Nature materials*, vol. 18, no. 9, pp. 931–935, 2019.
- [41] X. Zhou, J. Zhang, F. Li, X. Chen, G. Shi, Y. Tan, Y. Gu, M. Saleem, H. Wu, F. Pan *et al.*, “Strong orientation-dependent spin-orbit torque in thin films of the antiferromagnet Mn 2 Au,” *Physical Review Applied*, vol. 9, no. 5, p. 054028, 2018.
- [42] M. Meinert, D. Graulich, and T. Matalla-Wagner, “Electrical switching of antiferromagnetic Mn 2 Au and the role of thermal activation,” *Physical Review Applied*, vol. 9, no. 6, p. 064040, 2018.
- [43] S. Y. Bodnar, M. Filianina, S. Bommanaboyena, T. Forrest, F. Maccherozzi, A. Sapozhnik, Y. Skourski, M. Kläui, and M. Jourdan, “Imaging of current induced Néel vector switching in antiferromagnetic Mn 2 Au,” *Physical Review B*, vol. 99, no. 14, p. 140409, 2019.
- [44] S. Y. Bodnar, Y. Skourski, O. Gomonay, J. Sinova, M. Kläui, and M. Jourdan, “Magnetoresistance effects in the metallic antiferromagnet mn 2 au,” *Physical Review Applied*, vol. 14, no. 1, p. 014004, 2020.
- [45] M. Wang, C. Andrews, S. Reimers, O. Amin, P. Wadley, R. Campion, S. Poole, J. Felton, K. Edmonds, B. Gallagher *et al.*, “Spin flop and crystalline anisotropic magnetoresistance in CuMnAs,” *Physical Review B*, vol. 101, no. 9, p. 094429, 2020.
- [46] J. Godinho, H. Reichlová, D. Kriegner, V. Novák, K. Olejník, Z. Kašpar, Z. Šobáň, P. Wadley, R. Campion, R. Otxoa *et al.*, “Electrically induced and detected Néel vector reversal in a collinear antiferromagnet,” *Nature communications*, vol. 9, no. 1, p. 4686, 2018.
- [47] P. Wadley, V. Hills, M. Shahedkhah, K. Edmonds, R. Campion, V. Novák, B. Ouladdiaf, D. Khalyavin, S. Langridge, V. Saidl *et al.*, “Antiferromagnetic structure in tetragonal CuMnAs thin films,” *Scientific reports*, vol. 5, no. 1, pp. 1–6, 2015.

- [48] P. Wadley, V. Novák, R. Campion, C. Rinaldi, X. Martí, H. Reichlová, J. Železný, J. Gazquez, M. Roldan, M. Varela *et al.*, “Tetragonal phase of epitaxial room-temperature antiferromagnet CuMnAs,” *Nature communications*, vol. 4, no. 1, pp. 1–6, 2013.
- [49] X. Zhang, Q. Liu, J.-W. Luo, A. J. Freeman, and A. Zunger, “Hidden spin polarization in inversion-symmetric bulk crystals,” *Nature Physics*, vol. 10, no. 5, pp. 387–393, 2014.
- [50] G. Wastlbauer and J. A. C. Bland\*, “Structural and magnetic properties of ultrathin epitaxial Fe films on GaAs (001) and related semiconductor substrates,” *Advances in physics*, vol. 54, no. 2, pp. 137–219, 2005.
- [51] F. Krizek, Z. Kašpar, A. Vetushka, D. Kriegner, E. M. Fiordaliso, J. Michalička, O. Man, J. Zubáč, M. Brajer, V. A. Hills *et al.*, “Molecular beam epitaxy of CuMnAs,” *Physical Review Materials*, vol. 4, no. 1, p. 014409, 2020.
- [52] F. Máca, J. Kudrnovský, P. Baláž, V. Drchal, K. Carva, and I. Turek, “Tetragonal CuMnAs alloy: Role of defects,” *Journal of Magnetism and Magnetic Materials*, vol. 474, pp. 467–471, 2019.
- [53] S. Reimers, D. Kriegner, O. Gomonay, D. Carbone, F. Krizek, V. Novák, R. P. Campion, F. Maccherozzi, A. Björling, O. J. Amin *et al.*, “Defect-driven antiferromagnetic domain walls in CuMnAs films,” *Nature communications*, vol. 13, no. 1, pp. 1–7, 2022.
- [54] F. Krizek, S. Reimers, Z. Kašpar, A. Marmodoro, J. Michalička, O. Man, A. Edström, O. J. Amin, K. W. Edmonds, R. P. Campion *et al.*, “Atomically sharp domain walls in an antiferromagnet,” *Science advances*, vol. 8, no. 13, p. eabn3535, 2022.
- [55] S. Reimers, O. Gomonay, O. J. Amin, F. Krizek, L. X. B. Y. Lytvynenko, S. Poole, R. P. Campion, V. Novák, F. Maccherozzi, D. Carbone, A. Björling, Y. Niu, E. Golias, D. Kriegner, J. Sinova, M. Kläui, M. Jourdan, S. S. Dhesi, K. W. Edmonds, and P. Wadley, “Magnetic domain engineering in antiferromagnetic CuMnAs and Mn<sub>2</sub>Au devices,” 2023.
- [56] R. O’Handley, *Modern Magnetic Materials: Principles and Applications*. Wiley, 1999. [Online]. Available: <https://books.google.co.uk/books?id=RKV1QgAACAAJ>
- [57] O. Amin, S. Poole, S. Reimers, L. Barton, F. Maccherozzi, S. Dhesi, V. Novák, F. Křížek, J. Chauhan, R. Campion *et al.*, “Antiferromagnetic half-skyrmions electrically generated and controlled at room temperature,” *arXiv preprint arXiv:2207.00286*, 2022.
- [58] S. F. Poole, L. X. Barton, M. Wang, P. Manuel, D. Khalyavin, S. Langridge, K. W. Edmonds, R. P. Campion, V. Novák, and P. Wadley, “Probing the manipulation of antiferromagnetic order in CuMnAs films using neutron diffraction,” *Applied Physics Letters*, vol. 121, no. 5, p. 052402, 2022.

- [59] “Neutron diffraction at ISIS.” [Online]. Available: <https://www.isis.stfc.ac.uk/Pages/Neutron-diffraction.aspx>
- [60] “WISH Detector at ISIS.” [Online]. Available: <https://www.isis.stfc.ac.uk/Pages/Wish.aspx>
- [61] Z. Kašpar, M. Surýnek, J. Zubáč, F. Krizek, V. Novák, R. P. Campion, M. S. Wörnle, P. Gambardella, X. Marti, P. Němec *et al.*, “Quenching of an antiferromagnet into high resistivity states using electrical or ultrashort optical pulses,” *Nature Electronics*, vol. 4, no. 1 Supp., pp. S9–15, 2021.
- [62] A. K. Zvezdin and V. A. Kotov, *Modern magneto optics and magnetooptical materials*. CRC Press, 1997.
- [63] V. Saidl, P. Němec, P. Wadley, V. Hills, R. Campion, V. Novák, K. Edmonds, F. Maccherozzi, S. Dhesi, B. Gallagher *et al.*, “Optical determination of the Néel vector in a CuMnAs thin-film antiferromagnet,” *Nature Photonics*, vol. 11, no. 2. Supp, pp. 91–96, 2017.
- [64] C. Thomsen, H. T. Grahn, H. J. Maris, and J. Tauc, “Surface generation and detection of phonons by picosecond light pulses,” *Physical Review B*, vol. 34, no. 6, p. 4129, 1986.
- [65] H. Gomonay and V. M. Loktev, “Magnetostriction and magnetoelastic domains in antiferromagnets,” *Journal of Physics: Condensed Matter*, vol. 14, no. 15, p. 3959, 2002.
- [66] F. Qin, B. Li, L. Chen, and Z. Shang, “Laser-induced surface acoustic waves for measurement of elastic constants based on mode conversion,” *Materials Chemistry and Physics*, vol. 242, p. 122523, 2020.
- [67] G. Pharr and W. Oliver, “Measurement of thin film mechanical properties using nanoindentation,” *Mrs Bulletin*, vol. 17, no. 7, pp. 28–33, 1992.
- [68] J. W. Tucker and V. Rampton, *Microwave ultrasonics in solid state physics*. North-Holland, 1973.
- [69] W. S. Slaughter, *The linearized theory of elasticity*. Springer Science & Business Media, 2012.
- [70] A. Raihane, R. Tourbot, F. Ladieu, and D. L’Hôte, “A simple device for dielectric spectroscopy of polymers with temperature regulation close to 300 K based on a Peltier junction,” *Review of Scientific Instruments*, vol. 83, no. 4, p. 043903, 2012.
- [71] J. Zubáč, Z. Kašpar, F. Krizek, T. Förster, R. P. Campion, V. Novák, T. Jungwirth, and K. Olejník, “Hysteretic effects and magnetotransport of electrically switched CuMnAs,” *Physical Review B*, vol. 104, no. 18, p. 184424, 2021.
- [72] J. Godinho, H. Reichlová, D. Kriegner, V. Novák, K. Olejník, Z. Kašpar, Z. Šobáň, P. Wadley, R. Campion, R. Otxoa *et al.*, “Supplementary information for electrically induced and detected Néel vector reversal in a

collinear antiferromagnet,” *Nature communications*, vol. 9, no. 1 Supp., p. 4686, 2018.

# **Appendix A**

## **List of Abbreviations**

---

<b>Abbreviation</b>	<b>Definition</b>
AC	Alternating Current
ADC	Analogue-to-Digital Converter
AFM	AntiFerroMagnet
AMR	Anisotropic MagnetoResistance
ASOPS	ASynchronous OPtical Sampling
BBO	Barium Borate
CAD	Computer Aided Design
CNC	Computer Numerically Controlled
CW	Continuous Wave
DC	Direct Current
DW	Domain Wall
FM	FerroMagnet
FPGA	Field Programmable Grid Array
GMR	Giant MagnetoResistance
HAADF	High-Angle Annular Dark Field
HAMR	Heat Assisted Magnetic Recording
HDD	Hard Disk Drive
ID	Inner Diameter
IP	In-Plane
ISGE	Inverse Spin Galvanic Effect
MLD	Magnetic Linear Dichroism
MO	MagnetoOptical
MRAM	Magnetic Random Access Memory
ND	Neutral Density
NSOT	Néel order Spin Orbit Torque
OD	Outer Diameter
OOP	Out-Of-Plane
PEEK	PolyEtherEtherKetone
PEEM	PhotoEmission Electron Microscopy
PEM	Photo-Elastic Modulator
QMD	Quadratic Magnetic Deflection
RTS	Room Temperature System
SAW	Surface Acoustic Wave
SEM	Scanning Electron Microscope
SHG	Second Harmonic Generation
SOC	Spin-Orbit Coupling
SOT	Spin-Orbit Torque
SQUID	Superconducting QUantum Interference Device
STEM	Scanning Tunneling Electron Microscopy
STT	Spin Transfer Torque
TMR	Tunnelling MagnetoResistance
XMD	X-ray Linear Magnetic Dichroism
XRD	X-Ray Diffraction

---

# Appendix B

## Relevant Python Code

During the studies undertaken in this thesis, a python package was developed to aid in interfacing with equipment common between these experiments. This package allows for more rapid writing of scripts and reduced confusion when creating new measurement routines. This package can be found at <https://github.com/stupoole/Instruments>. Some example scripts utilising this package can be found at <https://github.com/stupoole/instrumentsexamples>.

A set of scripts, with simple graphic user interfaces, were developed to accelerate XMLD-PEEM image analysis and can be found at <https://github.com/stupoole/LEEM-analysis>. These scripts were based on the low energy electron microscopy (LEEM) analysis code by T. A. deJong, found at <https://github.com/TAdelJong/LEEM-analysis>. The adapted scripts rapidly calculate the XMLD images from the raw data while aligning all the frames in the raw data to account for drift during collection. The same drift correction can be applied to a series of the resulting XMLD images to align images taken at the same position at different times. This is helpful in quantifying the changes between images, i.e. as the result of electrical pulses. These scripts were used to analyse some of the data presented in Ref. 57.

Many more small scripts were developed to process data and interface with equipment for specific goals, but these are not made available.